npj | 2D materials and applications

Review article

Published in partnership with FCT NOVA with the support of E-MRS

https://doi.org/10.1038/s41699-025-00529-5

First-principles and machine-learning approaches for interpreting and predicting the properties of MXenes

José D. Gouveia[1,3], Tiago L. P. Galvão[2,3], Kais Iben Nassar[1] & José R. B. Gomes[1] ✉

MXenes are a versatile family of 2D inorganic materials with applications in energy storage, shielding, sensing, and catalysis. This review highlights computational studies using density functional theory and machine-learning approaches to explore their structure (stacking, functionalization, doping), properties (electronic, mechanical, magnetic), and application potential. Key advances and challenges are critically examined, offering insights into applying computational research to transition these materials from the lab to practical use.

Over the past decade, we have been witnessing a transformative wave in the search of novel materials, mainly propelled by an explosion of interest in two-dimensional (2D) materials after the discovery of graphene, their exceptional properties and many potential applications. Researchers worldwide have been investigating the unique properties and applications of these ultrathin structures, notably, of a family of two-dimensional transition metal carbides, nitrides, and carbonitrides, named MXenes, which were discovered in 2011[1].

The first synthesis of an MXene considered the room temperature exfoliation of a powder of Ti_3AlC_2 MAX phase with hydrofluoric acid (HF), followed by ultrasonication of the reaction products in methanol, originating a material composed of Ti_3C_2 layers terminated by fluorine and hydroxyl groups[2]. This work had a significant impact since many tens of MAX phases were already known, suggesting that several other 2D crystals could be obtained using a similar synthetic approach.

The MAX phases are hexagonal layered ternary transition metal nitrides and/or carbides, with a $M_{n+1}AX_n$ formula, where $n = 1–4$, where M corresponds to an early transition metal (e.g., from groups 3–6 in the Periodic Table), A stands for an element from a subset of groups 12–16, but mostly from groups 13 and 14, and X corresponds to either carbon (C) and/or nitrogen (N). Traditionally, an etchant is used to selectively remove the A-layer elements, which contributes to the weakening of the interactions between the $M_{n+1}X_n$ layers, allowing them to be readily separated. However, less hazardous (HF-free) synthetic pathways were proposed for obtaining MXenes, such as the NaOH-assisted hydrothermal process[3], or the electrochemical etching with diluted HCl[4] or NH_4Cl/TMA-OH (TMA = tetramethylammonium)[5]. The general formula of MXenes is $M_{n+1}X_nT_x$, where M and X are the same as in the MAX phases, and T stands for the surface termination, usually determined by the synthesis conditions (e.g., -OH, -O, or -F are very common). The subscript x in T_x is used to denote that the surface is not necessarily uniformly or fully functionalized. Heating treatments have been devised to remove the hydroxyl and fluoro surface terminations, followed by an H_2 treatment to remove the oxo groups on the surface, yielding bare MXenes (i.e., without surface terminations and formula $M_{n+1}X_n$)[6,7]. Kamysbayev et al.[8] successfully defunctionalized the $Ti_3C_2Br_2$ and Ti_2CBr_2 to their bare counterparts, Ti_3C_2 and Ti_2C, respectively, using LiH at 300 °C. Please note that while it is possible to attain MXenes experimentally, they cannot exist outside a vacuum environment, which severely limits its application.

In 2017, layered ternary transition metal borides (MAB phases) were used to synthesize a family of 2D materials analogous to that of MXenes, the so-called MBenes[9], that rely on layers of boron rather than on layers of carbon/nitrogen.

MXenes have garnered significant attention for their exceptional electronic, mechanical, and thermal properties. They display high electrical and metallic conductivity, high oxidation resistance, and hydrophilicity that can be tuned upon hybridization with other materials which, when combined with concomitant large surface areas and versatile structures, make them very attractive for potential applications in various fields, e.g., energy storage, catalysis, etc. The interest in MXenes, according to Google Trends (accessed November 19, 2024), is shown in Fig. 1. The interest has been growing exponentially by 34% per year, with a correlation coefficient $R^2 = 0.97$.

MXenes have become focal points in both experimental and computational studies. So much is known about MXenes and so much research has been going on that there are already countless reviews on MXenes, focused on very specific areas, such as biomedical applications[10], electromagnetic interference shielding[11,12], quantum dots[13], or polymer nanocomposites[14], to name a few very recent ones. However, reviews focused on theoretical

[1]Department of Chemistry, CICECO – Aveiro Institute of Materials, University of Aveiro, Campus Universitário de Santiago, Aveiro, Portugal. [2]Department of Materials and Ceramic Engineering, CICECO – Aveiro Institute of Materials, University of Aveiro, Campus Universitário de Santiago, Aveiro, Portugal. [3]These authors contributed equally: José D. Gouveia, Tiago L. P. Galvão. ✉e-mail: jrgomes@ua.pt

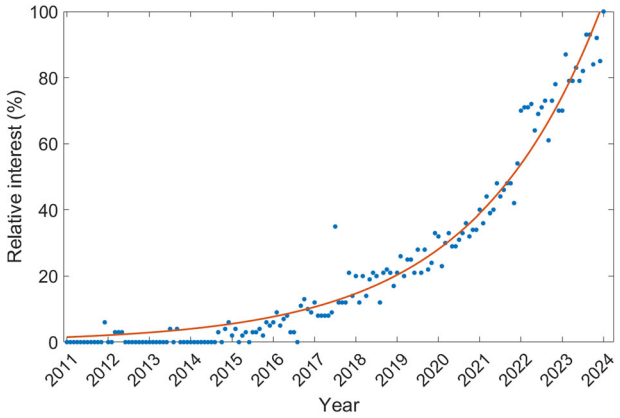

Fig. 1 | Relative interest in MXenes over time. Exponential relative interest in MXenes over time (blue dots, one per month). Data obtained from Google Trends.

advances only are rare. To the extent of our knowledge, three of the most recent such reviews[15–17] deal solely with electrocatalysis and energy applications. In contrast, there are countless reviews on MXenes as catalysts, with little or no focus on theoretical advances in this area[18–24].

In this review, we aim to provide a more general view of how computational techniques can contribute to predict or explain the general properties and applicability of MXenes, both the ones that have already been obtained experimentally and those that have not yet been synthesized, and to motivate the synthesis of new MXenes. In particular, we focus on the intersection between density functional theory (DFT) and machine learning, and on the potential of these approaches to unravel the intricacies of MXenes. As we delve into the geometric and electronic structure, and functionalization of MXenes, a comprehensive understanding of their behavior at the atomic and molecular levels emerges. These computational approaches are shown to be essential to accelerate the pace of 2D material research, providing crucial insights into MXene properties and in deciphering complex relationships within MXene systems, facilitating the design of materials with tailored properties and guiding experimental efforts.

Methods based on density functional theory

Computational methods based on the DFT circumvent approximately solving the Schrödinger equation of a quantum system, by directly obtaining its electron density and, from it, extracting information on physical quantities of interest for the ground state of the system. These include relative energies between different system configurations, bond lengths and angles, atomic charges, or the band structure. Moreover, the first and second derivatives of the energy with respect to the position of the atoms can be used to find special points (minima or N-order saddle-points) at the potential energy surfaces, which are essential for obtaining a complete picture of the energy landscapes of chemical reactions.

In DFT, the poly-electronic wavefunction composed by 3N spatial and N spin variables is replaced by the electron density consisting of three spatial variables only. This critical step is anchored on two theorems by Hohenberg and Kohn[25], one stating that the ground state for any system of interacting particles in an external potential, with a given fixed inter-particle interaction, is a unique functional of the electron density and another stating that the ground state energy of the system is the overall minimum value of this functional, i.e., the ground state energy is obtained through minimization of the energy functional with respect to the electron density, hence yielding the energy and the density of the ground state. However, despite considerable efforts since then, the exact form of the energy functional is not known and approximations had to be introduced. One year later, Kohn and Sham[25] proposed to represent the many-body problem of interactions in a poly-electronic system into a problem of non-interacting electrons evolving in an external potential. This strategy enables to flyover the terms that are very difficult to calculate, corresponding to kinetic and electronic repulsion, through one-electron Kohn-Sham equations that yield the energies of the corresponding Kohn–Sham orbitals, which are further employed to obtain the density for an N-particle system. The total energy of the system is obtained upon minimization, with respect to the electron density, of the sum of the Kohn-Sham (non-interacting) kinetic energy, electron–electron interaction energy (or Coulomb energy), and the exchange-correlation energy. The latter combines the effects of electron exchange and correlation, i.e., the residual part of the true kinetic energy (because of the approximation of a non-interacting system) and the non-classical electrostatic contributions. In other words, the exchange-correlation energy includes all that we do not know how to calculate exactly and that must be approximated somehow. It is precisely the complexity of the form that is used to approximate the calculation of the exchange-correlation energy that leads to the classification of methods based on the density functional theory in different classes.

Depending on the complexity (and accuracy) of the way the exchange-correlation term is approximated, Perdew et al. proposed a conceptual hierarchy of density functionals, the so-called "Jacob's ladder of density functional approximations for the exchange-correlation energy"[26], which starts at the Hartree world and ascends in terms of sophistication and accuracy from lower to higher rungs.

i. **Local Spin Density Approximation (LSDA):**
The simplest form of exchange-correlation functional.
Approximates the exchange-correlation energy density at each point in space based solely on the local electron spin density.
Adequate to treat densities that vary slowly over space but underestimates certain properties due to neglecting gradient corrections (suitable for solids but not for molecules).

ii. **Generalized Gradient Approximation (GGA)**:
An advancement over LSDA that considers not only the electron spin density at each point but also the gradient of the density.
Incorporates corrections based on the density gradient, improving accuracy in describing molecular geometries and some properties.
A widely used example is the PBE functional[27].

iii. **Meta-Generalized Gradient Approximation (meta-GGA)**:
Goes beyond GGA by including the kinetic energy density in addition to the electron density and its gradient.
Provides more accurate descriptions of molecular properties such as dispersion interactions and reaction barriers compared to GGAs.
Some examples are TPSS or the M06 family of functionals[28,29].

iv. **Hybrid Functionals**:

i. **Global Hybrid Functionals**
Combine the GGA or meta-GGA exchange-correlation functionals with a fraction of exact Hartree-Fock exchange.
Offer improved descriptions of electronic structure, energetics, and band gaps compared to pure GGA or meta-GGA functionals.
Examples include the B3LYP[30,31] and PBE0[32,33] functionals.

ii. **Range-Separated and Screened Hybrid Functionals**:
Treat short-range and long-range electron-electron interactions separately.
Offer better descriptions of charge-transfer excitations and solid-state properties.
Some examples are ωB97X[34], CAM-B3LYP[35], HSE06[36] and LC-PBE[37].

v. **Double-Hybrid Functionals**:
Include functionals that use not only occupied Kohn-Sham orbitals but also virtual orbitals, via methods such as MP2 or the random phase approximation (RPA).
Improve with unprecedented accuracy some chemical or physical properties of large-gap compounds, e.g., reaction energies, reaction barrier heights, and nonbonded interactions.
Examples include B2PLYP[38] and PWPB95[39].

The development of hybrid and double-hybrid functionals is part of an effort to improve the accuracy of calculations for molecular and solid-state

systems by addressing the limitations of earlier functionals. Hybrid functionals have adjustable parameters and were introduced to mitigate self-interaction and improve exchange-correlation accuracy, while the double-hybrid functionals were developed to enhance accuracy when applied to complex systems with short- and long-range correlation effects. The choice of density functional often depends on the system being studied and the properties of interest. While higher-rung functionals tend to be more accurate, they also come with increased computational cost, making them less practical for large systems. In fact, most studies published in the literature consider semi-local methods, either functionals from rungs 2 and 3 when combined with plane-waves, or hybrid approaches from rung 4 when combined with atomic orbitals. Moreover, either with plane-waves or atomic orbitals, approaches that are capable of accurately describing dispersion are often combined with the functionals for describing non-covalent interactions. A notable example is the atom–atom pairwise empirical dispersion corrections by Grimme et al.[40–42] which found widespread application. Also, for overcoming the intrinsic self-interaction errors associated with e.g., the functionals from rung 2 and affecting the correct description of localized electrons in many transition metal oxides as CeO_2 or NiO, another empirical approach[43] using the so-called Hubbard term ($+U$) that penalizes double occupancy of d or f orbitals has been widely employed. We performed an analysis of the articles published in 2023, where DFT methods were employed to study MXenes, and we found that nine in ten studies considered the Perdew-Burke-Ernzerhof (PBE) functional (3/5 of them augmented with Grimme et al. dispersion corrections). The remaining works considered functionals from different rungs of the ladder such as PZ[44], HSE06[36], TB-mBJ[45], wB97xD[46], or B97M-V[47].

In summary, different DFT functionals may be used to perform a computer simulation but they must be chosen wisely depending on the property of interest because of their intrinsic limitations. By being based on first principles, DFT provides results at the electronic level, which is both a strength and a limitation of the method. This is because the finer the level of detail of a computational model, the smaller system sizes can be successfully simulated in a reasonable amount of time. Indeed, DFT provides incredibly reliable results for quantum systems, at the cost of only being able to simulate a few thousand atoms with the algorithms and computational capabilities of today, when compared with the millions of particles that can be studied, for instance, with force field-based approaches[48]. Still, these approaches have been proven key in studies of the properties of materials, such as localized defects, adsorption and catalysis. This information is not only useful by itself, but it can also be fed to higher-level approaches, so that they do not need to go into the electronic detail and can therefore simulate much larger systems. In the majority of the DFT studies reported in the literature, the DFT calculations are performed at $T = 0$ K, i.e., the effects of the temperature are not considered. The inclusion of the temperature may be accomplished by combining the classical Newtonian equations to describe the motion of the atomic nuclei in the system with the DFT calculated forces acting on the atomic nuclei under specific initial conditions (positions and velocities of the nuclei) and boundary conditions to study how the dynamics of the molecular system evolves with time. This approach constitutes the ab initio molecular dynamics method, which is very time-consuming. Alternatively, standard statistical thermodynamics combined with data from a second-derivative analysis of the system can be used to estimate energies at specific pressure and temperature conditions, significantly reducing the computational cost.

No matter how much technology advances, computational resources are always finite and the calculations cannot be indefinitely parallelized. Therefore, any computational simulation aims at obtaining results as accurate as possible at the lowest computational cost possible. In the case of quantum mechanical simulations, several parameters can be tuned to achieve a compromise between accuracy and cost. The two most relevant ones are the size of the basis set used to expand the Kohn-Sham orbitals and the density of the grid of k-points used for reciprocal space integration[49]. The higher these two quantities are, the more accurate and resource-consuming the results become. Therefore, one of the first steps in a first-principles study is to find the minimum values of these parameters that yield converged results for a test calculation, i.e., to find the point beyond which the increased computational cost does not lead to significant changes in the results. Other parameters of interest include energy and force convergence criteria, and performing spin-polarized calculations or not[50].

Methods based on machine learning

Machine learning (ML) allows to develop statistical models that enable computers to learn from and analyze existing data, thereby identifying patterns and making predictions[51,52]. Based on data obtained experimentally or by DFT calculations, ML has proven instrumental in predicting MXene properties and proposing new materials tailored for specific uses, as discussed throughout this review. The integration of ML in materials science research not only facilitate the prediction of material suitability for specific applications, but also provides statistical insight into key material features, elucidating their aptness for particular uses and potentially reducing experimental time and costs, particularly when a large number of predictions have to be made in order to explore a broader portion of the materials' chemical space.

To support such advances, several databases have been developed to provide comprehensive datasets for MXenes. Some examples are: i) the aNANt MXene database[53,54], hosted by the Indian Institute of Science, which contains information on over 23,000 MXene structures, including calculated properties; ii) the MXenes Database by MEM-CES[55], which includes 730 structural data files (cif format) for MXenes and aims to provide simulated adsorbent metrics of MXenes for CO_2/H_2 separations; and iii) the MXene-db[56,57], which offers structural and computational band gap data for over 4000 MXene structures. These databases serve as foundational tools for ML-driven exploration and design of MXene materials, facilitating deeper insights and accelerating discovery processes.

The development of an ML model involves the following steps[58]:

i. *Data preparation*: Machine learning models require well-prepared data for calibration and performance evaluation, often sourced through data mining or computational simulations. These data must be meticulously curated, involving processes such as loading, processing, cleaning, and refining. Key challenges in materials science include addressing missing values, correcting inaccuracies, and standardizing units. Subsequently, conducting an exploratory data analysis is crucial to uncover underlying correlations, identify anomalies, and test hypotheses, typically involving a combination of summary statistics and visual representations. At the end of the data treatment, the obtained dataset should be split into three disjoint groups: training, validation, and testing. The training set is employed to calibrate the internal model parameters for each algorithm by fitting this part of the dataset. The validation set is utilized to choose the best combination of algorithm choice and its hyperparameters (settings that are configured before training the model and are not learned from the data), and also the best features. The test set is used to evaluate how the model performs for new data. A significant portion of machine learning projects is dedicated to data preparation, underscoring its importance for the success of the model. A word of caution is necessary when using data obtained through different DFT methods, as certain properties, such as band gaps, can exhibit significant variability. This variability often stems from the underestimation of experimental values by specific functionals. Therefore, combining data from studies employing different functionals or computational setups must be approached carefully, as machine learning models rely on consistent and homogeneous datasets to ensure reliability. To address this challenge, we propose using the digital object identifier (DOI) of the publication from which the data were retrieved as an additional descriptor. Including this information allows the integration of results from computational studies with slightly different parameters while maintaining traceability and enhancing the interpretability of machine learning predictions.

ii. *Feature Engineering*: Features serve as input variables used to predict output properties. In materials design, they are also referred to as descriptors and can include a large range of material properties, from experimental data to computed values obtained by methods like DFT. In addressing materials-related problems, prioritizing highly predictive features can be as crucial as the choice of algorithm, with expert knowledge playing an important role. Although a vast array of features, ranging from hundreds to thousands, may be initially considered for a given material, typically only a select few prove to be significant for the effectiveness of the final model. Consequently, the process of feature selection becomes indispensable. This process may incorporate various methodologies, such as filter methods that rely on specific statistical metrics, wrapper methods like backward feature elimination, or specialized algorithms including LASSO (Least Absolute Shrinkage and Selection Operator) regression[59], which are instrumental in refining the model for optimal performance.

iii. *Model optimization*: Model optimization aims to find the best combination of algorithm and hyperparameters. Most ML tasks can be categorized as unsupervised or supervised learning. Unsupervised learning works with unlabeled raw data to reveal relationships and patterns, while supervised learning uses labeled data to make predictions. Unsupervised learning makes use of clustering and association techniques, while supervised learning can be divided into regression (to predict numerical outputs) and classification (to identify data classes). Some common algorithms for these tasks are linear regression, k-nearest neighbors, decision trees, random forest, gradient boosting, support vector machines, and neural networks. A description of these algorithms can be found in ref. 60. XGboost (an implementation of gradient boosting)[61] is often the top choice for standard tabular numerical data, while deep neural networks excel in handling images, audio, and text, but can also be a top choice for tabular data[62]. Nevertheless, usually, the higher the complexity of the algorithm, the lower the explanatory power[63]. Despite various factors being in play, a recent empirical study suggests that the explanatory power of decision trees and random forest takes over other ML models[64]. Errors associated with model optimization can usually be categorized in two sources: underfitting and overfitting. Underfitting occurs when a model does not fit the training data well, while overfitting makes a model too specific to the training data, not being able to be generalized for new data. Ideally, *k*-fold cross-validation should be used to evaluate the model, since it helps estimate how well the model is likely to perform for new data, and can help mitigate issues such as overfitting. Both $k = 5$ and 10 have been verified to have low bias towards the validation set at a reasonable computational cost, and are commonly employed[65]. For example, in tenfold cross-validation, the model gets tested ten times on 10% validation subsets after ten training rounds on the remaining 90% of the cross-validation data.

iv. *Feature importance*: When satisfactory performance is obtained from cross-validation during the model optimization phase, feature importance should be investigated in order to interpret the model and understand what the algorithm has found in the data, understand if more features related to those with higher predictive power should be added to the model or, otherwise, to eliminate non-important features that are adding noise to the model. There are several feature importance methods. Mean Decrease in Impurity (MDI) is a specific method for tree-based methods (decision trees, random forest, XGBoost, etc.) and computationally inexpensive to obtain. Feature Permutation Importance (FPI), where each column representing a feature is randomly shuffled one by one, and the model evaluated each time, with the more important features, when shuffled, resulting in a greater degradation of the performance metrics of the model. FPI can be applied to any ML algorithm, but it is also more computationally expensive than MDI, for example[66]. SHAP (Shapley Additive exPlanations) values is a methodology based on cooperative game theory, where these values are calculated by considering all possible combinations of features and assessing the change in the output of the model when each feature is added to these combinations. It involves retraining the model numerous times, which makes it even more computationally intensive than FPI, but can also be applied to any algorithm[67].

v. *Final test*: The final test set is intended to evaluate the real performance of the model, using new data, unseen by the model during the previous feature engineering and model optimization steps. Typically, it comprises 10% to 30% of the whole dataset. If further model refinement is needed, new data should be used for this step. The minimum requirements of a useful ML model can vary greatly depending on the domain of application, the nature of the data, and the problem being solved. In terms of statistical performance metrics, our experience tells us that, as a rule of thumb, an R^2 of at least 0.5 should be considered for regression problems, and an accuracy of at least 70% would be expected for classification problems, but even this depends on each problem and other statistical metrics might tell a different story for better or worse. For regression problems, the R^2, mean absolute error and root mean squared error should be reported[68], while for classification problems, the accuracy, precision, recall, balanced accuracy or F1 score, and kappa value or Matthews correlation coefficient[69], should be considered. The robustness to overfitting (drop in the quality of the metrics from cross-validation to final test), training time and computational resource efficiency, scalability with the amount of data, and interpretability, are also factors to consider.

Structure of MXenes

MXenes were first synthesized just over 10 years ago, and that is enough time for plenty of properties of these materials to have been studied extensively. This includes MXenes that have been manufactured, and ones that have not been obtained in the laboratory yet but have been predicted to be stable by computational studies[70]. Many computational studies have taken advantage of the experimental observation of bare MXenes to simplify the models used by neglecting surface termination. Comprehensive overviews of which MXenes have been experimentally reported, and of the known properties of MXenes in general, can be found in refs. 71,72. Here, we present an overview of a selection of recent works in which DFT calculations were employed to study properties of already known MXenes or newly introduced ones.

Effect of surface termination on MXene properties

After the first MXene, Ti_3C_2, was isolated, computational works were quick to predict that many others, with different M or X elements or with different thickness, should be stable as well, and efforts immediately started to create them in the experimental laboratory. Indeed, for example, around five years after the advent of MXenes, the Ti_2N and Ti_4N_3 MXenes had been synthesized[73,74]. The $Ti_{n+1}N_n$ MXene variant with three Ti layers, Ti_3N_2, has apparently been elusive so far, but it is still a representative model of the titanium nitride MXenes. Although upon synthesis MXenes are initially covered by O, F, and OH terminal groups[75,76], the oxygen group is by far the one that adsorbs the strongest, thus being the most likely to be found[77]. Furthermore, post-processing methods easily replace the whole surface termination by O[76]. This motivated Aghaei et al., to analyze the properties of the Ti_3N_2 MXene versus those of its oxygen-covered counterpart, $Ti_3N_2O_2$, (see Fig. 2) using DFT[78].

The chosen exchange-correlation functional was the generalized gradient approximation (GGA) variant introduced by Perdew, Burke, and Ernzerhof (PBE)[27], supplemented by dispersion corrections by Grimme[41], to account for longer-range van der Waals interactions. This combination has become known as PBE-D, which may be followed by a number depending on the version of the Grimme's correction, and, as we will see, has become one of the standard choices in computational studies of MXenes.

Using PBE-D2, Aghaei et al. found that $Ti_3N_2O_2$ displays cohesive energy that is 30% lower than that of the clean MXene, signifying greater stability of the functionalized surface. Structurally, the innermost Ti-N ionic bond lengths were found to remain almost unchanged by the addition of O,

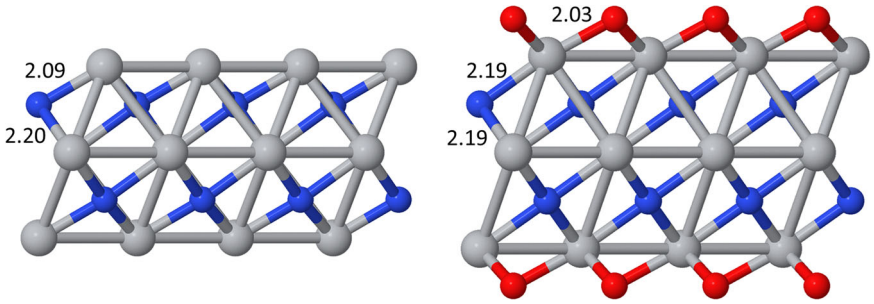

Fig. 2 | Molecular models for bare and O-covered Ti_3N_2 surfaces. Side views of models of the Ti_3N_2 (left-hand side) and $Ti_3N_2O_2$ (right-hand side) MXene surfaces. The values shown are bond lengths in Å, taken from ref. 78.

while the outer Ti-N covalent bonds are stretched by 5%. This is accompanied by an accumulation of electrons both on N and on O atoms, so that all Ti-N bonds become ionic, and the only remaining covalent bonds are Ti-O. Both Ti_3N_2 and $Ti_3N_2O_2$ were confirmed to be metallic[77], but oxidation was predicted to negatively impact the conductivity of the material. The O surface termination was also predicted to considerably reduce radiation absorption and reflectivity in the visible region, while increasing them at higher frequencies.

Bjork and Rosen studied the competition between twelve surface terminating species (O, OH, N, NH, NH_2, S, SH, H, F, Cl, Br, and I) on six experimentally obtained MXenes (Ti_2C, Nb_2C, V_2C, Mo_2C, Ti_3C_2, and Nb_4C_3) using DFT-PBE[79]. They confirmed that the chemical elements that adsorb the strongest on both nearly bare and fully covered MXenes are O and F. This result held for both vacuum and a simulated oxygen atmosphere. Infact, it was found that, in an oxygen atmosphere, it is thermodynamically advantageous to have no surface termination than to have a sulfur one, as O_2 reacts with the S termination to form SO_3 and then O replaces S as the surface termination. Furthermore, O and F were predicted to be the most thermodynamically favorable species to fill any kind of termination vacancy of any of the studied MXenes. In particular, the exposition of an OH-covered MXene to O_2 was predicted to remove the hydrogen from all OH groups, a conclusion that was also reached by Gouveia and Gomes[80]. The calculations by Bjork and Rosen also showed that a termination vacancy of an O-covered MXene is most likely to be filled by F than by any other species, indicating that an oxygen treatment does not replace the F surface termination and that a hypothetical fully F-terminated synthesized MXene should be very resistant against oxidation at ambient temperature. This oxidation resistance was observed both experimentally[81] and theoretically[82], although it has been demonstrated that high temperatures can remove the fluorine termination but not the oxygen one[7].

In a later study[83], Hou et al. focused their attention on the oxidation process of MXenes in aqueous systems. They considered the vanadium carbide MXene with oxo terminations as a prototype system and molecular models in which the empty space—often used in DFT studies to separate MXenes from their replicas in the periodically repeated images—was replaced by a varying number of water molecules. They performed DFT-based molecular dynamics (MD) simulations (PBE-D3), within the NVT ensemble ($T = 300$ K) and using small molecular models with up to 180 atoms ($V_{24}C_{12}O_{24}$·40 H_2O model), which were employed to develop a neural network potential for MD simulations using much larger models, with up to 20250 atoms ($V_{5400}C_{2700}O_{5400} \cdot 2250\ H_2O$). Their simulations are supportive of a spontaneous energy minimization process in which water molecules first interact directly with V atoms before proton release occurs. At the atomic scale, an oxygen atom from a water molecule moves toward the V_2CO_2 MXene surface, displacing a V atom from its equilibrium position and forming a V–O bond. Supported by two neighboring water molecules, the O–H bonds of the adsorbed water break one after the other as the V–O bond shortens, ultimately leading to the formation of a $[VO_4]^{\delta-}$ structure. Importantly, this incipient stable form of vanadium oxide together with the formed H_3O^+ species where found to inhibit subsequent oxidation reactions in nearby regions, hence contributing to the stabilization of the MXene against oxidation and preventing its very fast degradation[83].

Dahlqvist and Rosen performed PBE-D3 and rev-vdW-DF2 calculations with the VASP code to analyze how the nature and degree of surface termination of MXenes can affect, and hence used to control, their structural, electronic, and mechanical properties[84]. They considered halogen- and chalcogen-terminated MXenes, specifically M_2CT_x (M = Ti, Zr, V, Nb, Ta; T = S, Se, Te, Cl, Br, I; $x = 1, 2$). The findings show that MXenes with larger terminal atoms (such as Br and Cl on Ti_2C, Nb_2C, and Ta_2C) favor non-ideal termination coverage ($x < 2$), resulting in mixed termination sites and lower binding energies (i.e., energy difference ongoing from multilayer to single sheet MXene models), with concomitant propensity to delamination into single layers, though very low coverage can lead to structural collapse. Their study also revealed that non-ideal coverage increases the density of electronic states at the Fermi level, potentially boosting conductivity.

Atomic layer stacking and ordering

A peculiar way to tune the properties of MXenes is to change the way their atomic layers are stacked. Sun et al. first introduced this concept for the Mo_2C, Tc_2C, and Os_2C MXenes[85]. The underlying idea is that, for some MXene compositions, the surface is more stable if all the metallic atomic layers are aligned with each other, in an ABA configuration with D_{3h} symmetry, rather than staggered with respect to each other, as in the traditional MXene ABC configuration with D_{3d} symmetry (see Fig. 3).

Gouveia et al. then conducted a systematic DFT study which covered nine M element possibilities, X being C or N, the M_2X, M_3X_2, and M_4X_3 stoichiometries, both atomic layer stacking possibilities, and bare or O-terminated surfaces, for a total of 216 MXenes, in order to determine what makes different MXenes prefer different stackings[86]. They used the PBE functional with the Grimme dispersion corrections in their PBE-D3 version[40], because this study served as a reference to additional studies to further analyze how the change in atomic layer stacking can affect the adsorptive and catalytic properties of the MXene that are reviewed in separate subsections below. All MXenes made of M in group 6 of the Periodic Table and the MXene nitrides with M in group 5, apart from V_2N, were found to thermodynamically prefer the ABA stacking. Regardless of the preferred configuration, the energetic difference between the ABC and ABA configurations was predicted to change linearly with the thickness of the material, indicating that the relative stacking stability is per MXene layer. Furthermore, the surface O coverage bolsters the preference for the ABA stacking, making it even more stable when it is the most favorable one, or less unstable when ABC is preferred. The energy barriers for the transition from ABC to ABA stacking were calculated using the dimer method[87], and led to the conclusion that this transition is kinetically feasible, especially on O-terminated MXene surfaces. Nearly all energy barriers were found to be below 1 eV, the lowest ones being 0.09 and 0.10 eV, corresponding to Cr_2CO_2 and W_2NO_2, respectively. The shift to the thermodynamic stabilization of ABA stacking was ultimately attributed to a higher electronic density of the material, since stronger preference for the ABA alignment was found for M elements with more *d* electrons, for MXenes made of N rather than C, and in the presence of O surface groups.

Based on this study, Jurado et al. devised a strategy to experimentally identify the stacking of the Mo_2C MXene by using CO, CO_2, or H_2O as probe molecules[88]. A difference of almost 1 eV was calculated for the

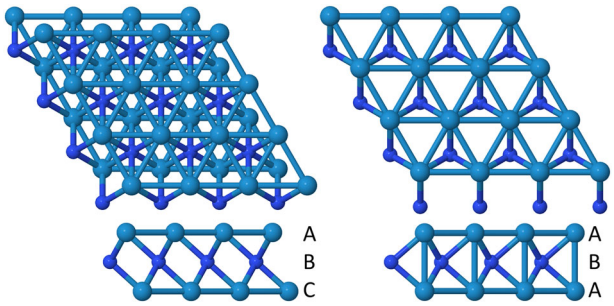

Fig. 3 | Molecular models for the W_2N MXene surface with ABC and ABA stacking. Top and side views of models of the W_2N MXene showing the two known stable atomic layer stacking possibilities for MXenes: ABC (left-hand side) and ABA (right-hand side).

adsorption energy of CO_2 on ABC-Mo_2C or ABA-Mo_2C. Moreover, the frequency of the asymmetric stretching vibrational mode of CO_2 and of the stretching mode of CO were found to differ by 150 and 300 cm^{-1}, respectively, which should be more than enough to clearly distinguish the two stacking possibilities experimentally. This provides a spectroscopic method to assess whether an ABC-to-ABA transition (or vice versa) has taken place in practical applications.

Triggered by the discovery of a new sub-family of $M_5X_4T_x$-like MXenes, more specifically, of the $Ti_{2.5}Ta_{2.5}C_4T_x$ and $Ti_{2.675}Nb_{2.325}C_4T_x$ MXenes[89], Downes et al. performed non-spin-polarized PBE calculations to predict stable compositions of MAX phases with potential for to add new MXenes to the M_5X_4 sub-family. More specifically, these authors studied $(M'_{1-y}M''_y)_5AlC_4$ MAX phases, either with the traditional $P6_3/mmc$ or the twinned $P\bar{6}m2$ structures, with M′ and M″ elements randomly arranged, keeping out-of-plane chemical ordering but with in-plane disorder. Interestingly, while in most cases the systems displaying solid-solution disorder were more stable than when having ordered arrangements, a few cases, namely, $Mo_3Sc_2AlC_4$ ($P6_3/mmc$), $Mo_3Ti_2AlC_4$ ($P\bar{6}m2$) and $Mo_3Sc_2AlC_4$ ($P\bar{6}m2$) have a stable ordered Mo-M″-Mo-M″-Mo (M″ = Sc or Ti) stacking as concluded from the calculated Gibbs free energy of formation at $T = 2000$ K[89].

Several research groups have focused on the distinct structural and compositional characteristics of high-entropy (HE) 2D carbide MXenes, suggested as an exotic family of these promising materials. In particular, Nemani et al. synthesized two high-entropy MXenes, $TiVNbMoC_3$ and $TiVCrMoC_3$, highlighting their stability and complex elemental arrangements, as well complemented with results from DFT calculations with the PBE functional[90]. The latter allowed to calculate the enthalpy of formation of different MAX phase compositions, from the total energies of these structures and of the constituting M, A, and X elements, per atom, in their standard state (bulk phases), as well as the Bader charges of the M elements. Two important observations in their work were that i) the configurational entropy—the number of discrete representative positions of the alloy constituents, calculated as −0.1773 and −0.2238 eV/f.u. (formula unit) for three-M and four-M systems, respectively—is an important contributor to the stabilization of the phases, and ii) the synthesizability of MAX candidates is higher in those candidates with an electron concentration close to 0.3 e/atom.

Building on the results from the two studies reviewed above—namely, that certain combinations of M' and M" (e.g., Mo and Ti) lead to ordered MXene phases[89], and that HE MXenes can be experimentally synthesized[90], Leong et al. conducted a high-throughput first-principles study of the atomic configurations in the $TiVNbMoC_3$ and $TiVCrMoC_3$ MXenes, focusing on possible metal segregation[91]. To explore the vast compositional space, their approach involved constructing surrogate models for the MXene configurational energies using a generalized Ising model. These models were trained and parameterized with PBE, and subsequently employed to perform accurate calculations of configurational energies for various atomic arrangements in HE MXenes, across different compositions and temperatures, using Monte Carlo simulations. Their calculations predicted a distinct preferential occupancy of metal atoms across the four layers of single-phase HE MXenes, even at temperatures as high as 2900 K. Over a broad compositional range, the outer/inner M layers are predominantly occupied by two of the four metals, with a residual amount of a third element in the M'M"M'"M""C_3 MXene, with Cr most preferentially occupying the outer layers, followed by Mo, V, Nb, and Ti. A clear separation of Nb and V atoms was found to occur in the inner layers and, within each M layer, the atoms largely form a solid solution due to the increased configurational entropy.

A novel HE MXene with composition $Ti_{1.1}V_{1.2}Cr_{0.8}Nb_{1.0}Mo_{0.9}C_4T_x$ was successfully synthesized by Ma et al.[92], who performed in tandem a computational study with the PBE functional and considering different configurations of $Ti_1V_1Cr_1Nb_1Mo_1C_4T_x$ HE MXene model with and without (random positioning) ordered M layers. As reported by other authors[89], they found a propensity for structures with M layers arranged in a solid solution to display lower formation energy than structures with ordered M layers. Also, the calculated density of states of the 1Ti: 1V: 1Cr: 1Nb: 1 Mo composition is higher at the Fermi level than those of other Nb_2C, V_2C, and Ti_3C_2 MXenes[92], which was interpreted as an indication that the former MXene has better conductivity and electron migration than the latter.

Magnetic ordering

MXenes offer significant promise for advancing 2D magnetism research due to the wide range of potential transition-metal compositions. However, experimental investigations into their magnetic properties are still limited. Studies have primarily focused on titanium-based carbide MXenes[93–95]. While titanium itself is non-magnetic, it can contribute to magnetic behavior when alloyed with other elements (e.g., Cr in ref. 93) or structurally modified (e.g., by applying various surface terminations through acid treatments as in ref. 94), where effects like magnetic transitions and Pauli paramagnetism have been observed.

García-Romeral et al. considered the PBE, PBE0, and HSE06 functionals to carefully analyze the electronic ground state of the Ti_2C MXene[96], namely, to investigate the relative stability of antiferromagnetic (AFM), ferromagnetic (FM) and non-magnetic (NM) states. An AFM ground state for Ti_2C was predicted with the three functionals but the PBE0 functional was found to stabilize FM states more than the PBE or HSE06 approaches. The DFT-derived spin exchange parameters (J_1, J_2, J_3) revealed that the intralayer FM coupling (J_2) is the dominant interaction, but the other interactions were significant and opposite in sign. The results also suggested a spin model with one unpaired electron per Ti atom, highlighting a strong ionic bonding component, contrasting with prior assumptions of two unpaired electrons per Ti in a triplet state[97]. Hence, García-Romeral et al.'s analysis establishes an AFM ground state for Ti_2C with robust FM intralayer coupling, which can be considered promising for 2D magnetic applications. An important technical aspect arising from their work is that while spin polarization minimally impacts structural parameters, it notably influences total energy stability among different magnetic configurations[96]. PBE calculations on $p(1 \times 1)$ unit cells of Ti_2C, Zr_2C, and Hf_2C confirmed that these MXenes exhibit magnetic ground states, with ordering of stability AFM > FM > NM solutions[98].

The topic had already attracted the attention of several computational researchers who considered DFT to predict the magnetic behavior of MXenes incorporating metals like Cr (Cr_2C[99,100], and Cr_2N[100], with H, O, OH, F or Cl terminations), or Mn (Mn_2C[101], with F, Cl, OH, O, or H terminations). In the latter, He et al. performed calculations with the DFT $+U$ approach ($U = 3$ eV) and with the HSE06 functional, and found that the Mn_2C MXene retained a ferromagnetic (FM) ground state even upon symmetrical functionalization with singly negative charged groups (e.g., F, Cl, OH). Furthermore, the same authors found that surface functionalization enables tunable magnetic states, producing FM half metals, antiferromagnetic (AFM) metals, or AFM semiconductors depending on the

electronegativity of the functional groups. The change in the properties upon functionalization were previously reported by Si et al. for the Cr_2C MXene[99], but in the latter case upon surface functionalization with the same −1 charged groups, there was an FM-to-AFM transition only. Hence, the Mn_2CT_2 MXenes show unique electronic and magnetic properties that are promising for spintronic applications, notably, the Mn_2CF_2 MXene which exhibits intrinsic half-metallicity with a Curie temperature above room temperature (T_C = 520 K)[101].

More recently, García-Romeral et al. conducted further computational studies to investigate how increasing the number of metal layers in titanium carbide MXene—from 2 to 3 to 4—affects its magnetic properties[102]. They considered the PBE, PBE0, and HSE06 approaches, already used in their previous work[96], as well as the PBE+U (U = 3 eV) one. All methods indicated that the Ti_2C, Ti_3C_2 and Ti_4C_3 display magnetic ground states and that the magnetic coupling constants increase monotonically with the thickness of the MXene. These authors proposed a spin model where the surface titanium atoms are paramagnetic (Ti^+ with one unpaired electron) while those in the middle layers are diamagnetic (Ti^{2+} closed-shell). These authors extended their calculations to investigate the electronic ground state of M_2C (M = Ti, V, Cr, Zr, Nb, Mo, Hf, Ta, and W) MXenes[103], revealing that Ti_2C, Cr_2C, Zr_2C, and Hf_2C MXenes exhibit open-shell conducting ground states, with spin polarization localized on the metal atoms. In contrast, V_2C, Nb_2C, Mo_2C, Ta_2C, and W_2C MXenes display diamagnetic conducting ground states. Further analysis of trends across the Periodic Table groups indicated that the energy difference between FM and NM states decreases when descending along Group IV, whereas it increases when ascending along Groups V and VI.

Vacancy defects

Materials in the laboratory are never as crystalline as models depict them, and MXenes are no exception. In fact, atomic vacancies were quickly identified on the Ti_3C_2 MXene, the first to be synthesized[104,105]. The understanding of how likely these defects are to be formed and how they change the properties of the MXene has always been accompanied by theoretical DFT-based studies, such as refs. 106,107 for the Ti_2X family of MXenes. More recently, higher-throughput studies have been conducted to find the most likely types of vacancies on many MXenes[108].

Parey et al. studied three kinds of vacancies on 18 different M_2X-type MXenes, with M = Sc, Ti, V, Cr, Mn, Y, Zr, Nb or Mo and X = C or N. The DFT calculations were made using the PBE-D3 approach (the D3 correction was included to later analyze the influence of vacancies on CO_2 activation)[109]. The three types of vacancies considered were metal vacancies (V_M), X-element vacancies (V_C or V_N), and metal-X vacancies (V_{MC} or V_{MN}). Thermodynamically, carbide MXenes were predicted to be more likely to contain vacancies than nitride ones and, within each of these two groups, the most stable vacancy is V_C or V_N, respectively.

The results of Parey et al. are supported by those of Gouveia et al., who studied the structural and energetic properties of vacancies in 84 MXenes, each composed of one among nine metallic elements, C or N, pristine or with O or F surface terminating groups, and with ABC or ABA stacking[108]. To calculate the formation energy of the different vacancies, the energy references were as follows: for metal atoms, the energy per atom of one unit cell of hexagonal-close-packed (hcp) Ti, Zr, and Hf metals or body-centered-cubic (bcc) V, Nb, Ta, Cr, Mo, and W metals; for carbon, the energy per atom of one unit cell of diamond; for nitrogen and oxygen, half the energy of gaseous nitrogen (N_2) and oxygen (O_2), respectively; and for fluorine, the energy difference between gaseous hydrogen fluoride (HF) and half of gaseous hydrogen (H_2). Gouveia et al. found that in O-terminated MXenes, C or N vacancies are still the most likely to be found, while M atoms become much harder to remove. For example, on Ti_2C, the V_{Ti} formation energy was calculated at just over 2 eV, while this value increased to more than 8 eV on Ti_2CO_2, as per previous studies[106]. This is a consequence of both the well-known oxophilicity of MXenes and stability of O-terminated MXenes. Indeed, for MXenes with F surface groups, it was predicted that the relatively lower V_M formation energies are restored, V_{Ti} lying at around 3.5 eV. According to the calculations, the F groups should be much easier to remove than O groups, with F vacancy formation energies being lower than O ones by several eV. Here, the authors raise a crucial point on the calculation of defect formation energies: the resulting value varies depending on the reference used for the energies of single atoms. As an example, F vacancy formation energies calculated using HF $-\frac{1}{2}H_2$ or $\frac{1}{2}F_2$ as reference for the energy of one F atom yield formation energy differences of circa 3 eV. These references should be considered when comparing the formation energies of atoms of different chemical elements obtained in different studies.

Gouveia et al. also found MXenes that appeared to display unrealistically negative vacancy formation energies of a few tens of eV, along with severe surface deformation, leading to a structure that could hardly be identified as an MXene. This was attributed to the instability of the ABC atomic layer stacking on these materials, motivating the analysis of the ABA-stacked counterparts, which yielded much more moderate vacancy formation energies and maintained the integrity of the MXene lattice[108]. The unstable MXenes in question include the already synthesized Mo_2CF_2 and Mo_2NF_2. Thus, the work of Gouveia et al. showed that, even if these MXenes are produced through exfoliation of an ABC-stacked parent MAX phase, the resulting material will display ABA atomic layer stacking, as observed experimentally[81,82].

Li et al. compared the stability of C vacancies in Ti_2CO_2 with that of clusters of C vacancies, namely C vacancy lines[110]. Four types of vacancies were studied, as shown in Fig. 4: single C vacancies, nearest-neighbor C vacancies, 3-C vacancies along a symmetry plane of the slab, and a full line of C vacancies spanning the whole material. Of these four, the one predicted to be thermodynamically less favorable is the double C vacancy, with a formation energy per C atom of 7.76 eV. On the opposite end of the stability ranking is the full-line vacancy, with a formation energy of 7.63 eV. Furthermore, the calculated binding energies, i.e., the energy of the systems with respect to all its isolated atoms, indicated that the defective Ti_2CO_2 slabs were thermodynamically more stable than the pristine MXene, and therefore might be found experimentally. The calculations also hinted that the electronic and magnetic behavior of the Ti_2CO_2 MXene changes upon introduction of carbon vacancy lines. The pristine material is a semiconductor and displays no magnetism, whereas the introduction of either of the four types of studied defect induces metallic behavior, and magnetism in the case of the one- and three-C vacancies. The absence of a full line of C atoms (Fig. 4) led to the highest conductivity due to the presence of a large amount of dangling bonds around the vacancies. All the defective systems appeared to display higher radiation absorption than pristine Ti_2CO_2 in the infrared region, while the opposite was found for the visible region, and their potential application as anode materials in aqueous or ionic/organic systems was suggested.

The calculated electronic properties of defective MXenes have been found to depend on the exchange-correlation functional used[108,111]. For instance, both the PBE and the HSE06 functionals predict the Ti_2CO_2 MXene to be a semiconductor but, with any kind of single-atom vacancy, the PBE predicts a metallic behavior, while HSE06 yields a small band gap of a few hundredths of an eV. As discussed in ref. 111, discrepancies between semi-local and hybrid functionals arise from two main sources. First, lingering strain in pre-relaxed structures can lead to errors in single-point hybrid-DFT calculations, particularly for extended defects, where strain accumulates across bulk-like regions. Second, the underestimation of band gaps by semi-local functionals can cause spurious defect level mixing with host states, leading to artificial structural changes. These factors suggest that fully relaxing defective MXene structures with hybrid-DFT approaches is crucial to accurately capture their electronic and structural properties. For Ti_2CO_2, the metallic behavior predicted by PBE may reflect such artifacts, while the HSE06 results may provide a more reliable description of defect-induced properties.

The works reviewed above clearly indicate that the band gaps of MXenes can be influenced by the presence of vacancies, which, when introduced in a controlled manner, can lead to tailor-made materials for

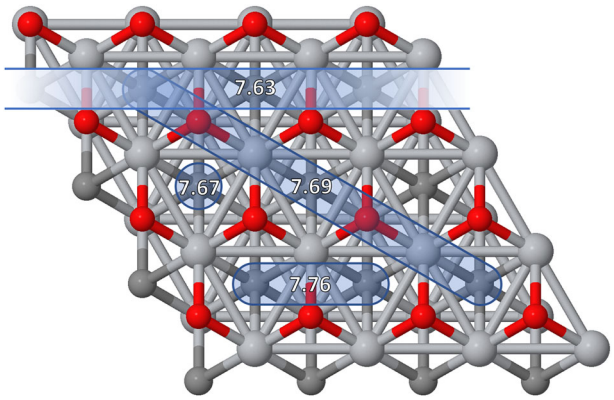

Fig. 4 | Molecular model for the Ti_2CO_2 MXene surface. Top view of the Ti_2CO_2 MXene, assumed infinite along its plane, with values of formation energies of carbon vacancy clusters, per carbon atom, in eV, calculated in ref. 110. The silver-, gray- and red-colored spheres denote atoms of titanium, carbon, and oxygen, respectively. The blue areas denote the studied types of C vacancy clusters: a full line of carbon atoms spanning the whole material (long horizontal rectangle), three carbon atoms contained in a plane of symmetry of the material (slanted blue area), two adjacent carbon atoms (bottommost blue area), or a single carbon vacancy (blue circle).

specific applications. This is exemplified by the work of Tao et al.[112], who successfully synthesized a molybdenum carbide MXene with a significant proportion of metal vacancies, designated as $Mo_{1.33}C$, from a chemically in-plane ordered quaternary MAX phase, specifically $(Mo_{2/3}Sc_{1/3})_2AlC$. Through detailed experimental and computational analyses (using the PBE approach), a close qualitative and quantitative agreement was observed, allowing the conclusion that the structure of $Mo_{1.33}C$ closely resembles that of Mo_2C but with ordered divacancies at every third Mo site. Compared to Mo_2C, the new $Mo_{1.33}C$ MXene exhibits a reduced mass density, along with significantly higher conductivity and volumetric capacitance[112].

Interaction with atoms of transition metal elements

The properties of MXenes can be modified not only by changing their overall structure, like mixing different X or M elements or functionalizing the whole surface, as we have seen, but also by slightly doping the surface with extra atoms (i.e., off-lattice doping). This is a widely recognized method in catalysis, since doping the surface of materials with atoms of another element can induce favorable changes in the electronic structure of the materials that often improve the overall catalytic activity[113]. More recently, the consideration of single atoms of a metallic element deposited onto a substrate, forming a so-called single-atom catalyst (SAC), to improve reaction efficiency and minimize metallic waste[114]. With this in mind, theoretical[115] and experimental[116,117] studies have examined the interaction of MXenes with single transition metal atoms and their effect on catalysis. More recently, systematic first-principles studies, which consider many MXenes and many transition metal elements, have led to the establishment of patterns in the way MXenes interact with atoms of these elements.

In 2021, Oschinski et al. employed a PBE-D3 approach to investigate the interaction of an atom of each of ten different transition metal elements (fourth period of the Periodic Table) with each of nine MXenes with M_2C stoichiometry (M = Ti, Zr, Hf, V, Nb, Ta, Cr, Mo, and W)[118]. The authors of that work discovered that all MXenes behave qualitatively similarly. For example, on all nine MXenes, as one moves along the fourth period of the Periodic Table, the transition metal atom adsorption strength increases up to vanadium, then decreases abruptly for chromium, gradually increases again up to iron, cobalt or nickel, and dips again to its lowest value for zinc. The adsorption was found to be spontaneous and very exothermic, by 2 to 6 eV, for every MXene/metal combination. The Bader charges on the metal adatoms also follow the same pattern for all MXenes: Sc is the most positively charged atom, while Co or Ni are the most negatively charged ones. Intriguingly, despite the very strong transition metal atom adsorption on the MXenes, the potential energy profile on the surface is almost flat in many cases, and their diffusion energy barriers along the surface are rather low, ranging from 0.02 eV for Sc diffusion on Ta_2C, to 0.69 eV for Ti on Cr_2C. Apart from Ti diffusion on Cr_2C, all diffusion energy barriers are lower than 0.36 eV.

Later, Keyhanian et al. conducted a similar study, using the same approach, on nine oxygen-terminated MXenes, with stoichiometry M_2CO_2 (M = Ti, Zr, Hf, V, Nb, Ta, Cr, Mo, and W)[119]. Again, all surfaces examined presented the same qualitative behavior towards transition metal atom adsorption. The preferred adsorption site is the one that allows the adatom to form the most bonds with the surface: three bonds with O and three bonds with M surface atoms. In the presence of the O layer, the adsorption is strongest for Sc (ranging from approximately 4 eV on Hf_2CO_2 and 9.5 eV on Cr_2CO_2), becomes weaker along the first row of transition metals, reaching its lowest for Zn (between approximately 0 eV on Hf_2CO_2 and 2 eV on Cr_2CO_2). The magnitude of the adsorption energies calculated is consistent with those found for adsorption of metal atoms on metal oxide surfaces[120]. All metal atoms become positively charged when adsorbed on M_2CO_2 MXenes, with the strongest adsorption generally being associated to more charge transferred. The calculated diffusion energy barriers are much higher than the ones obtained by Oschinski et al. for the bare MXenes[118], especially for Sc, Ti, and V diffusion. Not surprisingly, the diffusion of the barely adsorbed Zn involves virtually no energy barrier.

The trends in MXene-metal interactions were generalized by Gouveia et al. to transition metal elements of the second and third rows[121]. Taking advantage of the fact that all MXenes display the same qualitative behavior towards transition metal adsorption, Gouveia et al. considered only the Ti_2C and Ti_2CO_2 MXenes, since these are the most studied ones, and thirty different metal elements. On Ti_2C, metals of the second and third rows adsorb on the same surface sites as the corresponding ones of the first row: a bridge site for groups 3–5 of the Periodic Table, a hollow site above a C surface atom for groups 6–10, and a hollow site above a Ti atom for groups 11 and 12. This suggests that the most favorable adsorption site is related to the filling of the *d* subshell of the transition metal atoms. On Ti_2CO_2, most atoms adsorb in a position that allows them to form three bonds with Ti and three bonds with O, in agreement with the findings of Keyhanian et al.[119].

In terms of adsorption strength on Ti_2C, as shown in Fig. 5, the behavior of the atoms of the three transition metal rows predicted by Gouveia et al. was found to be quite different but, on each row, the adsorption is still strongest for the Fe, Co, and Ni group, and weakest for atoms of the Zn group[121]. The latter is also true for Ti_2CO_2, but on this MXene the adsorption is strongest for the first metals of each period, and simply becomes weaker along each period. Figure 5 also shows the amount of charge transferred between the MXene surfaces and each transition metal atom. One can observe that, for all three periods, stronger adsorption is roughly accompanied by more charge transferred. This is especially noticeable on Ti_2CO_2, where all Bader charges are positive, indicating a transfer of electrons from the metal atom to the MXene. This is justified by the presence of oxygen, the second most electronegative element of the Periodic Table.

The diffusion energy barriers of transition metal atoms on Ti_2C were predicted to be lower for atoms at the leftmost and rightmost ends of each period of the Periodic Table and were calculated at 0.25 eV (for Ir) at most[121]. All studies agree that, on Ti_2CO_2, these diffusion barriers are much higher, but decrease along each period, thus following the same trend as the adsorption strength. The high barriers predicted for transition metal atom diffusion on Ti_2CO_2 were attributed to the difficult process of the metal adatom breaking three metal-Ti in order to travel over the O layer and bond with three distinct Ti atoms in a neighboring unit cell (see Fig. 6). This difficulty does not occur in the bare Ti_2C, on which diffusion only requires breaking one metal-Ti bond at a time while keeping the other two intact. The stability of the MXene/metal systems demonstrated in all the studies presented in this section paved the way for the potential development of MXene-supported single-atom catalysts with unique properties.

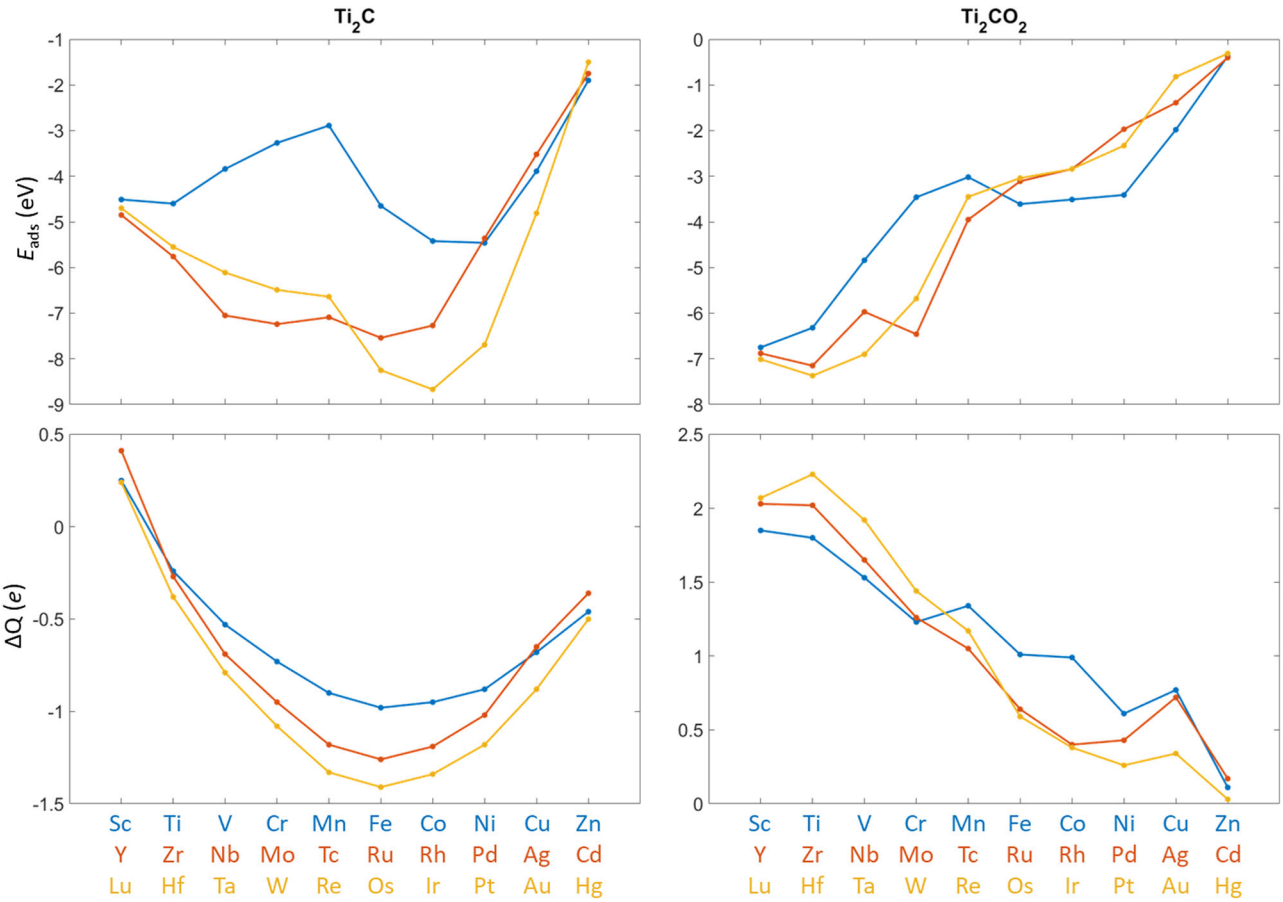

Fig. 5 | Adsorption energies and charges for metals on titanium carbide surfaces. Adsorption energies (E_{ads}, top panels) and Bader charge (ΔQ, bottom panels) of transition metal atoms adsorbed on Ti_2C (left-hand side) and Ti_2CO_2 (right-hand side) MXene surfaces. Values taken from ref. 121.

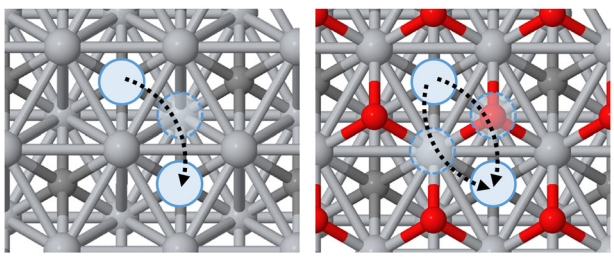

Fig. 6 | Diffusion mechanism of metals on titanium carbide surfaces. Illustrations of the diffusion mechanism of a transition metal atom adsorbed on Ti_2C (left-hand side) or Ti_2CO_2 (right-hand side), starting from a hollow site above a carbon atom, and ending in a neighboring equivalent position, following the path represented by the arrows. Titanium atoms are represented in silver color, carbon in gray, oxygen in red, and the metal atom in blue. The semi-transparent blue circles are intermediate metastable states of the diffusion.

Prediction of synthesizable MAX phases and MXenes

Although tens of MAX phases and MXenes have been realized, hundreds have been predicted to be synthesizable. In 2021, Khaledialidusti et al. used a DFT-based computational method, with the PBE functional, to estimate the stability of MAX phases, each composed of one of 11 M elements, one of 17 A elements, C or N, and $n = 1$, 2 or 3, for 1122 MAX phase candidates. Khaledialidusti To this end, the phonon dispersion and formation energy of the MAX structures were calculated. The first of these quantities is related to the second-order derivative of the energy of the system with respect to the atomic positions and was employed to assess the dynamic stability of the materials. In turn, the formation energy is a measure of how stable the configuration of the system is when compared to other configurations. In practice, to be considered locally and thermodynamically stable, a MAX phase should display the absence of modes with imaginary wavenumbers and negative formation energy.

The formation energy criterium was found to be much more restrictive than the phonon dispersion, in the sense that all the M/A/X/n combinations that did not meet the phonon dispersion criterium, did not meet the formation energy one either. This suggests that future studies could in principle restrict themselves to calculating formation energies to arrive at reliable conclusions. In short, MAX phases were predicted to be more stable when i) the M element belongs to group 4 or 5 of the Periodic Table; ii) the A element is not Si, P, S, Cu, or Ir; iii) the X element is C. A total of 466 MAX phases were predicted to be synthesizable, where the number of carbides is more than twice that of nitrides. This is around 3 times as many as the number of MAX phases that have actually been realized.

Encouragingly, from the calculated force constants between the M and A elements and between the M and X elements, Khaledialidusti et al.[70] observed that the M-A bonds are much weaker, as expected, since the way MXenes are traditionally produced is precisely by breaking the M-A bonds in MAX phases[2]. The thermodynamic stability of the resulting MXenes, relative to the precursor MAX phase, was assessed by calculating the exfoliation energy. Weak M-A forces and thermodynamic stability of MXenes with respect to the precursor MAX phases were used as criteria to establish 136 MAX phases as the ones that can be exfoliated to produce 26 MXenes, shown in Table 1. Note that 12 of these 26 had already been manufactured at the time of the prediction, but others came to be synthesized later, such as Ta_2C[122], Cr_2C[123], V_2N[124], and Ti_4C_3[125].

DFT calculations have been employed to propose alternative ways of synthesizing MXenes, such as epitaxial growth. By taking advantage of the

Table 1 | The 26 synthesizable MXenes, and corresponding precursor MAX phase A elements, predicted by the DFT calculations in ref. 70

MXene	Precursor MAX phase A element
Ti_2C	Al Ga Ge Si
Zr_2C	Si
Hf_2C	Al Ga Ge In Si
V_2C	Al Au Cd Zn Ga
Nb_2C	Al Au Cd Ga In Ir Tl Zn
Ta_2C	Al Au Ga In Zn
Cr_2C	Au Ga Zn
Mo_2C	Al Zn
Ti_2N	Al Ga
Hf_2N	Al
V_2N	Zn
Ti_3C_2	Al Au Cd Ga Ge In Ir Si Tl Zn
Zr_3C_2	Al
Hf_3C_2	Al Au Cd Cu Ga Ge In Ir Pb Si Sn Tl Zn
V_3C_2	Al Au Cd Ga Zn
Nb_3C_2	Al Au Cd Ga Ge In Ir Tl Zn
Ta_3C_2	Al Au Cd Ga Ir Zn
Ti_3N_2	Al Zn
Hf_3N_2	Al
Ti_4C_3	Al As Au Cd Ga Ge In Ir Si Tl Zn
Zr_4C_3	Al Cd Ga In Ir Si Zn
Hf_4C_3	Al Au Bi Cd Ga Ge In Ir Pb Si Sn Tl Zn
V_4C_3	Al Ga Zn
Nb_4C_3	Al Au Cd Ga Ge In Ir Sn Tl
Ta_4C_3	Al Au Cd Ga In Ir Tl Zn
Ti_4N_3	Al Ga

The MXenes highlighted in bold font had already been experimentally synthesized at the time of publication, while those in italic font have since been successfully prepared.

excellent capabilities of MXenes for dissociating nitrogen[126], Gouveia et al. suggested obtaining thicker MXenes experimentally by depositing alternating layers of nitrogen and a metallic element over a thinner precursor MXene[98]. For this to be realizable, a series of steps must be thermodynamically and kinetically favorable, such as exothermic metallic atom adsorption. The limiting step was determined to be the adsorption and dissociation of N_2 on the nearly fully N-covered MXenes, predicted to be achievable for nearly half of the 18 considered MXene seeds. These results are useful as guidelines for experimentalists, as they provide the most likely obtainable MXenes, as well as the most probable paths for obtaining them.

Prediction of new MXenes and their properties

Despite not having been synthesized to date, the Hf_2C MXene has attracted the attention of plenty of theoretical studies, possibly because Ti_3C_2 was the first to be synthesized, Zr_3C_2 was realized a few years later[127], and therefore MXenes based on the next transition metal of this group of the Periodic Table, Hf, are expected to be stable.

Liu et al. compared the electronic properties of Hf_2CT_2, with six different surface terminations (T = O, S, Se, F, Cl, OH), with those of the bare Hf_2C MXene, using the PBE-D3 method[128]. The geometries of the six terminated materials were predicted to be qualitatively the same, with the functional groups adsorbed on hollow sites over Hf atoms. The lattice constant of Hf_2C was predicted to increase with surface termination, from 3.20 Å on pristine Hf_2C, up to 3.45 Å on Hf_2CSe_2. Results for Hf_2CSe_2 were later confirmed by the calculations of Jasani et al., using the PBE exchange-correlation functional without dispersion corrections, and some elastic properties of this theoretically predicted material were calculated[129]. By comparing the binding energies, any Hf_2CT_2 surface was predicted to be more stable than the clean one, with emphasis on Hf_2CO_2, which displays the lowest binding energy by far. This was an expected result, as MXenes are known to be very oxophilic. The Hf_2CT_2 MXene was found to be metallic both with and without any surface termination, apart from Hf_2CO_2, which has a semiconductor indirect band gap of 1.0 eV. Functional groups other than O shift the Fermi level into the conduction band, inducing a semiconductor-to-metal transition. The Hf_2CCl_2 and Hf_2CF_2 systems have work functions (the difference between the vacuum energy and the Fermi energy) considerably smaller (3.78 and 3.59 eV) than those of the other studied functionalized surfaces (5.36 to 8.84 eV), and therefore were proposed as applicable in thermionic and electron emission devices. The functionalization of Hf_2C was found to eliminate the magnetism inherent to the clean surface and change the type of electrode. In particular, the Cl-, OH-, and F-terminated Hf_2C MXenes are potential anode materials, while O-, S-, and Se-terminated ones are potential cathode materials.

The authors of ref. 128. additionally considered the effect of mixed O, OH, and F surface terminations, which are known to occur experimentally. Three different ratios were studied: while keeping the OH content at 0.11, the O/F stoichiometric coefficients considered were 0.28/1.61, 0.78/1.11, and 1.61/0.28. Because of the presence of F and OH, all three mixed-termination MXenes displayed metallic behavior, implying that, in reality, Hf_2CT_2 is most likely a metal, even if most of its surface termination is composed of O adatoms. The lattice constant, density of states and work function of the $Ti_3C_2T_2$ and V_2CT_2 MXenes with mixed O, OH, and F terminations were predicted to be very well modeled by a weighted average of the same properties of their uniformly terminated counterparts[130].

In a subsequent study, Liu et al. investigated the effect of substituting C atoms by N ones (i.e., in-lattice doping) in the Hf_2CO_2 MXene[131]. This was again done using the DFT-D3 method and a 3 × 3 supercell of the material, so that ten different N/C ratios (0/9, 1/8, 2/7, …, 9/0) were considered. In terms of structural stability, the lattice constant was found to decrease as the N doping amount increases, so that when all C's are replaced by N, the lattice constant is 1.5% smaller than on pristine Hf_2CO_2. However, in terms of binding energy, the calculations showed that the stability of the system is reduced as N doping increases, ultimately making Hf_2NO_2 less stable than Hf_2CO_2 by around 0.2 eV per atom. The semiconductor behavior of Hf_2CO_2 was found to disappear even with the smallest finite N/C ratio, due to the Fermi level rising above the conduction band minimum. Calculations of the surface storage charge suggested that Hf_2CO_2 is a potential cathode material, while the slightest N doping turns the MXene into a potential anode material. Interestingly, as the N doping amount increases, the surface tends to become a symmetric electrode, implying that tuning the N concentration should yield any desired type of electrode. Once again, a mixture of surface terminations was considered as well, $Hf_2CO_{0.42}F_{1.19}(OH)_{0.39}$, for comparison with the purely O-terminated MXene. The semiconductor character of the Hf_2CO_2 MXene was concluded to be exclusive to this pristine material, since the replacement of even a minor amount of C by N, or of the O surface termination by other species or a mixture of O, F, and OH turns the MXene into a metal.

In 2022, 10 years after the isolation of the first MXene, Michałowski et al. synthesized samples of the Ti_3AlC_2, Mo_2TiAlC_2, and Cr_2TiAlC_2 MAX phases and the $Ti_3C_2T_x$ MXene using traditional methods, and analyzed them using secondary ion mass spectroscopy (SIMS), thus studying their structure at the atomic level[132]. They discovered that there was oxygen present amid the carbon layers of both classes of materials. The oxygen content was considerable even on the MXene, amounting to 30% replacement of the carbon atoms with oxygen ones, yielding a $Ti_3C_{1.4}O_{0.6}$ stoichiometry. This led to the suggestion that, most likely, nearly all carbide MXenes produced to date are in fact oxycarbides. Taking inspiration from this finding, Gouveia and Gomes studied the structural and energetic stability of substitutional oxygen on the Ti_3C_2 MXene for several oxygen concentrations, using the PBE-D3 approach[133]. The calculations showed that, at least up to 75% replacement of carbon content with oxygen one, the substitution is exothermic and the resulting $Ti_3C_{2-x}O_x$ MXene structure is indistinguishable from that of the pristine Ti_3C_2 MXene, explaining the difficulty and delay in experimentally identifying the oxycarbide. The $Ti_3C_{2-x}O_x$ MXenes were also predicted to display metallic behavior independently of the oxygen concentration on the carbon layer. If all carbon is replaced by oxygen, the resulting Ti_3O_2 2D material is no longer stable with its original ABC atomic layer stacking and should transition to an ABA

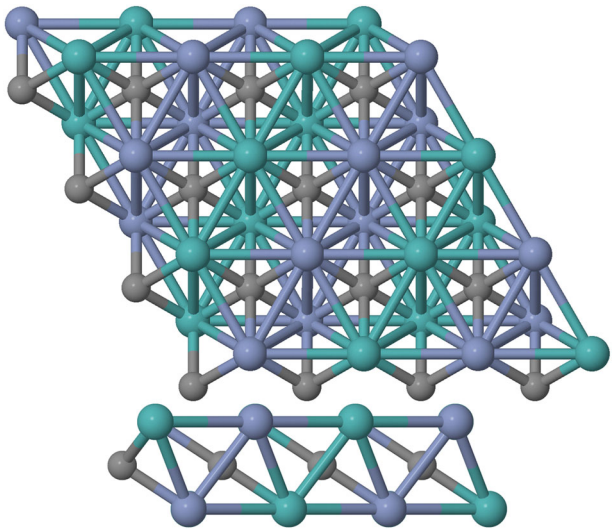

Fig. 7 | Molecular model for the TiVC bimetallic MXene surface. Top and side views of the optimal configuration of the TiVC bimetallic MXene surface, as obtained in ref. 136. The spheres represent atoms of Ti (blue), V (green), or C (gray).

phase, which is more stable than ABC by 0.37 eV per formula unit. As a consequence, Ti_3O_2 became the first material derived from a Ti-based MXene to prefer the ABA layer alignment, confirming the postulate by Gouveia et al., that the ABA phase of MXenes is stabilized and driven by a higher electronic density of the material[86].

In a more recent study, Michałowski et al. developed a protocol for deconvoluting SIMS data, enabling the quantitative analysis of the composition of individual MXene atomic layers[134]. This advancement allowed for the distinct detection of not only oxycarbide MXenes but also oxynitride and oxycarbonitride MXenes. Notably, analysis of multiple MXene samples revealed that some could achieve high oxygen concentrations (>65%) in the X layer, corroborating earlier theoretical predictions by Gouveia and Gomes[133].

Simultaneously, Gouveia and Gomes[135] examined the effects of subsurface substitutional oxygen atoms on the structural, energetic, and electronic properties of MXenes with varying M, X, and T elements. They studied MXenes of the form M_2XT_2, with M = Ti or V; X = C or N; and T = none, O, or F, which, when compared with their earlier work on the Ti_3C_2 MXene[133], also allowed them to analyze the influence of MXene thickness. Their findings demonstrate that subsurface O is thermodynamically stable in any concentration across all analyzed MXenes. On bare Ti_2C, subsurface O atoms migrate to the surface, forming carbon vacancies and localized O terminations. The results in their work[135], align with experimental evidence suggesting that all synthesized MXenes may, in fact, be oxycarbides or oxynitrides[134]. Furthermore, they also suggested that conditions that remove surface terminations are likely to induce significant X-layer vacancies. Notably, O-terminated nitride MXenes (M_2NO_2, M = Ti or V) exhibit spontaneous distortions, whereas pristine O-terminated carbide MXenes (M_2CO_2, M = Ti or V) retain hexagonal symmetry unless subsurface O exceeds ~75 %. Fluorine terminations stabilize hexagonal structures, even in nitride MXenes, making F-based synthesis routes particularly suitable for these materials. Electronic analyses revealed that pristine MXenes are metallic, except for the semiconducting Ti_2CO_2, whose band gap is influenced by subsurface O. While PBE predicted a loss of semiconducting behavior at low O concentrations, HSE06 suggested that the material remains semiconducting, albeit with increased conductivity as the O content rises[135].

Even though most MXene research focuses on those made of a single M element, multimetallic MXenes have been synthesized. The possibility of controlling the multimetallic composition of MXenes paves the way for even broader applicability of this family of materials. One such MXene is TiVC, which was first synthesized in 2022[136]. Sometime later, a theoretical study by Zhang et al. examined the structural properties of $TiVCT_x$ considering different surface terminations (F, O, and OH), using the PBE functional[137]. Different relative positions of the Ti and V atoms were considered, and the most asymmetric one, shown in Fig. 7, was deemed the most stable. As is usual with ABC-stacked MXenes, the F, O, or OH terminal groups prefer being placed on surface hollow sites above a metallic atom. The frequencies of the Raman- and infrared-active vibrational modes of the system were calculated for comparison with the ones obtained experimentally. According to the calculations, the functionalization of the TiVC surface introduces new active modes and considerably changes the vibrational frequencies of the existing ones, as shown in Table 2. With this information and the experimental data from ref. 136, it was concluded that the surface termination of the as-synthesized TiVC MXene was composed of F and OH groups, as demonstrated by the very small deviation between the frequencies calculated for TiVCF(OH) and the experimentally measured ones.

MXenes as catalysts

Every chemical reaction follows a different mechanism, involving relocation of atomic nuclei and redistribution of electronic charge, to break some chemical bonds and form new ones. More often than not, somewhere along the reaction path, there are intermediate states of the system that are less stable than the reactants in their initial state, which is more likely to happen if the initial bonds are stronger. The least stable of these states is called the reaction transition state. This means that, for the products of the reaction to be formed, the system needs to overcome an energy barrier, called the reaction activation energy, which can be defined as the difference between the energy of the system in the reaction transition state and in its initial state. An analogy with an everyday phenomenon could be the toppling of an object: even though the object is more stable when toppled than when sitting upright, one needs to tilt the object by a certain minimum amount, in order to cause gravity to spontaneously pull it towards the toppled position. Likewise, chemical reactions can be facilitated by the presence of a third party, a catalyst. The catalytic process starts with the catalyst forming chemical bonds with the reactants, weakening the existing bonds within the reactants. Secondly, an external energy source provides enough energy to break the weakened bonds. Then, new bonds are formed, giving rise to the products of the reaction. Finally, the catalyst is regenerated by removing the reaction products, and can be used again. Thus, a suitable catalyst for a given reaction should be able to bind to the reactants, should effectively lower the reaction activation energy, should preferably be selective towards the desired reaction products and not competing side reactions that may occur, and should not be too strongly bound to the products, allowing their separation after the reaction has taken place. Different catalytic categories use different energy sources to overcome the reaction activation energy: thermal catalysis uses temperature, photocatalysis uses electromagnetic radiation, and electrocatalysis uses an external voltage.

Thermal catalysis

Since MXenes are solids, they can serve as catalysts in heterogeneous catalysis, i.e., catalysis in which the phase of the catalyst is different from the phase of the reactants or products. Here, the MXene is the (solid) catalyst and the reaction of interest involves gases. From the theoretical point of view, in particular at the DFT level, assessing the suitability of an MXene for use in catalysis consists of calculating the reactant adsorption energies on the surface, calculating the activation energy for the reaction to occur (which should be lower than in the gas phase), and calculating the adsorption energy of the products.

Mathematically, in a catalyzed reaction, the initial and final states of the system correspond to energy minima with respect to atomic positions, but the transition state is a saddle point of the potential energy surface, and these are much harder to find. Two common methods are the dimer and the nudged elastic band (NEB) methods. Both approaches attempt to find saddle-point system configurations. To use the dimer method, one can take the initial state of the system and manually change the coordinates of the

Table 2 | Frequencies of the local vibrational modes, in cm^{-1}, of the $TiVCT_x$ MXene with different surface terminations, calculated in ref. 137 and measured in ref. 136

	TiVC	$TiVCF_2$	$TiVC(OH)_2$	TiVCO(OH)	TiVCFO	TiVCF(OH)	Experiment
A_1	569.7	638.3	3625.2	3641.3	716.4	3642.7	3600 (1%)
A_1	329.9	519.4	3602.3	692.6	594.0	677.9	670 (1%)
A_1		453.4	664.5	602.0	471.6	555.6	540 (3%)
A_1		262.7	561.1	505.1	308.3	480.1	475 (1%)
A_1			499.8	286.2		276.8	
A_1			295.0				
E	667.9	696.3	749.0	604.2	644.6	737.9	
E	230.3	281.0	418.3	404.3	366.9	387.5	400 (−3%)
E		226.9	401.2	367.0	186.3	333.2	325 (3%)
E		191.0	329.8	237.2	142.9	234.8	250 (−6%)
E			306.5	152.8		199.7	195 (2%)
E			211.1				

The first column indicates the mode type and the first row the surface termination. The percentage deviation of the values calculated for TiVCF(OH) from the experimental values is shown in parenthesis.

atoms of interest for the reaction, moving them in the direction that one expects them to go for the reaction to take place. For example, to study the catalysis of H_2 dissociation on a solid surface, one would first find the ground state adsorption configuration of H_2 on the surface, then change the atomic coordinates of the H atoms so that they are slightly farther from each other, and use the resulting configuration as input for the dimer calculation. The NEB method is computationally more expensive and requires the knowledge of the final state of the system, but is more likely to find a saddle point than dimer. Instead of using only one configuration as input, NEB uses several configurations (images), resulting from linear interpolation of the atomic positions between the initial and final states. The method then optimizes all the images simultaneously while keeping equal spacing between consecutive ones. Herein, we present some examples of recent works that reveal the sort of information that DFT calculations can provide in this field.

Dehydrogenation of propane

The dehydrogenation of propane catalyzed by the $Ti_2CO_{2-x}(OH)_x$ MXene, i.e., the Ti_2C MXene with a surface termination consisting of some O groups and some OH groups, was studied by Liu et al. using the van der Waals density functional (vdW-DF), an exchange-correlation functional augmented with van der Waals corrections[138,139]. The reaction transition states were found by a combination of the NEB and dimer methods: first, the initial and final states of the system (hydrogenated and dehydrogenated propane adsorbed on the MXene) were found, then a NEB calculation with 10 intermediate images provided the dehydrogenation reaction path, and finally the central images were used as dimer inputs for obtaining more accurate transition states. On the purely O-terminated surface, Ti_2CO_2, the dehydrogenation of the CH_2 group of propane was predicted to be easier than that of a CH_3 group, since the former requires surpassing an energy barrier of 1.60 eV while the latter has a higher one, 2.01 eV[140]. The authors then built 24 different $Ti_2CO_{2-x}(OH)_x$ MXene models, with varying OH/O fraction and distribution, and calculated the propane activation energy on each, shown in Fig. 8. As seen in this Figure, different arrangements of the same fraction of OH and O groups can lead to very different activation energy values, implying that the OH fraction is not a good descriptor. However, the activation energies were found to correlate linearly with the corresponding reaction energies, as in a Brønsted–Evans–Polanyi (BEP, also shown in Fig. 8) relationship, and with a more useful physical quantity, the surface hydrogen affinity. This can be roughly defined as the adsorption energy of a hydrogen atom, and was determined to also strongly depend on the surface termination group distribution, since the highest and lowest calculated hydrogen affinities were found for the same fraction of OH groups (43.75%). Unsurprisingly, the $Ti_2CO_{2-x}(OH)_x$ MXene models that were predicted to more strongly adsorb hydrogen atoms were the ones with the lowest fraction of OH groups, and yielded the lowest activation energies for propane dehydrogenation on average. The linear relation obtained allows the estimation of dehydrogenation activation energies as a function of the hydrogen affinity, with a mean absolute error lower than 0.2 eV, both at the CH_3 and CH_2 group. Unlike reaction energies, the hydrogen affinity is an intrinsic property of the material and can therefore be measured experimentally and used to predict the suitability of an MXene for alkane dehydrogenation.

Dehydrogenation of methylcyclohexane

Bare MXenes, i.e., MXenes without surface functionalization, have their outer metallic layers exposed and are known to be very reactive, spontaneously dissociating many molecules[80,141,142]. Other species, e.g., CO_2, adsorb on the bare surface without dissociating spontaneously as predicted computationally[143], despite the low calculated dissociation energy barriers, and observed experimentally[144]. This can be useful when the molecule dissociates in the desired way, but it becomes harmful if the molecule is completely disintegrated. The latter was predicted to be an expected outcome if one attempts to dehydrogenate methylcyclohexane to toluene using a bare Ti_3C_2 MXene surface[145]. According to the DFT-PBE calculations of Obodo et al., attempting to catalyze this reaction using Ti_3C_2 would result in a too exothermic process that destroys the molecule and deactivates the surface. However, after depositing layers of Pt over the MXene surface, which has been shown to be experimentally feasible[146], the calculations showed that the reactivity of the material becomes much more moderate. By simulating the presence of one, two, or three Pt layers over Ti_3C_2, Obodo et al. noticed that the reaction becomes endothermic, but the endothermicity is reduced as the number of Pt layers increases. With as few as three Pt layers, the catalytic activity is already improved with respect to the Pt(111) surface.

Dissociation of nitrogen

Armed with the knowledge of the high reactivity of bare MXenes towards most molecules, Gouveia et al. built models of 18 MXenes and performed DFT-based calculations, using the PBE-D3 exchange-correlation functional, to study N_2 dissociation on their surfaces[126]. This is an important reaction, involved in the Haber-Bosch process for industrial production of ammonia. In fact, N_2 dissociation is the rate-limiting step of ammonia synthesis, because it involves breaking a triple N-N bond, which in gas phase would require around 10 eV of energy. N_2 was found to exothermically adsorb and dissociate on all the studied surfaces. The calculated activation energies are shown in Table 3. Notice that even the highest one represents a decrease of nearly 90 % with respect to gas phase dissociation. Some MXenes were therefore predicted to display N_2 dissociation energy barriers lower

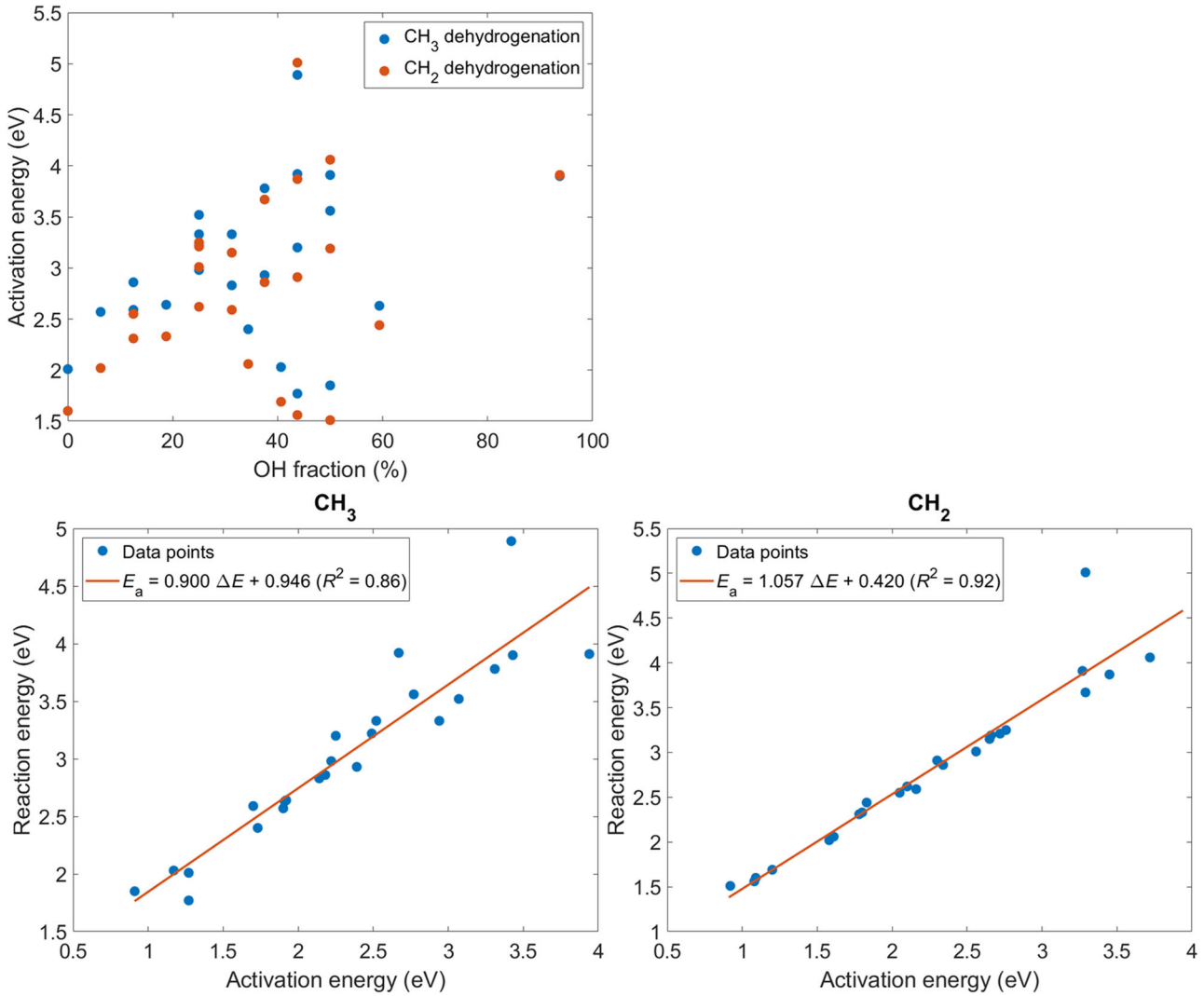

Fig. 8 | Activation and reaction energies for propane dehydrogenation. (Top panel) Activation energy for propane dehydrogenation via a CH_3 (blue points) or the CH_2 (orange points) group, catalyzed by the $Ti_2CO_{2-x}(OH)_x$ MXene as a function of the percentage of the O surface termination that is replaced by OH groups. (Bottom panels) Brønsted–Evans–Polanyi (BEP) correlations between the reaction energies energies (ΔE) and activation energies (E_a) for propane dehydrogenation via a CH_3 (left-hand side) or the CH_2 (right-hand side) group. Data from ref. 140.

than those found for some of the established catalysts for this reaction, such as Fe(111) or Ru nanoparticles, with energy barriers of circa 0.80 eV and 0.4–1.9 eV, respectively[147,148]. The lowest value is achieved by the W_2N MXene, which has not been experimentally realized yet. The exothermic reaction energies correlate reasonably well with the activation energies, an occurrence known as Brønsted−Evans−Polanyi relationship[149–151]. In order to form NH_3 using MXenes, the successive hydrogenations of the adsorbed N adatoms become the rate-limiting steps, which are endothermic and involve energy barriers between 1.24 and 1.70 eV, suggesting that MXenes would have to be used as co-catalysts with, for example, Ru nanoparticles, in the Haber–Bosch process. An alternative pathway, such as the Mars-van Krevelen mechanism[152,153], might be feasible for producing ammonia since the successive dissociation of N_2 molecules on the MXene surfaces has been predicted to create a nitrogen adlayer[98].

In their study of N_2 dissociation on bare MXenes[126], Gouveia et al. observed that MXenes composed of an M element of group 6 of the Periodic Table became distorted in the vicinity of the adsorbed molecule, in agreement with previous predictions by Shao et al.[154]. This led them to investigate whether this happened due to an attempt by the surface to transition to another more stable phase, which they found to consist of an ABA atomic layer stacking, instead of the usual ABC one found on most MXenes[86]. This stacking is more stable than the traditional one for 8 out of the 18 MXenes that were analyzed and this was found to have consequences on their catalytic activity. For example, according to the calculations, the ABA-stacked W_2N MXene presented an N_2 dissociation energy barrier, of 0.18 eV, which is even lower than the 0.28 eV found for ABC stacking. The former signifies a reduction of over 96% with respect to the gaseous phase barrier.

Water-gas shift reaction

The dissociation of water molecules is often the rate-limiting step in processes such as the water-gas shift reaction or the hydrogen evolution reaction[155–158]. The former is a very important process involved in the industrial production of hydrogen. The DFT calculations of Gouveia et al. showed that 18 studied MXenes greatly facilitate the water dissociation step by reducing the activation energy of the first O-H bond breaking to almost zero[159]. In particular, MXenes made of an M element from group 4 of the Periodic Table (Ti, Zr, or Hf) display water dissociation energy barriers below 0.1 eV. The energy barriers and reaction energies follow a BEP relationship, as in the case of N_2 dissociation by MXenes[126]. However, it was predicted that water dissociation would be too exothermic, for example when compared with metallic surfaces[160–162], which would be a major problem for regenerating the catalyst by desorbing the products of the reaction.

Table 3 | Energy barriers for N_2 dissociation catalyzed by bare MXenes taken from Gouveia et al.[126]

Carbides			Nitrides		
Ti	**V**	**Cr**	**Ti**	**V**	**Cr**
0.98	0.80	0.85 (0.78)	0.93	0.78	0.61 (0.61)
Zr	**Nb**	**Mo**	**Zr**	**Nb**	**Mo**
1.10	0.75	0.93 (0.62)	0.91	0.60 (0.78)	0.45 (0.41)
Hf	**Ta**	**W**	**Hf**	**Ta**	**W**
0.96	0.53	0.37 (0.37)	0.75	0.48 (0.54)	0.28 (0.18)

The values in parenthesis correspond to ABA-stacked MXenes, as found in ref.86
Eighteen MXene surfaces are considered, with the M element written in bold font. Lower or higher values are placed over backgrounds with colors closer to green or red, respectively.

Table 4 | Adsorption energies (E_{ads}), dissociation energy barriers (E_{barr}), and dissociation reaction energies (E_{reac}), in eV, of a water molecule on the Mo_2C MXene, with different surface terminations, as calculated by Gouveia et al.[82]

Termination	E_{ads}	E_{barr}	E_{reac}
None	−0.62	0.41	−1.39
O_2	−0.20	2.50	2.33
F_2	−0.13	0.31	−1.06
$O_{0.13}F_{1.63}$	−0.73	0.14	−0.52
$O_{0.25}F_{1.38}$	−0.41	0.20	−0.69

The hope of using MXenes to catalyze the water-gas shift reaction was restored by Deeva et al., who synthesized the molybdenum carbide MXene and used it to catalyze this reaction[81]. These authors prepared three different samples, namely, Mo_2CT_x, where F has the highest fraction of terminating groups, and two partially reduced Mo_2CT_x-500 and Mo_2CT_x-800 obtained from the former sample, using 20 vol% H_2 in N_2 at 500 and 800 °C, respectively. Under water gas shift conditions, the oxophilic nature of partially reduced samples leads them to be covered with oxygen, which was suggested to reduce the catalytic activity[81]. With these results in mind, Gouveia et al. conducted another DFT-based study, this time including Mo_2C models that had surface functionalization[82]. The dissociation of a water molecule was studied on five different models, mimicking five different regions of the MXene: a model with no surface termination, a model with Mo_2C fully covered by O (Mo_2CO_2), a model with full F termination (Mo_2CF_2), and two models in which the F termination is partially replaced by one or two O adatoms ($Mo_2CO_{0.13}F_{1.63}$ or $Mo_2CO_{0.25}F_{1.38}$, respectively). The models were inspired by the results of Deeva et al., which stated that the surface of the synthesized material was functionalized by mostly (70%) fluorine adatoms (i.e., $Mo_2CF_{1.4}T_x$). The quantitative results are summarized in Table 4. On the bare Mo_2C, water was predicted to adsorb exothermically and require a low energy barrier to dissociate, but the products (OH and H) remain too tightly bound to the surface. On Mo_2CO_2 and Mo_2CF_2, water weakly physisorbs relatively far from the surface, with adsorption energies of −0.20 and −0.13 eV, respectively. On Mo_2CO_2, this is not enough to activate an O-H bond, since the energy required to break it on this surface is 2.50 eV. In contrast, the Mo_2CF_2 actually reduces the activation energy to 0.31 eV, although this is higher than the absolute value of the adsorption energy on this surface, implying that water is more likely to desorb again instead of dissociating. The issue with water dissociation on Mo_2CF_2 is that, when the H atom binds to a surface F atom, an HF molecule is released, and the surface termination is locally replaced by OH. These qualitative findings for water dissociation on Mo_2C, Mo_2CO_2, and Mo_2CF_2 motivated the development of the mixed-termination models, since the following rules became apparent: i) the MXene cannot be bare, since that leads to irreversible surface poisoning; ii) the surface termination cannot be comprised of too much oxygen, since regions fully functionalized by oxygen are inert towards adsorption and dissociation; and iii) the surface termination cannot be made solely of F adatoms, since this termination is removed in the form of HF upon water dissociation, damaging the surface. According to the calculations of Gouveia et al., the local replacement of F adatoms by one or two O groups creates a section of the Mo_2C MXene that is reactive enough to exothermically adsorb water and dissociate it, with energy barriers of 0.14 or 0.20 eV, respectively, without being damaged in the process or leading to reaction products that are too stable. The products are hydroxyl groups that remain adsorbed on the surface, but not on their thermodynamically most favorable adsorption site, which may increase their reactivity for the following steps of processes that begin with the dissociation of water. This study showed that the synthesis of MXenes by HF etching of the A element of a MAX phase leads to a surface that is mostly covered by F, which is partially replaced by O, and that the resulting surface composition is fortuitously adequate for catalyzing the dissociation of water molecules.

The previous paragraphs illustrate just a few examples of how easy it is for bare MXenes to dissociate adsorbed molecules, and therefore how hard it usually is to form new molecules on these surfaces. We now proceed to describe this contrast on MXenes, namely for CO_2 dissociation and CO oxidation.

Carbon dioxide reduction and carbon monoxide oxidation

Morales-Salvador et al. used the PBE-D3 exchange-correlation functional to show that 18 MXenes very easily dissociate CO_2 molecules into CO+O, with Mo_2N, Hf_2N, and V_2C eliminating the energy barrier entirely[143]. The CO_2 adsorption and dissociation were studied not only on the bare MXenes but also on Ti_2CO_2 and Mo_2NO_2 with a small bare region where three O adatoms have been removed. Even in this small area, the CO_2 dissociation energy barriers were predicted to be as low as 0.14 and 0.01 eV, and the desorption energy of the resulting CO became 0.29 and 1.75 eV, respectively. The results showed that, after dissociating CO_2, the MXenes ultimately become covered by an oxygen terminating layer, which is known to be removable by hydrogenation into H_2O, regenerating the catalyst. Parey et al. extended these results to MXenes with vacancy defects, again using a DFT-based PDE-D3 methodology[109]. Three types of vacancies were considered: M vacancies, C/N vacancies and MC/MN vacancies. The latter was predicted to require the most energy to be formed, in agreement with the calculations of Gouveia et al.[108], whereas C/N vacancies are thermodynamically the easiest to form. The CO_2 molecule was found to adsorb more strongly on most defective MXenes than on the pure ones (i.e., CO_2 is attracted to the vacancies), most notably on the C/N-defective V_2C, Nb_2C, Ti_2N, V_2N, Zr_2N, and Mo_2N MXenes, on which CO_2 dissociates spontaneously. Since the C/N vacancies are the most likely to occur, this means that the list of MXenes that spontaneously dissociate CO_2 in the laboratory should be even larger than the one predicted by Morales-Salvador et al.[143]

The reverse process, i.e., CO oxidation, is unfeasible on bare MXenes, given the almost non-existing energy barrier and clear exothermicity of CO_2 dissociation on these surfaces. Two recent theoretical works used a DFT-D3 approach to predict the feasibility of CO oxidation on transition metal single-atom catalysts based on the surface-functionalized Ti_2C MXene. Zhu et al. analyzed the potential of single Fe atoms deposited on the Ti_2CO_2 MXene surface (Fe/Ti_2CO_2) for CO and O_2 adsorption, and then for CO oxidation[163]. The CO molecule was found to exothermically adsorb on the Fe/Ti_2CO_2, with an adsorption energy of −1.16 eV, clearly differing from the undoped Ti_2CO_2, which is known to barely adsorb even the smallest molecules[80,142,164,165]. Curiously, Fe/Ti_2CO_2 can even adsorb two more CO molecules, with subsequent adsorption energies of −1.33 and −0.82 eV. The adsorption of O_2 is stronger than that of CO by 0.42 eV, implying that, statistically, O_2 should adsorb first. After one O_2 adsorbs on Fe/Ti_2CO_2, the adsorption energies of CO and O_2 become −0.57 and −0.23 eV, respectively, thermodynamically leading preferably to $CO+O_2$ co-adsorption. A second CO adsorption, i.e., $2CO+O_2$ co-adsorption, was predicted to be

possible as well, and to yield the energetically cheapest mechanism for CO_2 formation:

$$2CO^* + O_2^* \rightarrow CO_2^* + CO^* + O^* \rightarrow 2CO_2^* \quad (1)$$

The first and second CO_2 formations require energy barriers of only 0.20 eV and 0.15 eV, respectively. The CO_2 desorption energy, of 0.03 eV, is also very low. Peng et al. considered a SAC based on the same MXene but with a different surface functionalization, Ti_2CN_2, with a single atom of Zn[166]. Here, the calculated CO and O_2 adsorption energies were −0.89 and −0.88 eV, respectively. The CO oxidation mechanism predicted to be the easiest to realize is shown in Eq. 1, and consisted of gaseous CO interacting directly with the adsorbed O_2, forming gaseous CO_2 and leaving behind an O adatom, which then bonds with a second CO to form a second CO_2. The two reactions of this mechanism have very low energy barriers, of 0.06 and 0.03 eV, respectively, and are exothermic by over −2 eV. The desorption energies of the first and second formed CO_2 are 0.23 and 0.44 eV, respectively, indicating that the formed CO_2 molecules could be desorbed at room temperature. Given the popularity and vast knowledge about the Ti_2C MXene and the non-nobility of Fe and Zn, these results unveil the Fe/Ti_2CO_2 and Zn/Ti_2CN_2 single-atom catalysts as promising cheap and very active catalysts for CO oxidation.

Fischer-Tropsch synthesis

Kountoupi et al.[167] studied by experimental and computational approaches the suitability of the Mo_2CT_x MXene of the Fischer–Tropsch (FT) process[168–170] under steady-state conditions ($p = 25$ bar and $T = 600$ K), focusing on how the activity and selectivity are affected by the surface oxygen and carbidic carbon contents. From the experimental side, they concluded that the defunctionalization of the MXene using H_2 treatment at 400 °C yields a Mo_2C MXene-based catalyst with 55% selectivity towards higher hydrocarbons (alkanes with five or more carbon atoms). Furthermore, when the H_2 pre-treatment is made at 500 °C, carbon vacancies are created and the resulting catalyst can only form methane, not larger hydrocarbons. According to their DFT calculations, direct CO dissociation into C* and O* is easy avoiding the formation of other oxygenate species beyond CO_2 which becomes the major reaction product. The hydrogenation of CH_3* species to methane was predicted to involve a very high energy barrier thus leading to the formation of larger alkanes. Both the experimental and computational results led to the conclusion that the surface will become poisoned by O-adatoms due to CO decomposition reaction, with or without H_2 assistance, and the high-oxophilicity of the MXene.

Photocatalysis

In photocatalysis, electromagnetic radiation is used to promote electrons from the valence band to the conduction band, allowing their reaction with oxidants to create reduced products, and generate holes in the valence band, which can react with reductants to create oxidized products. In general, for this to successfully happen, two things are needed: the radiation energy must be greater than or equal to the band gap of the catalyst, and the lifetime of the electron–hole pair (called an exciton) must be long enough to keep the pair from recombining. Typically, infrared radiation (photons with energies between 1.24 meV and 1.7 eV) is used for this process because its energy range coincides with the range of energies separating the quantum levels of molecular vibrations and it contains the band gaps of many semiconductors. Infrared also represents more than half of the energy received from sunlight at the surface of the Earth. Studies on photocatalysis using MXenes are relatively scarce, probably because most MXenes are either metallic or have band gaps that are too wide[54,171]. According to DFT calculations using the very accurate HSE06 exchange-correlation functional[172], and machine-learning predictions[54], the MXenes most likely to have suitable band gaps for photocatalysis are made of M = Sc, Ti, or Y. We highlight Sc_2C, whose Janus-type surface termination was extensively studied in a PBE study by Zhang et al. in search for a photocatalysis-capable Sc_2C-based MXene[173]. Ten surface termination combinations were chosen from T, T' = O, F, H, OH, or Cl, forming Sc_2CTT' Janus surfaces. Of these, Sc_2CFCl, Sc_2COHCl, and Sc_2CHCl were deemed the most promising for photocatalysis because of their calculated band gaps, 1.79, 0.99, and 1.84, respectively, and large internal electric field. The Sc_2COHCl MXene should be suitable for photocatalysis using infrared radiation.

Ontiveros et al. explored MXenes as photocatalysts for driving the water splitting reaction[57]. Using the PBE functional for optimization runs and the PBE0 hybrid functional for more reliable band gap estimations, they analyzed the band alignment of M_2X and M_2XO_2 MXenes, where M = Sc, Y, Ti, Zr, Hf, V, Nb, Ta, Cr, Mo, or W, and X = C or N, with respect to water splitting potentials. Bare MXenes (i.e., without O-termination) were found to be metallic, whereas oxygen termination induced semiconducting behavior, with group III and IV MXenes emerging as the most promising candidates. Carbide MXenes (X = C) exhibited larger and more frequent band gaps when compared to nitride MXenes (X = N). Notably, for carbide MXenes, the band gap decreased for group III metals and increased for group IV metals when moving down the group, whereas an inverse trend was observed for nitride MXenes. Ontiveros et al.[57] also identified MXenes with band gaps exceeding 1.23 eV, the minimum photon energy thermodynamically required to drive water splitting, as determined by the oxidation potential of H_2O to O_2 (1.23 V vs. NHE). Among the O-terminated MXenes, Zr_2CO_2 emerged as a standout candidate due to its favorable band alignment with water-splitting potentials and significant charge density separation between the valence and conduction bands. Interestingly, the effect of stacking on the calculated band gaps was found to be subtle but sufficient to influence the electronic properties under certain conditions.

Electrocatalysis

Climate change and the increasing global energy demands are among the main problems that humanity faces today. The main electrochemical processes involved in the field of renewable energies are hydrogen evolution (HER), oxygen evolution (OER), oxygen reduction (ORR), and carbon dioxide reduction (CO_2RR)[174]. These processes occur at the solid/liquid interface between an electrode and an electrolyte solution. From the theoretical point of view, the mechanism via which an electrochemical processes occurs over an electrocatalyst can be described by a sequence of reaction intermediates and the Gibbs free energies changes between them (ΔG)[175]. This information can be condensed in a free energy diagram, which shows how the free energy changes along the reaction coordinate[176].

Regardless of the preferred mechanism of an electrochemical reaction over an electrocatalyst, the overall ΔG at zero electrode potential is the same. For example, OER is a four-electron-transfer process,

$$2H_2O \rightarrow O_2 + 4H^+ + 4e^- \quad (2)$$

Assuming an equilibrium potential of zero for the reversible hydrogen electrode, the equilibrium potential, U^0, of OER reaction is 1.23 V. Since the whole process involves transferring four electrons, this means that, if one sums the Gibbs free energy changes along the reaction path of OER over any electrocatalyst, the value thus found is always $4 \times 1.23 = 4.92$eV. In other words, in the free energy diagram of OER at zero applied potential, the final state lies 4.92 eV above the initial state. The application of an electrode potential can increase or decrease (depending on its polarity) the free energy of the intermediate and final states with respect to the initial state, potentially driving the reaction in the desired direction. Taking again the example of OER, an electrode potential of $U^0 = 1.23$ V brings the reaction to an equilibrium, by definition bringing the free energy of the products, from 4.92 eV above the reactants, to 0 eV, $G(\text{reactants}) = G(\text{products})$. In this situation, the system is at electrochemical equilibrium, and the net current is zero. If one applies an electrode potential, U, that is greater than the one needed to achieve equilibrium, then the forward direction will be favored, and O_2 will be produced. The difference, $\eta = U - U^0$, is the definition of the overpotential. Note that the electrode potential can stabilize not only the reaction products but also all the intermediates whose formation involves at least one electron or proton transfer. Obviously, one can almost always apply a very

large overpotential and force all electrochemical steps to become exergonic, but this is energetically unprofitable. Realistically, the applied overpotential should not exceed 0.3 V.

The activity of an electrocatalyst towards a certain electrochemical reaction can be assessed from the knowledge of the sequence of ΔG connecting the reactants and products, and by using the Sabatier principle and assuming a Brønsted–Evans–Polanyi relationship[177]. These two results state that the initial, intermediate and final species should not adsorb too weakly or too strongly on the electrocatalyst, and that the energy barrier values depend linearly upon the reaction energies. The descriptor $G_{max}(\eta)$, defined as the largest free-energy span between all reaction intermediates, was introduced by Exner to assess the performance of electrocatalysts[178]. This descriptor accounts for the applied overpotential and kinetic effects, and includes the concept that in catalysis, there are no rate-determining steps, but instead rate-determining states, as concluded by Kozuch and Shaik[179].

Hydrogen evolution

Hydrogen evolution is a reaction that produces H_2 from two protons. Although it is suitable for producing gaseous H_2, it is very commonly a nuisance competing side reaction in processes like nitrogen fixation or CO_2 reduction and, for this reason, knowledge on how likely it is to occur on an electrocatalyst is always useful. In general, two possible mechanisms are considered. The first reaction step is common to both and is called the Volmer step, in which a proton is reduced on the electrocatalytic surface,

$$H^+ + e^- + * \rightarrow H^* \quad (3)$$

In the Volmer-Tafel (VT) mechanism, the second (Tafel) step assumes that two Volmer steps have occurred, so that two H^* exist on the surface, which can then undergo a chemical step, generating molecular H_2,

$$2H^* \rightarrow H_2 + 2* \quad (4)$$

In the Volmer-Heyrovsky (VH) mechanism, the second proton is reduced directly on top of the first one, directly forming H_2,

$$H^+ + H^* + e^- \rightarrow H_2 + * \quad (5)$$

The activity of the $Ti_3C_2T_x$ MXene as a catalyst for the HER was studied by Meng et al., considering a large number of surface termination possibilities[180]. Surface termination phase diagrams were built, depicting the most stable surface functionalization for each (U, pH) pair, the so-called Pourbaix diagrams. The equilibrium potential of the HER is, by the usual definition, 0 V. At the equilibrium potential, and assuming the whole surface is functionalized by the same species, the most stable surface termination was found to be -O. In more realistic models, allowing binary and ternary functionalization, competition was found between $T_x = O_{2/3}(OH)_{1/3}$, $F_{1/3}O_{1/3}(OH)_{1/3}$ and $F_{3/9}O_{4/9}(OH)_{2/9}$, with similar stability, with the F-containing terminations occurring only at low pH. Gibbs free energy diagrams were obtained for all the surface termination possibilities. The strong H affinity of the pristine Ti_3C_2 MXene was found to prevent the formation of H_2. Interestingly, the three most stable terminations under working conditions were found to be the most promising for HER performance, since they require almost negligible overpotentials (0.01 V) for all the electrochemical steps to become exergonic (Table 5). For the $O_{2/3}(OH)_{1/3}$ and $F_{3/9}O_{4/9}(OH)_{2/9}$ terminations, the preferred mechanism is the Volmer-Heyrovsky one, while on $Ti_3C_2F_{1/3}O_{1/3}(OH)_{1/3}$, the Volmer-Tafel one is favored. In comparison, the V_2C MXene was predicted to achieve maximum electrocatalytic activity for HER when with a full H surface termination[181]. These findings show that the most favored surface termination for HER is MXene-dependent and that these surfaces can compete with other electrocatalysts commonly used for the HER, such as Pt, MoS_2, or WS_2.

A combination of experimental and computational approaches was used to analyze the role of surfaces terminations (T_x) on the HER activity of five different carbide MXenes (*viz.* Ti_2C, Ti_3C_2, Mo_2C, Mo_2TiC_2, and $Mo_2Ti_2C_3$)[182]. Handoko et al. observed that the HER activities of $Ti_3C_2T_x$ samples produced by different fluorine-containing etchants were largely dependent on the fluorine functionalization of the basal plane, with the samples containing higher coverages exhibiting lower activities (larger overpotentials). Moreover, the large Tafel slopes suggested that H adsorption (Volmer step) could be rate limiting. DFT calculations with the BEEF-vdW functional were performed to understand this behavior from the changes in the free energy for H adsorption (ΔG_H) with varying amounts of fluoro groups on the basal plane, as the ideal HER catalyst must hold ΔG_H values close to zero. The models $Ti_3C_2O_2$, $Ti_3C_2O_{1.5}F_{0.5}$, Ti_3C_2OF, $Ti_3C_2O_{0.5}F_{1.5}$, and $Ti_3C_2F_2$ with F:Ti ratios corresponding to 0.00, 0.17, 0.33, 0.50 and 0.67 per unit cell, respectively, were used to mimic MXenes with increasing degrees of fluoro functionalization. The calculated ΔG_H values were found to increase monotonically from F:Ti ratio of 0.00 to 0.50, with a more significant increase being observed on going from F:Ti ratio of 0.50 to 0.67, because the H atom adsorbs preferably on top of the oxo terminations which are not present in the basal plane of $Ti_3C_2F_2$. These authors extended the calculations to carbide MXenes containing molybdenum (Mo_2CT_x, $Mo_2TiC_2T_x$, and $Mo_2Ti_2C_3T_x$) and observed that in the $Mo_2TiC_2T_x$ and $Mo_2Ti_2C_3T_x$ MXenes, the increase of the fluoro functionalization induces a significant increase of the ΔG_H from F:Mo ratio of 0 to 0.25 and that the ΔG_H stays constant for larger functionalizations. Interestingly, in the case of the $Mo_2TiC_2F_2$ and $Mo_2Ti_2C_3F_2$ MXenes, the adsorption of H was found to be unstable and led to the formation of HF, as it was found by Gouveia and Gomes[82] when exploring the feasibility of the water gas shift reaction on the Mo_2CF_2 MXene. In the case of the Mo_2CT_x MXene without F functionalization, the BEEF-vdW ΔG_H value is 0.048 eV, which is closer to thermoneutrality than the ΔG_H calculated for the 2H-phase of MoS_2 (cf. 0.08 eV with the RPBE functional[183]), hence suggesting that the Mo_2CT_x without fluoro groups on the basal plane may be an excellent HER catalyst.The HER was also analyzed over 24 ordered double transition-metal carbide MXenes by Jin et al.[184]. As in the work of Handoko et al.[182], the BEEF-vdW ΔG_H values were used to identify the promising HER catalysts. Under the standard conditions, the most favorable surface terminations found were either the pure O functionalization, or a mix of O and OH groups, depending on the elemental composition of the outermost metallic layers. In particular, if these layers are made up of Mo, Ti or Nb, the surface tends to prefer the simple O termination, whereas when the outer layer contains Cr or V, the mixed O/OH termination is preferred. This mixed surface termination has also been predicted by López et al. for monometallic MXenes[185]. The activity and chemistry of the bimetallic MXenes was found to be dominated by the composition of the outer metal layer, and strongly dependent on the

Table 5 | Calculated data for the hydrogen evolution reaction on the $Ti_3C_2T_x$ MXene surface with different surface terminations

Termination	Mechanism	G_{max}/eV	η/V
None	–	2.41	–
O	VH	0.40	0.40
H	VH	0.63	0.63
OH	VH	0.48	0.48
F	VH	2.62	2.62
$O_{1/3}(OH)_{2/3}$	VH	0.08	0.08
$O_{1/2}(OH)_{1/2}$	VH	0.23	0.23
$O_{2/3}(OH)_{1/3}$	VH	0.01	0.01
$F_{1/3}O_{1/3}(OH)_{1/3}$	VT	0.08	0.01
$F_{3/9}O_{4/9}(OH)_{2/9}$	VH	0.01	0.01

For each surface composition, the preferred mechanism, Volmer-Heyrovsky (VH) or Volmer-Tafel (VT) is stated, along with G_{max} as a descriptor, and the overpotential, η, required to make all electrochemical steps exergonic. Data taken from ref. 180.

strength of the outer M-O bond: the weaker this bond in the MXene, the stronger the bond between the MXene O and the adsorbed H atom. The ordered double transition-metal MXene that showed the lowest overpotential (0.003 V) was $Mo_2NbC_2O_2$.

MXenes have also been mixed with other materials in order to improve their durability for the HER. For example, Lim and collaborators synthesized a 2H-MoS_2/Mo_2CT_x MXene nanohybrid[186]. Both their experiments and DFT calculations revealed that the sulfidation of the MXene, with an S/O ratio of 1/3, effectively prevents its oxidation and consequent deactivation, allowing the system to sustain current densities over 450 mA/cm^2. This not only experimentally demonstrates the capability of this particular nanohybrid, but also suggests that the interfaces between other materials and chalcogenides can be suitable for electrochemical applications.

Nitrogen and nitrate reduction

The electrochemical nitrogen reduction reaction (NRR) to ammonia,

$$N_2(g) + 6(H^+ + e^-) \rightarrow 2NH_3(g) \quad (6)$$

with an equilibrium potential of 0.057 eV, is a considerably more complex process than hydrogen evolution, involving more steps and more possible reaction mechanisms. For this reason, only bare MXenes had been studied theoretically for this application[154,187–189], until Johnson et al. investigated the role of the surface termination in controlling the NRR electrocatalytic activity of MXenes[190]. It was shown that the surface termination is especially important for this reaction because the calculated Pourbaix diagrams indicated that, under the NRR operating conditions, the O and H terminations are most favorable, with free energies of several eV below the bare materials. The associative NRR mechanism comprises six electron exchanges,

$$N_2(g) + H^+ + e^- \rightarrow *N_2H \quad (7)$$

$$*N_2H + H^+ + e^- \rightarrow *N_2H_2 \quad (8)$$

$$*N_2H_2 + H^+ + e^- \rightarrow *N + NH_3(g) \quad (9)$$

$$*N + H^+ + e^- \rightarrow *NH \quad (10)$$

$$*NH + H^+ + e^- \rightarrow *NH_2 \quad (11)$$

$$*NH_2 + H^+ + e^- \rightarrow NH_3(g) \quad (12)$$

In other words, one N atom of the N_2 molecule is three-fold hydrogenated and released as NH_3, and then the second atom undergoes the same process. Due to the well-known high reactivity of bare MXenes towards nitrogen adsorption[126] and the near-zero equilibrium potential, the free energy profiles of NRR on these surfaces are significantly downhill in the first parts of the reaction and equally uphill in later steps, implying catalyst poisoning by the early NRR intermediates. All bare MXenes were predicted to spontaneously form N_2H, and four of them (Mo_2C, Mo_2N, W_2C, and W_2N) offered a reasonable theoretical overpotential for NRR, which is not enough to make them suitable for nitrogen fixation, as bare MXenes are not stable under NRR conditions. In contrast, H- and O-terminated MXene surfaces are more stable but not as reactive. Of the 65 MXenes compared by Johnson et al.[190], only W_2CH_2 satisfies the three required criteria: i) low theoretical overpotential; ii) stability under NRR conditions; and iii) selectivity towards NRR instead of the unwanted HER.

Since the theoretical prediction of the stability of ordered bimetallic MXenes[191] and of the optimal conditions for their synthesis[192], many works have dedicated themselves to comparing the behavior of these materials with that of the traditional monometallic MXenes. This is the case of a study by Zhao et al., in which the activity of 18 double-metal MXenes, with stoichiometries $M'_2M''C_2$ and $M'_2M''_2C_3$, for electrochemical NRR was analyzed[193]. One important result was that the calculated ΔG of the potential-determining step are all below 0.98 eV, which is the benchmark value on the Ru(0001) surface. For most MXenes, this step was the second hydrogenation of the second N atom, Eq. 11. This includes $Mo_2Nb_2C_3$, the MXene that was estimated to be the most promising one for several reasons. Firstly, the calculated ΔG potential-determining step was the lowest one (0.39 eV), with an overpotential of 0.48 V. Secondly, by performing calculations including implicit solvation, the authors found that the solvent has a positive effect on NRR activity. Lastly, the O-functionalized $Mo_2Nb_2C_3O_2$ MXene surface with an O vacancy, a more realistic model compared to the experimentally prepared material, displayed the same activity as the bare one. The calculations revealed that the Mo atoms that directly bind to the reaction intermediates regulate the electron transfers between these species and are probably responsible for the high activity.

Very recently, the nitrate reduction reaction (NO_3RR) catalyzed by MXenes has been suggested as a very promising approach for converting nitrate into e.g., ammonia[194,195], which begins with the reduction of nitrate to N adatoms and then followed by reactions described by Eqs. 10–12. On transition metal (TM) clusters with 1 to 3 atoms deposited on O-vacancies of $M_3C_2O_2$ MXenes (TM = V, Cr, Mn, Fe, Co, Ni, Cu, Zr, and Hf; M = Ti, V, Cr, Nb and Mo), Zhao et al.[194] performed DFT calculations and found that the deposition of the TM clusters regulates the adsorption strength of the species involved in the NO_3RR. The $Nb_2@V_3C_2O_2$ and $Nb_3@V_3C_2O_2$ showed remarkable thermodynamic stability and the best catalytic activity and selectivity towards ammonia.

Gao et al.[195] studied the NO_3RR catalyzed by single atoms of a transition metal element from Ti to Au replacing a metal of the $Ti_3C_2O_2$ with a Ti-O vacancy. The most promising systems were predicted to be the ones containing an Ag (representative precious metal) or a Cu (representative of a non-precious metal) atom. High efficiency and selectivity towards ammonia and low limiting potentials were calculated for these two cases.

Oxygen evolution and reduction

OER and its reverse, ORR are two textbook reactions that are commonly tackled in theoretical studies of electrocatalysis. While bare MXenes are extremely oxophilic and can spontaneously dissociate oxygen molecules upon adsorption, the opposite happens on functionalized MXenes, and this can deter the application of any MXene, with or without surface termination, as an electrocatalyst for oxygen evolution or reduction. Table 6 compares the adsorption energy and charge transfers of oxygen molecules on some bare and surface-terminated MXenes.

Both bare and terminated MXenes are unsuited for OER/ORR, for opposite reasons. The former interact too strongly with reaction intermediates, keeping the products from desorbing, whereas the latter interact too weakly to effectively bind the species and provide electrons for the reaction to occur. One could argue that $Nb_2C(OH)_2$ is an exception to this, given the moderate O_2 adsorption energy of −0.92 eV. However, this adsorption was observed to be accompanied by the spontaneous extraction of two H atoms from surface OH groups to generate an H_2O_2 molecule, demonstrating the instability the OH-functionalized MXene, as had been predicted by Gouveia et al.[80] and Gao et al.[196].

Kan et al. showed that, by doping the surface of the Nb_2CT_2 MXene with single atoms of Pt or Pd, the MXene-O_2 interaction becomes more manageable and both OER and ORR can be conducted using the same surface as a bifunctional electrocatalyst[197]. This is illustrated in Table 7. The inclusion of single Pd or Pt atoms leads to O_2 adsorption energies and charge transfers that are between those of the bare and fully terminated Nb_2C MXene. Furthermore, if the single atoms are adsorbed on T vacancies, effectively partially replacing the T atoms, the O_2 adsorption energy nearly doubles and the OER and ORR overpotentials are nearly halved, ultimately causing the Pt SACs to display the lowest overpotentials for both reactions, especially when located at O or F vacancies of Nb_2CO_2 or Nb_2CF_2, respectively.

SACs have also been built by replacing an atom of the M element of a MXene with an atom of another transition metal element[198,199]. For example,

Table 6 | Adsorption energies (E_{ads} in eV) and charge transfers (Q in e) of O_2 on some bare ($x = 0$) and functionalized ($x = 2$) MXenes, according to the calculations in ref. 197

MXene	E_{ads} ($x = 0$)	E_{ads} ($x = 2$)	Q ($x = 0$)	Q ($x = 2$)
Nb_2CO_x	−11.47	−0.29	1.23	0.17
Nb_2CF_x	−11.47	−0.22	1.23	0.21
$Nb_2C(OH)_x$	−11.47	−0.92	1.23	0.88
Mo_2CO_x	−9.92	−0.36	0.82	0.13
Ti_2CO_x	−11.31	−0.19	0.91	0.12
V_2CO_x	−10.52	−0.23	1.08	0.15
$Ti_3C_2O_x$	−11.69	−0.27	0.98	0.11
$Nb_4C_3O_x$	−10.76	−0.12	0.88	0.07

Table 7 | Adsorption energies (E_{ads}) and charge transfers (Q) of O_2 on Pt-or Pd-doped Nb_2CT_2 MXene surfaces, and respective OER and ORR overpotentials, η_{OER} and η_{ORR}, respectively

Surface	E_{ads}/eV	Q/e	η_{OER}/V	η_{ORR}/V
Nb_2C	−11.47	1.23	---	---
Nb_2CO_2	−0.29	0.17	---	---
Nb_2CO_2-Pd	−0.35	0.47	0.56	0.80
Nb_2CO_2-Pt	−0.37	0.43	1.01	0.75
Nb_2CO_2-V_O-Pd	−0.62	0.61	0.44	0.51
Nb_2CO_2-V_O-Pt	−0.65	0.56	0.39	0.48
Nb_2CF_2-Pd	−0.32	0.41	0.45	0.78
Nb_2CF_2-Pt	−0.31	0.40	0.97	0.71
Nb_2CF_2-V_F-Pd	−0.59	0.57	0.58	0.47
Nb_2CF_2-V_F-Pt	−0.55	0.53	0.37	0.40

The surface termination is T = O or F, and the Pt or Pd atoms can be adsorbed surfaces without or with T vacancies (V_T). Data taken from ref. 197.

Chen et al. did a systematic DFT study of the effect of substitutional transition metal atoms on Mo_2CO_2 in the activity of this MXene towards the ORR[200]. Even though Mo_2CO_2 does not adsorb O_2, replacing one Mo with another transition metal can lead to O_2 adsorption energies up to −1.31 eV (for substitutional V). Substitutional Mn, Fe, or Ni atoms were projected to be the best for ORR, with overpotentials between 0.27 and 0.35 V and moderate O_2 adsorption energies between −0.32 and −0.50 eV, as required by the Sabatier principle. The employment of SACs here has several advantages, such as providing a middle-ground between the reactivity of bare and terminated MXenes, and allowing more efficient use of noble metal atoms—100 % on Nb_2CO_2-V_O-Pt and Nb_2CF_2-V_F-Pt *vs.* 33.3% on Pt(111) or IrO_2(110), the benchmark ORR catalysts.

Carbon dioxide reduction

Carbon dioxide can be electrochemically reduced through many mechanisms and into different products. Motivated partly by the fact that the bare Nb_2N MXene surface had been predicted to bind to transition metal atoms[201], CO_2 electroreduction process was studied by Lu et al. over SACs (V, Cr, Mn, Fe, Co, or Ni) on the Nb_2NO_2 MXene surface, using the PBE-D3 approach[202]. They found that CO_2 adsorbs preferably on the transition metal atom with moderate adsorption energies, ranging between −0.77 and −0.30 eV, which are suitable for catalysis, and with moderate charge transfers, ranging from 0.60 to 0.25 electrons, as shown in Table 8. Furthermore, the analysis was simplified by the fact that intermediate species with more than one carbon atom are not stable over SACs, so that only mono-carbon species had to be considered. Notably, the Co and Ni SACs

Table 8 | Adsorption energies (E_{ads}) of CO_2 and CH_4, charge transfers (Q) upon CO_2 adsorption, and maximum Gibbs free energy spans (G_{max}) of CO_2 reduction to CH_4 on the Nb_2NO_2 MXene surface doped with one atom of V, Cr, Mn, Fe, Co or Ni, according to the results of the calculations taken from ref. 202

Surface	$E_{ads}(CO_2)$/eV	Q/e	G_{max}/eV	$E_{ads}(CH_4)$/eV
Nb_2NO_2-V	−0.77	−0.60	1.00	−0.35
Nb_2NO_2-Cr	−0.51	−0.53	0.90	−0.47
Nb_2NO_2-Mn	−0.34	−0.58	0.95	−0.23
Nb_2NO_2-Fe	−0.46	−0.25	1.15	−0.41
Nb_2NO_2-Co	−0.30	−0.26	0.60	−0.38
Nb_2NO_2-Ni	−0.54	−0.31	0.80	−0.36

exhibit G_{max} lower than and similar to, respectively, the limiting potential of 0.74 V of the state-of-the-art Cu(211) catalyst[203].

These results can be compared with analogous ones obtained for the CO_2 electrochemical reduction on SACs over the Ti_2CO_2 MXene surface[204]. Zheng et al. found that the catalytic activity of such SACs can be described by the valence state of the transition metal adatom and observed a volcano-shaped relationship between these two quantities, peaked around 0.8 electrons for Co and Ni. The same transition metal elements were indeed estimated to yield the best catalytic activity on Nb_2NO_2 as well, albeit with a different peak charge transferred of *circa* 0.5 electrons[202]. This reaction has also been studied on 10 SACs deposited on the Ti_2CN_2 MXene surface[205]. There, Sc-, Ti-, V-, Mn- and Fe-based SACs were predicted to effectively originate CO with overpotentials below 0.5 V, but with poor CO selectivity on the first three transition metals. However, N-functionalized MXenes may be too reactive towards transition metal atom adsorption[98].

The effect of the surface termination in the CO2RR was analyzed very recently by Meng et al.[206]. These authors considered the Ti_3C_2 MXene with several combinations of the O, OH and F surface terminations, *viz.* OH, $(OH)_{2/3}O_{1/3}$, $(OH)_{1/2}O_{1/2}$, $(OH)_{1/3}O_{2/3}$ and $F_{1/3}(OH)_{1/3}O_{1/3}$, which differs from previous studies that focused on uniformly functionalized MXenes. The OH groups were found to serve mainly as H-donors, and the presence of both OH and O groups benefited the catalysis by reducing the limiting potential, in agreement with experimental results available in the literature.

Hydrazine oxidation

The electrochemical hydrazine oxidation follows the global reaction

$$N_2H_4 \rightarrow N_2 + 4H^+ + 4e^- \quad (13)$$

with standard potential -0.33 V. Zhou et al. reported a joint experimental and theoretical study of the activity of a Ni SAC based on the $Ti_3C_2T_x$ MXene towards this reaction[207].

Experimentally, it was observed that Ni atoms occupy Ti vacancies on the surface of the MXene and that the activity of the Ni SAC surpasses that of Ni nanoparticles, both deposited on the same $Ti_3C_2T_x$ MXene.

The DFT-based calculations, using the PBE exchange-correlation functional, determined that an Ni atom deposited on a Ti vacancy of the $Ti_3C_2T_x$ MXene becomes strongly coupled to the neighboring C atoms. In turn, the presence of Ni at a Ti vacancy of the $Ti_3C_2T_x$ MXene was found to cause a downshift in the *d*-band center of the C atoms from 1.74 eV to 1.52 eV, allowing for an optimal activation energy of N_2H_4. This molecule was adsorbed preferably over the Ni single atom, with a moderate adsorption energy of -0.69 eV, which suggests a stronger adsorption than on Ni nanoparticles (E_{ads} = -0.55 eV). The overall activation energy for hydrazine oxidation was estimated at 0.45 eV, or 0.13 eV lower than on Ni nanoparticles deposited on the same MXene, supporting the experimental findings that a Ni single atom prevails over Ni nanoparticles for hydrazine oxidation.

Predictions by machine learning

The MXene family of materials includes a wide range of elemental compositions combined with different surface terminations, which currently leaves the majority of possible MXenes undiscovered or uncharacterized. Traditional experimental trial and error takes a long time to unveil the full potential of these materials. Therefore, DFT calculations have been employed to obtain descriptors and output properties associated with their production and application and, more recently, machine learning (ML) strategies are being developed to digest high-throughput DFT data, and thus accelerate the discovery of new and synthesizable MXenes for targeted applications (Fig. 9)[208]. As a result, an account of the current state of the art regarding machine learning studies that target the MXene family of materials is provided herein, with the main details of the ML approaches presented in Table 9.

Synthesizability and stability

A central issue for the application of MXenes is their synthesizability. To tackle this problem, Frey et al.[209] employed a positive and unlabeled (PU) machine learning framework, adapting it to predict the likelihood of successfully obtaining these materials. Besides the MXene family, they also built a model for their layered precursor materials known as MAX phases. Elemental information and data from high-throughput DFT calculations were utilized to characterize each material. After a feature selection step based on principal component analysis, the model hyperparameters were optimized. Two positive and unlabeled learning algorithms were employed, with the most helpful being an implementation of transductive bagging coupled with a decision tree classifier, chosen for its interpretability. The model generated synthesizability scores ranging from 0 to 1 for unlabeled samples, with the analysis revealing that features related to thermodynamic stability, bond strength, and charge distribution had the most significant impact on predictions. Notably, the predictions of the model aligned well with experimental findings, indicating that earlier group transition metal MXene and MAX phases with lower charge densities of the M atoms were more likely to be synthesized. The positive and unlabeled learning model successfully identified 111 MAX phases and 18 MXenes as synthesizable materials, including novel systems, such as Hf_4N_3, Sc_3C_2, and W_4C_3, even though monometallic MXenes based on Hf, Sc, or W had not been synthesized yet. Moreover, by considering both MAX phase synthesizability and the MXene score, the authors identified the top 20 most promising MAX systems that could be synthesized and subsequently etched to produce previously unavailable MXenes. Their results were validated based on 10-fold cross-validation, and, in time, these predictions of promising systems allow for a litmus test on their work.

He and Zhang[210] explored the stability of $M_{n+1}X_n$ MXenes, testing several machine learning algorithms and symbolic regression methods to assess and classify MXene material stability, based on a relatively small dataset of 85 materials. The output stability value was defined as the convex hull distance, according to the formula $E_{stability} = E_{formation} - H_f$, where $E_{formation}$ is the formation energy and H_f is the convex hull energy, following the definition from other authors[211]. After using Pearson regression to select the most appropriate descriptors, random forest, k-nearest neighbors, logistic regression, support vector machine, and gaussian naive bayes were tested, with support vector machine emerging as the most accurate method for classifying materials based on their stability. Beyond the supervised learning classification approach, one interesting aspect of the study was the use of symbolic regression. Symbolic regression aims to find a symbolic expression or mathematical equation that best fits the data, essentially modeling the relationship between the input features and the outcomes. This symbolic expression can then be used to predict new data points or for further analysis. Using this methodology, the authors identified the key descriptors and generated an indicator (from the combination of other descriptors) that can be associated with MXene material stability. In this study, $(\chi(M)\text{-}R_{vdW}(M))^3$ was the new and most important descriptor, obtained from symbolic regression, where $R_{vdW}(M)$ is the atomic van der Waals radius of the metal, and $\chi(M)$ corresponds to its electronegativity. Note that the greater variability on the considered $M_{n+1}X_n$ MXenes is associated with the nature of the M element; hence, it is not surprising that the key indicators prioritize data for the M element over the X element.

Electronic properties

Rajan et al.[54] delved into the electronic properties of MXenes, especially their band gaps, which are important to identify promising candidates for electronic, optoelectronic, and photocatalytic applications. The authors employed kernel ridge regression, support vector machine, Gaussian process, and bootstrap aggregating, using as input variables readily available elemental properties and DFT-optimized structural and electronic properties. From 23 870 generated structures, 7200 were randomly selected to obtain all the DFT and elemental properties necessary to build an initial metal−semiconductor classification model, which filters out finite gap MXenes with 94 % accuracy using the bootstrap aggregation algorithm. From these, 70 were selected as semiconductors, and their band gaps predicted using a ML regression model with the Gaussian process algorithm, which yielded the best results. The authors were able to address the band gap underestimation issue commonly found when using local and semi-local functionals in DFT calculations, without resorting to more time-intensive approaches, such as GW, despite still requiring the calculation of DFT based structural and electronic descriptors.

Besides the many possible MXene compositions and their different terminations, the functionalization of MXenes can result in tens of thousands of possible materials, with potential applications spanning from electronics to energy-related fields. For these types of applications, MXene properties depend on the position of their band edges. Therefore, their determination can allow the tailoring of their structure for specific applications. However, computing the position of these bands can be time-

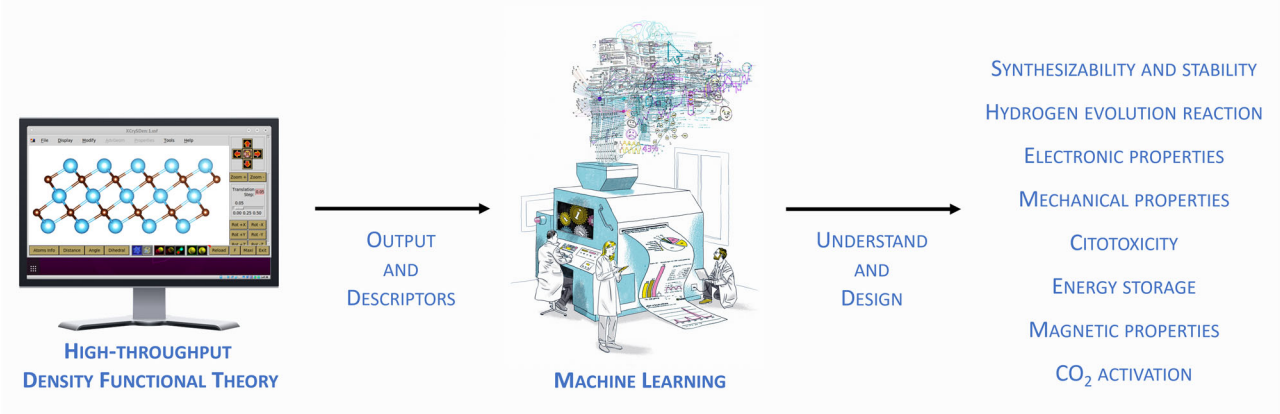

Fig. 9 | Computational modeling strategy. DFT and ML complementarity to understand and design applied MXenes.

Table 9 | Details of the machine learning (ML) approaches used to model and predict different MXene outputs[a]

Year, authors	Output	Data size	Feature selection	ML problem	Algorithm	Validation /Test
Rajan et al.[54]	Metal−semiconductor identification	643	LASSO	Classification	Bagging	5-fold CV, 10 % test
Rajan et al.[54]	Band-gap estimation	70	LASSO	Regression	Gaussian process	5-fold CV, 10 % test
Frey et al.[209]	Synthesizability	792	PCA	Positive and unlabeled learning	Robust ensemble SVM	10-fold CV
Mishra et al.[212]	Valence band	76	LASSO, NCA	Regression	Gaussian process	10 % test
Marchwiany et al.[219]	Cytotoxicity	71	Random forest feature importance	Classification	Random forest	10-fold CV
Venturi et al.[214]	Mechanical strength, band gap and formation energy	>3500	---	Regression	CGCNNs	15 % validation; 15 % test
Wang et al.[222]	HER	420	RFE; feature importance; Pearson correlation coefficient	Regression	AdaBoost	10-fold CV
Zheng et al.[221]	HER	299	Pearson correlation coefficient	Regression	Random forest	10-fold CV, 25 % test
He et al.[210]	Stability	85	Pearson correlation coefficient; Symbolic regression	Classification	SVM	20 % test
Li et al.[226]	Energy storage (gravimetric capacity, voltage, and induced charge)	360	RFE	Regression and Classification	Multi-output random forest	5-fold CV; 20 % test
Song et al.[218]	Saturation magnetization	23825	---	Classification	AdaBoost	10-fold CV; 10 % test
Tian et al.[216]	Tensile stiffness	157	---	Regression	SISSO	---
Abraham et al.[229]	CO_2 activation	114	Feature importance	Regression	Random forest	5-fold CV; 20 % test
Boonpalit et al.[230]	CO sensing	450	---	Regression	CGCNNs	20 % validation
Chen et al.[224]	ORR and OER	78	Feature importance	Regression	Random forest	4-fold CV; 25 % test
Cheng et al.[227]	Hydrogen adsorption distance	12647	---	Classification and regression	ALIGNNs	5-fold CV
Ding et al.[232]	Solar spectral absorption	500	---	Regression	Random forest	10 % test
Jiao et al.[231]	C−N coupling	54	LASSO	Regression	SISSO	10-fold CV
Ma et al.[225]	ORR and OER	42	Expert knowledge criteria	Regression	Random forest and gradient boosting	5-fold CV; 10 % test
Liang et al.[223]	HER (Gibbs free energy of hydrogen adsorption)	264	Pearson correlation coefficient; feature importance	Regression	Random forests	30 % test
Liang et al.[223]	HER (cohesive energy)	264	Pearson correlation coefficient; feature importance	Regression	Random forest	30 % test
Roy et al.[213]	Work function	275 and 315	Genetic algorithm	Regression	Artificial neural networks	5-fold CV; 20 % test

[a]Definition of the abbreviations: ALIGNNs - physics-informed atomistic line graph neural networks; CGCNNs - Crystal Graph Convolutional Neural Networks; CV - Cross-Validation; HER – Hydrogen Evolution Reaction; LASSO - Least Absolute Shrinkage and Selection Operator; NCA - Neighborhood Component Analysis; OER – Oxygen Evolution Reaction; ORR – Oxygen Reduction Reaction; PCA - Principle Component Analysis; RFE - Recursive Feature Elimination; SISSO - Sure Independence Screening and Sparsifying Operator; SVM – Support Vector Machine.

intensive, especially taking into account all the possible configurations that could be considered. To address this challenge, Mishra et al.[212] developed a machine-learning model capable of determining the position of the valence or conduction band edges, using gaussian process regression, with a level of accuracy akin to GW calculations, achieving a minimal root-mean-squared error of 0.12 eV. Their model is based on PBE band edges and vacuum potential together with other DFT (formation energy, ground state phase) and elemental (standard deviations of atomic radius, average of molar volume for all the species, and heat of vaporization) descriptors, correlating with GW-derived band edges. Their work also pointed to the role of the electronegativity difference between the functional groups and the transition metals in determining band edges and fine-tuning the electronic properties of MXenes. This factor was considered as a descriptor in the model and reveals the role of creating surface dipoles due to MXene functionalization on the band positioning and modification of vacuum potential.

An electronic surface property that can influence the application of MXenes in catalysis, electronics, and energy storage is the work function. Using a dataset of 275 MXenes encompassing various compositions and surface terminations, including O, OH, F, or none. Roy et al.[213] developed a series of ML models to identify MXenes with desirable work function values. Based on 15 fundamental descriptors for the elements and using artificial neural networks, the authors were able to estimate work function values with an associated mean absolute error value of 0.25 eV for the test set. Feature importance analysis revealed that the work function is mostly influenced by the properties of atoms terminating the MXene surface, namely their electronegativity, mutually validating the conclusions obtained years before by Mishra et al.[212]. In order to increase the transferability of their model to new materials, the authors developed reduced-order models with ten, eight, and five features, which were able to predict the work function of MXenes with various surface terminations beyond the original training set, such as Br, Cl, S, N, and NH (including extra data related to these new models in comparison with the initial dataset), with only a minor increase in mean absolute error.

Mechanical properties

Besides their unique electronic properties, MXenes are also known to be mechanically stronger than other 2D materials like graphene oxide (GO)[214,215], being applied as part of protective coatings, composites and membranes[215]. Venturi et al.[214] developed a ML approach to avoid the computation of descriptors of materials, which might require more expensive DFT calculations. Therefore, they used crystal graph convolutional neural networks on systems with planar periodicity (also containing systems besides MXenes), to calculate their thermodynamic, mechanical, and electronic properties. Their screening process considered nearly 45 000 material structures, focusing on two end uses: mechanical strength and photovoltaics. By analyzing statistical data derived from their screening, they unveiled the main structural and compositional design principles that influence the properties of the materials. Their approach reciprocally validated well-established design principles and revealed novel insights. For instance, they reaffirmed that hybrid organic-inorganic perovskites containing lead or tin are promising candidates for solar cell applications, in line with existing literature. Additionally, they identified titanium-based MXenes as having high stiffness coefficients, aligning with their reputation as mechanically robust materials. Moreover, their investigation uncovered promising untested compositions of all-inorganic perovskites, offering unexplored avenues for research in the field of photovoltaics. Lastly, they made the code available, which can foster further developments in the field. Their work has shown the capabilities of crystal graph convolutional neural networks, and the design principles presented by the authors can guide further experimental and computational research.

Tian et al.[216] conducted a machine learning-based study focused specifically on the mechanical properties of MXenes, in particular, on the tensile stiffness and strength of 157 types of MXenes, obtained from DFT calculations. Their results reveal a wide range of tensile stiffness values for MXenes, with 42 structures surpassing the stiffness of materials known for their outstanding mechanical properties, such as graphene and transition metal dichalcogenide monolayers. The mechanical properties of MXenes were found to be strongly influenced by their thickness, bond strength, and surface terminations. Remarkably, similarly to the electronic properties, the surface terminations were identified as a key factor in enhancing the tensile stiffness, which can be twice as high for some surface terminations in comparison with bare MXenes. The authors used a machine learning technique for high-dimensional data analysis and feature selection, named Sure Independence Screening and Sparsifying Operator (SISSO), that allows to obtain interpretable relationships between descriptors and outputs. As a result, based on physically interpretable descriptors, the following analytical formula for predicting tensile stiffness (E^{2D}) was obtained:

$$E^{2D} = E_{MX} + E_{coupling} + E_{T} \quad (14)$$

where the three quantities on the righthand side of the equation are also derived formulas themselves. E_{MX} represents the effect of thickness and bond stiffness and depends on the MXene thickness and M–X bond stiffness, $E_{coupling}$ represents the weakening effect of surface terminations on internal M–X bonds, therefore it is a function of both M–X and M–T bond stiffness, and E_T is the contribution of the stiffness of the M–T bonds. Furthermore, the authors found that the tensile strength (σ_s) scales linearly with the tensile stiffness.

Magnetic properties

Two-dimensional ferromagnetic materials have been playing an increasingly essential role in low-dimensional spintronics[217]. Since MXenes are emerging as one of the largest families of two-dimensional materials, Song et al.[218] developed an ML model to classify the magnetic states of these materials, starting with a database of 23,825 materials. Their approach combined high-throughput DFT calculations with machine learning techniques, and introduced a new descriptor, derived from the averaging of matrices with information about elemental properties, crystal structure (connectivity), and Coulomb interactions. After developing and evaluating their model on the larger dataset, the authors conducted DFT calculations with the PBE functional, generating structures and properties for 4153 new MXene materials, from which 753 materials were found to possess high saturation magnetization (a saturation magnetization criterion of 15 $\mu_B$nm^{-2} was employed to classify magnetic from non-magnetic materials). Then, they employed the previously developed ML classification model (AdaBoost, cf. Table 9) to purpose 1432 promising 2D magnetic MXene materials, that should possess high saturation magnetization. Note that the quality of the ML data is strongly determined by the choice of the DFT approach (please see section "Magnetic ordering" above). The PBE functional may struggle to accurately describe magnetic materials, especially those with strong electron-electron interactions, and hybrid functionals are typically regarded as more effective choices for accurately capturing magnetic properties.

Cytotoxicity

For the industrial application of MXenes, the toxicological profile of these materials must be evaluated. Traditional in vitro toxicological studies are time-consuming and expensive, therefore predictive models, such as those being developed with the aid of ML techniques, are often employed in some step of the development process and life cycle analysis of materials. Marchwiany et al.[219] identified key surface-specific features associated with the cytotoxic behavior of 2D materials and leveraged machine learning to predict the toxicity for MXenes not previously tested in vitro. They highlighted two factors contributing to the cytotoxicity of 2D materials, notably the presence of transition metal oxides and lithium atoms on the surface. Furthermore, their research underscores the importance of surface characteristics to the toxicity of MXenes, while other structural properties have minimal impact. The machine-learning model successfully assessed the cytotoxicity of 19 MXenes, identifying two as cytotoxic with almost 90% probability, while the rest are considered non-toxic (cytotoxicity probability

lower than 20 %) and suitable for various technological applications. The two MXenes that were predicted to be toxic are based on Ti_3C_2 and are the only ones with metal (titanium) oxide on their surface. Additionally, the research methodology and machine learning models developed by the authors can be extended to other complex 2D materials, including emerging materials like 2D transition metal borides (MBenes)[9] and van der Waals heterostructures[220].

Hydrogen evolution reaction

For the high-throughput screening of potential hydrogen evolution reaction (HER) MXene catalysts, Zheng et al.[221] employed a combination of ML models and DFT calculations, to predict the Gibbs free energy of hydrogen adsorption (ΔG_{H^*}), which, according to the authors, is an accepted proxy of HER performance for various catalysts. First, the authors employed four different ML regression algorithms, including Elman artificial neural networks, kernel ridge regression, support vector machine, and random forest, based on DFT calculations for a total of 132 MXenes. The random forest algorithm gave the best performance and, in comparison with other algorithms, also had the advantage of its performance being the same when using DFT-based descriptors (lattice parameter, bond lengths, Bader charges, etc.) together with elemental properties (tabulated properties for the M, X, and T atoms included in the MXene structure), or using solely elemental descriptors with no DFT descriptors. Therefore, the authors relied on the random forest model with elemental properties alone to make further predictions, since it was faster to evaluate new prospective MXenes catalysts. Their work considered bare and S-terminated MXenes and identified Os_2B and the S-terminated $Sc_{n+1}N_n$ ($n = 1, 2, 3$) MXenes as active catalysts, since ΔG_{H^*} approaches zero for a broad range of hydrogen coverages (from 1/9 to 4/9 monolayer). Furthermore, the authors highlighted the role of S functional groups in modulating HER performance, causing the weakening of the adsorption of H*, which is a pivotal step in the HER process. Furthermore, ΔG_{H^*} values were predicted using the developed random forest model considering only elemental properties for 167 new MXenes. This was in addition to the 132 tested initially that also included DFT descriptors, giving a total of 299 MXenes evaluated in this work, and resulting in the identification of 8 new MXenes as potential HER catalysts. This work included a thorough validation and testing methodology, based on tenfold cross-validation, leaving 25% of the dataset for testing, which was randomized 100 times, while also considering leave-one-cluster-out cross-validation, with clusters depending on the physical similarities of the materials.

Wang et al.[222] used high-throughput DFT calculations and ML to identify trends in the activity of oxygen-terminated monometallic and ordered bimetallic MXenes as HER catalysts. The materials considered by the authors were evaluated in terms of catalytic activity, thermal stability, and conductivity computations. Their work identified 110 experimentally unexplored MXenes with promising HER activity and thermal stability that surpasses that of the ideal platinum catalyst. Interestingly, titanium was featured in most of the predicted promising bimetallic MXene catalysts, which is supported by experimental results. Furthermore, their work demonstrated that the development of descriptors based on the AdaBoost ensemble learning model is able to accurately predict HER activity and unveil the fundamental geometric and chemical origins of the process, which are also consistent with electronic insights. The authors relied on tenfold cross-validation to optimize the model, and the materials predicted to surpass the ideal platinum catalyst, when they are obtained experimentally, can be used to further evaluate their predictions in the future.

Liang et al.[223] explored the effect on the MXene electrocatalytic performance of surface termination tuning and the incorporation of single transition metal (TM) atoms, using DFT) calculations as the primary tool. Their research identified 21 previously uninvestigated TM@MXene catalysts that exhibit superior electrocatalytic activity compared to platinum, among a pool of 264 promising candidates. Furthermore, 7 of these 21 promising HER catalysts were predicted to have both thermal and thermodynamic stability, underlining their potential for practical application. Interestingly, these 7 MXenes are all based on Ti_3C_2, with varying surface termination and TM doping. This is of interest for practical applications, since Ti_3C_2-based MXenes are the ones whose method of synthesis has been known for the longest time. Additionally, the authors verified that ML techniques were able to predict the catalyst activity (ΔG_{H^*}) and thermal stability (cohesive energy) using only easily accessible elemental properties of single atoms and surfaces group elements, such as molar volumes, atomic radius, boiling points, and electron affinities, for ΔG_{H^*}, and the third ionization, ionic radius, atomic mass, crystal radius, and molar volume for the cohesive energy.

Oxygen reduction and evolution reactions

The oxygen reduction reaction (ORR) and oxygen evolution reaction (OER) are critical for electrochemical conversion processes that play a role in various clean energy conversion and energy storage technologies, which are pivotal to unveil sustainable energy solutions. Despite their importance, ORR and OER suffer from slow kinetics and require catalysts such as platinum, ruthenium dioxide or iridium dioxide, to occur. However, the price of the metals in these catalysts prevents their widespread adoption for large-scale industrial applications. Therefore, Chen et al.[224] explored the catalytic potential of M-N_4-Gr/MXene heterojunction nanosheets for ORR and OER, through a combination of DFT calculations and ML predictions. The M-N_4-Gr layer is based on graphene (Gr), replacing two neighboring carbon atoms by one atom of a metallic (M) element and the four surrounding carbons with nitrogens (N_4). A total of 78 heterostructure nanosheets, comprising the Ti_2C, Nb_2C, and V_2C MXenes and M-N_4-Gr implanted with each of 26 different transition metal atoms, were examined. The random forest regression algorithm demonstrated the best performance among the tested ML methods, resulting in reduced root mean squared root errors. This study also highlighted the potential of Ni-N_4-Gr/Nb_2C and Ni-N_4-Gr/V_2C for ORR, Ru-N_4-Gr/Nb_2C for OER, whereas Co-N_4-Gr/V_2C was predicted to be a promising bifunctional catalyst. The authors also identified the *d*-band center of the metal active site and the amount of charge transfer from the metal in each structure as key descriptors, from the correlation between these descriptors and the overpotential, thus providing valuable insights for future catalyst design.

Ma et al.[225] studied the catalytic activity of Pt-doped dual transition metal Janus MXenes, which, in this case, are MXenes that have different types of transition metal elements on each side of the surface. The authors took advantage of this to design bifunctional catalysts for both ORR and OER. Through a combination of first-principles calculations and ML models, their study explores the underlying physical and chemical factors that influence the catalytic overpotential. The dynamic and thermal stability of Janus MXenes was initially evaluated using cohesive energies, phonon dispersion, and ab initio molecular dynamics simulations. Subsequently, the electronic properties of Pt-doped Janus MXenes were examined. The analysis confirmed the stable support of Pt atoms on the oxygen vacancies (Pt-V_O) of dual transition metal MXenes, while the density of states and projected density of states calculations indicated their favorable electrical conductivity as single-atom catalysts. Building upon these findings, high-performance single-atom catalysts with minimal overpotentials for ORR and OER were identified, such as Pt-V_O-$CrTiCO_2$, Pt-V_O-$MnTiCO_2$ and Pt-V_O-$PdTiCO_2$. Pt-V_O-$MnTiCO_2$, in particular, showed the most significant improvement compared to Pt-V_O-Ti_2CO_2, which was considered as a reference system in this study. This achievement was credited to the adjustment of single-atom catalysts electronic properties through dual transition metal modifications. A key aspect of this study was the consideration of machine-learning models (random forest regression and gradient boosted regression) to pinpoint descriptors crucial to the catalytic activity of MXenes-based single-atom catalysts for ORR/OER, concluding that the adsorption energy of OH was the most important descriptor for both ML models as well as for both reactions. Therefore, as future work, the authors propose to focus on the adsorption of OH on the catalyst surface, increasing the dataset and building a new ML model for this purpose. Moreover, the binding energy of Pt onto the substrate and the *d*-band center of the Pt atom were also found to be important descriptors to model both

reactions. Hence, this study provides valuable guidance for the development of novel and efficient bifunctional Janus-MXenes electrocatalysts for ORR and OER.

Energy storage

The mass adoption of electric cars and the critical role of wireless electronic devices in our lives are putting increasing pressure on lithium prices, since it is ubiquitous in batteries due to its excellent balance of energy density, power density, and life cycle. This has led to the development of new high-capacity battery materials that can reduce the dependence on lithium, and MXenes are also candidates for this application. Li and Barnard[226] explored the electrochemical energy storage potential of MXenes, in order to establish a relationship between MXene composition and various electrochemical properties. The authors transformed the MXene chemical formulas into categorical descriptors, enabling the simultaneous prediction of multiple electrochemical properties. The ML workflow developed incorporated multi-target regression techniques, to predict the gravimetric capacity, voltage, and induced charge, emphasizing the physicochemical characteristics crucial for battery design. Furthermore, this study involved an inverse design approach by predicting MXene formulas based on predefined battery performance criteria, using multi-target classification techniques. The MXene surfaces studied were of the form $Z_2M_2CT_2$, where the MXene transition metal element is M = Sc, Ti, V, Cr, Zr, Nb, Mo, Hf, or Ta; the surface termination is T = H, O, OH, F, or none; and an extra ion intercalation layer was considered, Z = Li, Na, K, or Mg. The resulting inverse model suggests Li_2M_2C and Mg_2M_2C (M = Sc, Ti, Cr) as promising candidates for more detailed analysis using DFT, according to the predicted gravimetric capacity, voltage, and induced charge properties. On the one hand, the more traditional forward predictions, based on a regression model, allow to establish guidelines for the discovery of new battery materials, identifying as important factors the intercalating ions, transition metals, and functional groups. On the other hand, the inverse model, based on classification, is a tool to predict new battery materials with targeted specifications, while considering three important variables for final application within the same model (multi-target ML). This study shows the capability of the inverse model to classify multi-class materials accurately, expanding the scope of inverse design and offering specific chemical formulas as potential outputs.

Hydrogen storage

Cheng et al.[227] performed a computational study exploring the hydrogen storage capabilities of MXene multilayers, motivated by growing interest in hydrogen as a clean energy source and the potential of MXenes multilayers for hydrogen storage, as highlighted by Liu et al. [228]. Cheng et al. developed a workflow to screen a large number of MXene compounds (23,857 in total, with 12,647 used to train and validate the model) to investigate the relationship between the activated H_2 bond length and the adsorption distance. The methodology involved the use of DFT to generate a dataset concerning the adsorption geometries of hydrogen on MXenes, which allowed to understand how hydrogen molecules interact with the MXene surface. Furthermore, the study employed machine-learning techniques, specifically physics-informed atomistic line graph neural networks (ALIGNNs), to predict adsorption parameters. ALIGNNs are a type of neural network designed to model physical systems by incorporating known laws of physics into their structure, which enhances their predictive accuracy and interpretability. They were interpreted within the framework of Pauling's resonating valence bond (RVB) theory, which describes the quantum mechanical phenomenon where electrons are not localized on individual atoms in a molecule or a crystal lattice but are spread over several atoms, forming a resonance structure. The main conclusion of the study was the derivation of a general formula that describes the relationship between the activated H_2 bond length and the adsorption distance on MXenes. This formula, based on DFT, machine learning, and RVB theory, indicates how the ligancy (i.e., coordination number) and valence of transition metals in MXenes affect the activation of dihydrogen, which is a crucial aspect of hydrogen storage.

CO_2 activation and CO sensing

In order to create added value by removing the excessive carbon dioxide concentration from the atmosphere of the Earth, CO_2 should be utilized at an industrial level instead of just stored. Abraham et al.[229] combined high-throughput DFT and ML methodologies to identify the main descriptors associated with the activation of CO_2 over MXene surfaces. They analyzed a dataset comprising 114 pure and defective MXenes, offering insights into their adsorption energy, with random forest regression emerging as the best-performing method. Based on feature importance analysis embedded in random forest, the authors found that surface properties such as *d*-band center, surface metal electronegativity, and the valence electron number of metallic atoms were the key indicators to predict CO_2 activation. This work established a framework for the design of MXene-based catalysts, facilitating the prediction of potential markers for CO_2 activation and its subsequent utilization.

Carbon monoxide detection is vital for environmental safety, since it is colorless and odorless, but poses a high health risk. Due to their surface accessibility, electrical conductivity, stability, and surface functionalization versatility, MXenes are ideal candidates for gas sensing applications. O- and S- terminated MXenes exhibit limited interaction with CO, but it can be significantly enhanced through transition metal decoration. Therefore, Boonpalit et al.[230] presented an innovative approach involving the high-throughput screening of 450 combinations of transition-metal decorated MXenes (TM@MXene) for CO sensing applications. This screening is facilitated by an integrated active learning and DFT pipeline developed by the authors. The active learning component harnesses a crystal graph convolutional neural network (CGCNN) as a surrogate model, enabling the swift identification of CO sensor candidates while minimizing computational resource demands. The CGCNN approach allows to increase the speed of virtual screening by skipping the iterative feature engineering step, due to its automatic feature extraction ability, whereas the active learning approach allows to reduce the number of required training samples compared to a fully supervised learning methodology, starting with a reduced database of 40 adsorption energies and requesting more DFT calculations as the learning process progresses until 450 TM@MXene were analyzed. Four criteria were imposed for suitability towards CO sensing: CO adsorption energy between −0.8 and −0.6 eV, negative surface formation energy, charge transfer of at least 0.15 electrons upon CO adsorption, and visible surface density of states change near the Fermi level in the presence of adsorbed CO. In the end, the authors identified $Sc@Zr_3C_2O_2$ and $Y@Zr_3C_2O_2$, the only systems predicted to satisfy all four criteria, as the most promising TM@MXene candidates for CO sensing.

C−N coupling

Electrochemical C−N coupling is a promising way to efficiently convert excess CO_2/N_2 or harmful N-containing NO_3^-/NO_2^- anions into valuable products, such as urea, methylamine, and acetamide, for example. This approach is both environmentally beneficial and sustainable, since it decreases the dependence on fossil fuels, while promoting a more circular economy. It is known that the pivotal step in this process is the initial formation of the C−N bond, which determines the activity and selectivity of the C−N coupling. Therefore, Jiao et al.[231] built activity and selectivity pathways for 54 MXene surfaces by employing DFT calculations. Their findings revealed that the activity of the C−N coupling step primarily hinges on the strength of *CO adsorption ($E_{ad\text{-}CO}$), while selectivity is influenced by the co-adsorption strengths of *N and *CO ($E_{ad\text{-}N}$ and $E_{ad\text{-}CO}$). Consequently, they proposed that an ideal C−N coupling MXene catalyst should display moderate *CO adsorption and stable *N adsorption. Their study further incorporated ML techniques to derive data-driven correlations, describing the relationship between $E_{ad\text{-}CO}$ and $E_{ad\text{-}N}$, using atomic physical chemistry features. By applying these formulas, the researchers efficiently screened 162 MXene materials without the need for more time-intensive

DFT calculations. Several potential catalysts, including $Ta_2W_2C_3$, were identified as promising for C−N coupling performance, and subsequently validated through further DFT calculations.

Solar spectral absorption

Ding et al.[232] investigated the use of MXenes-based metasurface absorbers (MMA) to enhance solar spectral absorption, a crucial aspect of solar cell technology. Despite significant advancements in this field, conventional materials and design methods have not met practical requirements. MXenes, known for their spectral selectivity, are considered as promising solar-absorbing materials, with their optical properties closely linked to their chemistry. The work from these authors focused on examining the absorption characteristics of various MMA configurations with different terminal groups in the solar spectrum. To address this, the authors employed a random forest regression model, built specifically for these systems. The random forest method facilitated the entire process, from parameter selection to structural optimization, with a remarkable low error rate of only 0.02%, surpassing two other classical ML algorithms, linear regression and k-nearest neighbors, which were used for comparison. The simulation results demonstrated that the MMA with $Ti_3C_2O_2$ achieved exceptional solar absorption, absorbing 93.2% of the solar spectrum and emitting a mere 1.2% in the mid-infrared band (5000–13,000 nm), making it an almost ideal solar absorber. Furthermore, the proposed MMA exhibited advantageous properties, such as polarization insensitivity and angular independence, all while maintaining a slender profile. Notably, the maximum absorptivity and corresponding structural parameters were predicted directly by the random forest regression model, eliminating the complexities and time-consuming aspects associated with traditional manual design processes. This approach points in the direction regarding the design of solar absorber structures.

Machine-learning features

The majority of the machine-learning works targeting MXenes reviewed in this work (Table 9) focused on developing workflows to predict numerical properties (regression), with random forest being the most common selected algorithm. The median dataset had 287 examples and the average number of features among the works that included feature selection was 12, which, by our experience, constitutes a reasonable proportion of selected features to total number examples (~4%). In the works that calculated the feature importance for the respective models, cf. Table 10 and Fig. 10, it is possible to observe that most of the important properties were elemental properties, such as electronegativity, ionization energy, atomic mass, atomic radius, boiling point, valence electrons, molar volume, etc. Properties related to the elements present on the external layer (surface terminations) of the MXene material were also key, since many predicted processes and properties are promoted by the interface of these materials. The most important DFT property that appeared as input was the formation energy.

Future perspectives

As the computational power increases, molecular models used in the simulations are becoming more realistic. The inclusion of the MXene surface termination in the computational models was one such improvement, since MXene functionalization, aside from more accurately matching the experimentally observed material, is desired for catalytic applications because bare MXenes do not satisfy the Sabatier principle for most molecules, as they interact too strongly. Another crucial advance of the computational models of MXenes was the consideration of metallic atoms other than the M element of the MXene, both as double transition metal MXenes and as metal atom dopants on the surface to form single-atom catalysts.

The number of MXenes predicted to be stable is expected to increase exponentially each time a new experimental or theoretical discovery increases the tuneability of MXenes. Examples of this are the synthesis of bimetallic MXenes, the observation of previously unknown possible MXene surface terminations and mixtures thereof, or the identification of oxygen within the carbon layers of MXenes, which suggested that most carbide MXenes are in fact oxycarbides.

We expect to see a rise in the number of studies on MXene-deposited single-atom catalysts, since the deposition of single atoms of a metallic element has been shown in many contexts and for many MXenes to lead to an intermediate MXene-adsorbate interaction strength, between the easily poisoned bare MXenes and the almost inactive fully terminated ones. Thus, MXene-based single-atom catalysts seem very promising to make use of the reactivity of the M layer of MXenes towards adsorption and bond activation, while still allowing the surface termination to limit the adsorption strength of reaction intermediates, following the Sabatier principle. Also, the dynamics of mixtures of surface terminations, of ions and solvent molecules within multiple layers of MXenes, and their role in the properties displayed by MXenes, are difficult to prove by experimental approaches only and, consequently, future computational studies are needed, conceivably taking advantage of on-the-fly machine-learned potentials. Another under-explored area is related with defective MXene surfaces (vacancies, areas devoid of terminations).

In order to enhance our understanding of the properties of MXenes and to improve the discovery of new MXenes, it will be essential to integrate high-throughput DFT, data-driven methods, and ML approaches into a cohesive framework. Within this approach, the following strategies can be employed:

1. High-throughput DFT Methods: i) Develop automated pipelines for performing high-throughput DFT calculations, reducing manual intervention and speeding up the process of preparing calculations; ii) continue leveraging high-performance computing clusters to handle large-scale DFT calculations; iii) take advantage of improved DFT methods, with more accuracy to compute specific interactions and properties, while also allowing faster convergence and reduced computational cost, enabling the evaluation of a larger number of MXene possibilities.
2. Data Management: i) Establish a centralized and standardized database to store and manage the vast amount of MXene data that can be simulated using high-throughput DFT; ii) ensure data quality and consistency by implementing rigorous criteria for appropriate MXene DFT calculations; iii) employ data-mining techniques to extract meaningful MXene properties from the increasing number of publications targeting these materials and build a larger database.
3. Machine learning: i) Mutually validate DFT and experimental data using appropriate statistical criteria and/or machine learning methods. ii) use machine learning to identify the most relevant features that influence MXene properties, in order to target these features to be included in databases, thus contributing to improve future models; iii) implement active learning approaches where machine learning models iteratively suggest the most informative MXene systems to simulate or synthesize next, thus saving time and resources.
4. Integrated DFT, data and ML approaches: Create an automated closed-loop system where DFT simulations feed data into machine learning models, and the insights gained inform further simulations and experimental validations.
5. Collaboration and open-source: Foster the collaboration among scientists working with MXenes using different experimental and computational approaches through the use and production of open-source platforms, tools and shared databases.
6. The next MXene frontier: Explore combinations of elements and characteristics of MXene materials that are absent from current databases, and, thus, might not be recommended by expert knowledge or current ML models.

By integrating high-throughput DFT, data-driven methods, and ML approaches, the process of discovering new MXene-based materials can become more efficient and effective, leading to faster advancements in their realistic application.

Table 10 | Number of features considered in studies devoted to the prediction of the properties of MXenes by machine learning and, when available, the ones that were considered more important

Year, authors	Output	Number of Features[a]	Most relevant features
Rajan et al.[54]	Metal−semiconductor identification	47 | 11	Volume per atom; Average elemental boiling point; Standard deviation of group number in the periodic table; Standard deviation of average elemental boiling point; Formation Enthalpy.
Rajan et al.[54]	Band-gap estimation	47 | 15	Molar volume; Mean elemental boiling point; Standard deviation of mean elemental group number in periodic table; Standard deviation of mean elemental melting point; Formation Energy.
Frey et al.[209]	Synthesizability	>80 | >80	M-X bond length; Cohesive energy; Bader charge of X; Formation energy; Mass per atom.
Mishra et al.[212]	Valence band	56 | 7	Average vacuum potential; Conduction band minima; MXene phase; Vacuum potential for the lower surface; Band gap.
Marchwiany et al.[219]	Cytotoxicity	17 | 17	MxOy presence; Li on the surface; Surface modification; Delaminating agent; Lateral size; Cl on the surface.
Venturi et al.[214]	Mechanical strength, band gap and formation energy	NA | NA	Atomic and bond feature vectors were used. Authors did not report the most important features, but selected descriptors as group or period numbers, electronegativity, number of valence electrons or nature of bonded atoms.
Wang et al.[222]	HER	41 | 5	Distance between oxygen and metal atoms in the outermost layer; Distance between the nearest neighbor oxygen atoms; Ionization energy difference; Average value of affinity energy; Number of valence electrons of X.
Zheng et al.[221]	HER	24 | 20	Electronegativity of T; Atomic mass of T; M-X bond length; Bader charge of T; Bader charge of X.
He et al.[210]	Stability	25 | 16	The most important descriptor, $(\chi(M)\text{-}R_{vdW}(M))^3$, where $R_{vdW}(M)$ and $\chi(M)$ correspond to the atomic van der Waals radius and the electronegativity, respectively, of the metal atom (M), was identified via the symbolic regression of the material stability. Other descriptors were: number of electrons in the d orbital of M; electronegativity of M; second ionization energy of M; first ionization energy of M.
Li et al.[226]	Energy storage	19 | 16	Categorical descriptors indicating the presence of Mg, K, Ta, Hf, and O.
Song et al.[218]	Saturation magnetization	9 | 9	Number of unpaired electrons of M; Enthalpy of atomization; Atomic number; Polarizability; Density.
Tian et al.[216]	Tensile stiffness	19 | 3	Thickness; Stiffness of M–X bonds; Surface terminations.
Abraham et al.[229]	CO_2 activation	18 | 18	d-band center; Surface metal electronegativity; Number of valence electrons of M.
Boonpalit et al.[230]	CO sensing	NA | NA	Atomic and bond feature vectors were used.
Chen et al.[224]	ORR and OER	NA | 12	Charge transfer; d-band center of the active transition metal.
Jiao et al.[231]	C−N coupling	13 | 13	Period number; Atomic first ionization-energy; Atomic Pauling electronegativity; Number of valence electrons of M; Atomic weight; Atomic radius of M; Thickness.
Liang et al.[223]	HER	49 | 8	Molar volume of surface element; Atomic radius of single atom; Boiling point of surface element; Boiling point of single atom; Electron affinities of surface element.
Liang et al.[223]	HER	49 | 8	Third ionization potential of surface group element; Ionic radius of surface group element; Atomic mass of surface element; Atomic radius of surface element; Molar volume of surface element
Ma et al.[225]	ORR and OER	13 | 13	Hydroxide adsorption energy; Binding energy of Pt on substrate; d-band center of Pt; Oxide formation enthalpy; Lattice constant.
Roy et al.[213]	Work function	15 | 15	Electronegativity of T atoms; Ionization potential of T atoms; Electron affinity of T atoms; Orbital radius of the outermost orbitals of the T atoms; Orbital radius of the outermost orbitals of the M atoms.

[a]Value on the left denotes the number of features originally considered by the authors before a feature selection step (cf. Table 9, Feature selection column), while the value on the right denotes the number of features used to predict the properties of MXene after selecting the relevant ones.

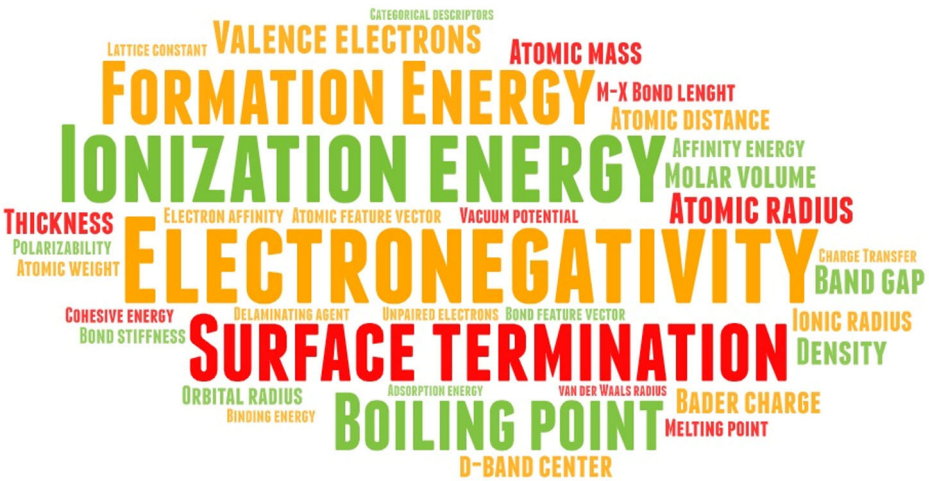

Fig. 10 | Word cloud. Word cloud of the most important feature descriptions in the ML works that had this information available.

Data availability

Data sharing is not applicable to this article as no new data were created or analyzed in this study.

Received: 5 August 2024; Accepted: 15 January 2025;
Published online: 01 February 2025

References

1. Gogotsi, Y. & Anasori, B. The rise of MXenes. *ACS Nano* **13**, 8491–8494 (2019).
2. Naguib, M. et al. Two-dimensional nanocrystals produced by exfoliation of Ti_3AlC_2. *Adv. Mater.* **23**, 4248–4253 (2011).
3. Li, T. et al. Fluorine-free synthesis of high-purity $Ti_3C_2T_x$ (T=OH, O) via alkali treatment. *Angew. Chem. Int. Ed.* **130**, 6223–6227 (2018).
4. Sun, W. et al. Electrochemical etching of Ti_2AlC to Ti_2CT_x (MXene) in low-concentration hydrochloric acid solution. *J. Mater. Chem. A* **5**, 21663–21668 (2017).
5. Yang, S. et al. Fluoride-free synthesis of two-dimensional titanium carbide (MXene) using a binary aqueous system. *Angew. Chem. Int. Ed.* **57**, 15491–15495 (2018).
6. Hart, J. L. et al. Control of MXenes' electronic properties through termination and intercalation. *Nat. Commun.* **10**, 522 (2019).
7. Persson, I. et al. On the organization and thermal behavior of functional groups on Ti_3C_2 MXene surfaces in vacuum. *2D Mater* **5**, 015002 (2017).
8. Kamysbayev, V. et al. Covalent surface modifications and superconductivity of two-dimensional metal carbide MXenes. *Science* **369**, 979–983 (2020).
9. Zhang, B., Zhou, J. & Sun, Z. MBenes: progress, challenges and future. *J. Mater. Chem. A* **10**, 15865–15880 (2022).
10. Solangi, N. H. et al. Recent trends in MXene-based material for biomedical applications. *Environ. Res.* **222**, 115337 (2023).
11. Idumah, C. I. Recent advancements in electromagnetic interference shielding of polymer and mxene nanocomposites. *Polym. Technol. Mater.* **62**, 19–53 (2023).
12. Guo, H. et al. State of the art recent advances and perspectives in 2D MXene-based microwave absorbing materials: a review. *Nano Res.* **16**, 10287–10325 (2023).
13. Sun, J. *et al.* Recent advances in the synthesis of MXene quantum dots. *Chem. Rec*. **23**, e202200268 (2023).
14. George, S. C., Nair, S. T. & Sophia Ponraj, J. *MXene-Filled Polymer Nanocomposites* https://doi.org/10.1201/9781003164975 (CRC Press, 2022).
15. Zhan, C., Sun, W., Xie, Y., Jiang, D. & Kent, P. R. C. Computational discovery and design of mxenes for energy applications: status, successes, and opportunities. *ACS Appl. Mater. Interfaces* **11**, 24885–24905 (2019).
16. Zhu, H. et al. DFT practice in MXene-based materials for electrocatalysis and energy storage: from basics to applications. *Ceram. Int.* **48**, 27217–27239 (2022).
17. Meng, L., Viñes, F. & Illas, F. Theoretical modelling of the Hydrogen evolution reaction on MXenes: a critical review. *Curr. Opin. Electrochem.* **40**, 101332 (2023).
18. Morales-García, Á., Calle-Vallejo, F. & Illas, F. MXenes: new horizons in catalysis. *ACS Catal* **10**, 13487–13503 (2020).
19. Bai, S. et al. Recent advances of MXenes as electrocatalysts for hydrogen evolution reaction. *npj 2D Mater. Appl.* **5**, 78 (2021).
20. Ahmad Junaidi, N. H., Wong, W. Y., Loh, K. S., Rahman, S. & Daud, W. R. W. A comprehensive review of MXenes as catalyst supports for the oxygen reduction reaction in fuel cells. *Int. J. Energy Res.* **45**, 15760–15782 (2021).
21. Wong, W. Y. & Sulaiman, R. R. R. MXene as catalyst. in *Fundamental Aspects and Perspectives of MXenes* (eds. Khalid, M., Grace, A. N., Arulraj, A. & Numan, A.) 241–269 https://doi.org/10.1007/978-3-031-05006-0_10 (Springer Nature Switzerland AG, 2022).
22. Yang, Y., Xu, Y., Li, Q., Zhang, Y. & Zhou, H. Two-dimensional carbide/nitride (MXene) materials in thermal catalysis. *J. Mater. Chem. A* **10**, 19444–19465 (2022).
23. Sun, Y. et al. Applications of MXenes and their composites in catalysis and photoelectrocatalysis. In *Mxenes and their Composites* 449–498 https://doi.org/10.1016/B978-0-12-823361-0.00007-1 (Elsevier, 2022).
24. Xia, C. et al. Recent catalytic applications of MXene-based layered nanomaterials. *Chemosphere* **325**, 138323 (2023).
25. Kohn, W. & Sham, L. J. Self-consistent equations including exchange and correlation effects. *Phys. Rev.* **140**, A1133–A1138 (1965).
26. Perdew, J. P. & Schmidt, K. Jacob's ladder of density functional approximations for the exchange-correlation energy. *AIP Conf. Proc.* **577**, 1–20 (2001).
27. Perdew, J. P., Burke, K. & Ernzerhof, M. Generalized gradient approximation made simple. *Phys. Rev. Lett.* **77**, 3865–3868 (1996).
28. Tao, J., Perdew, J. P., Staroverov, V. N. & Scuseria, G. E. Climbing the density functional ladder: nonempirical meta–generalized gradient approximation designed for molecules and solids. *Phys. Rev. Lett.* **91**, 146401 (2003).
29. Zhao, Y. & Truhlar, D. G. The M06 suite of density functionals for main group thermochemistry, thermochemical kinetics, noncovalent interactions, excited states, and transition elements: two new functionals and systematic testing of four M06-class functionals and 12 other functionals. *Theor. Chem. Acc.* **120**, 215–241 (2008).
30. Kim, K. & Jordan, K. D. Comparison of density functional and MP2 calculations on the water monomer and dimer. *J. Phys. Chem.* **98**, 10089–10094 (1994).
31. Stephens, P. J., Devlin, F. J., Chabalowski, C. F. & Frisch, M. J. Ab initio calculation of vibrational absorption and circular dichroism spectra using density functional force fields. *J. Phys. Chem.* **98**, 11623–11627 (1994).
32. Perdew, J. P., Ernzerhof, M. & Burke, K. Rationale for mixing exact exchange with density functional approximations. *J. Chem. Phys.* **105**, 9982–9985 (1996).
33. Adamo, C. & Barone, V. Toward reliable density functional methods without adjustable parameters: the PBE0 model. *J. Chem. Phys.* **110**, 6158–6170 (1999).
34. Chai, J.-D. & Head-Gordon, M. Systematic optimization of long-range corrected hybrid density functionals. *J. Chem. Phys*. **128**, 084106 (2008).
35. Yanai, T., Tew, D. P. & Handy, N. C. A new hybrid exchange–correlation functional using the Coulomb-attenuating method (CAM-B3LYP). *Chem. Phys. Lett.* **393**, 51–57 (2004).
36. Heyd, J., Scuseria, G. E. & Ernzerhof, M. Hybrid functionals based on a screened Coulomb potential. *J. Chem. Phys.* **118**, 8207–8215 (2003).
37. Iikura, H., Tsuneda, T., Yanai, T. & Hirao, K. A long-range correction scheme for generalized-gradient-approximation exchange functionals. *J. Chem. Phys.* **115**, 3540–3544 (2001).
38. Grimme, S. Semiempirical hybrid density functional with perturbative second-order correlation. *J. Chem. Phys*. **124**, 034108 (2006).
39. Goerigk, L. & Grimme, S. Efficient and accurate double-hybrid-meta-GGA density functionals—evaluation with the extended gmtkn30 database for general main group thermochemistry, kinetics, and noncovalent interactions. *J. Chem. Theory Comput.* **7**, 291–309 (2011).
40. Grimme, S., Antony, J., Ehrlich, S. & Krieg, H. A consistent and accurate ab initio parametrization of density functional dispersion correction (DFT-D) for the 94 elements H-Pu. *J. Chem. Phys.* **132**, 154104 (2010).
41. Grimme, S. Semiempirical GGA-type density functional constructed with a long-range dispersion correction. *J. Comput. Chem.* **27**, 1787–1799 (2006).

42. Ramalho, J. P. P., Gomes, J. R. B. & Illas, F. Accounting for van der Waals interactions between adsorbates and surfaces in density functional theory based calculations: selected examples. *RSC Adv.* **3**, 13085 (2013).
43. Electron correlations in narrow energy bands. *Proc. R. Soc. London. Ser. A. Math. Phys. Sci*. **276**, 238–257 (1963).
44. Perdew, J. P. & Zunger, A. Self-interaction correction to density-functional approximations for many-electron systems. *Phys. Rev. B* **23**, 5048–5079 (1981).
45. Tran, F. & Blaha, P. Accurate band gaps of semiconductors and insulators with a semilocal exchange-correlation potential. *Phys. Rev. Lett.* **102**, 226401 (2009).
46. Chai, J.-D. & Head-Gordon, M. Long-range corrected hybrid density functionals with damped atom–atom dispersion corrections. *Phys. Chem. Chem. Phys.* **10**, 6615 (2008).
47. Mardirossian, N. & Head-Gordon, M. Mapping the genome of meta-generalized gradient approximation density functionals: the search for B97M-V. *J. Chem. Phys*. **142**, (2015).
48. Carvalho, A. P. et al. Sticky-MARTINI as a reactive coarse-grained model for molecular dynamics simulations of silica polymerization. *npj Comput. Mater.* **8**, 49 (2022).
49. Choudhary, K. & Tavazza, F. Convergence and machine learning predictions of Monkhorst-Pack k-points and plane-wave cut-off in high-throughput DFT calculations. *Comput. Mater. Sci.* **161**, 300–308 (2019).
50. Fajín, J. L. C., Cordeiro, M. N. D. S., Gomes, J. R. B. & Illas, F. On the need for spin polarization in heterogeneously catalyzed reactions on nonmagnetic metallic surfaces. *J. Chem. Theory Comput.* **8**, 1737–1743 (2012).
51. Moosavi, S. M., Jablonka, K. M. & Smit, B. The role of machine learning in the understanding and design of materials. *J. Am. Chem. Soc.* **142**, 20273–20287 (2020).
52. Wang, A. Y.-T. et al. Machine learning for materials scientists: an introductory guide toward best practices. *Chem. Mater.* **32**, 4954–4965 (2020).
53. MXene Database | Project aNANt. https://anant.mrc.iisc.ac.in/apps/mxene.
54. Rajan, A. C. et al. Machine-learning-assisted accurate band gap predictions of functionalized MXene. *Chem. Mater.* **30**, 4031–4038 (2018).
55. Massoumılari, Ş., Doğancı, M. & Velioğlu, S. Unveiling the potential of MXenes for H_2 purification and CO_2 capture as an emerging family of nanomaterials. *AIChE J*. **68**, (2022).
56. MXene-db: MXene Database. Contains structural and bandgap data for over 4000 MXene structures. https://github.com/diegonti/MXene-DB.
57. Ontiveros, D., Viñes, F. & Sousa, C. Bandgap engineering of MXene compounds for water splitting. *J. Mater. Chem. A* **11**, 13754–13764 (2023).
58. Bordonhos, M. et al. Multiscale computational approaches toward the understanding of materials. *Adv. Theory Simul.* **6**, 2200628 (2023).
59. Tibshirani, R. Regression shrinkage and selection via the Lasso. *J. R. Stat. Soc. Ser. B* **58**, 267–288 (1996).
60. Galvão, T. L. P., Novell-Leruth, G., Kuznetsova, A., Tedim, J. & Gomes, J. R. B. Elucidating structure–property relationships in aluminum alloy corrosion inhibitors by machine learning. *J. Phys. Chem. C* **124**, 5624–5635 (2020).
61. Chen, T. & Guestrin, C. XGBoost: a scalable tree boosting system. In *Proc. 22nd ACM SIGKDD International Conference on Knowledge Discovery and Data Mining* 785–794 https://doi.org/10.1145/2939672.2939785 (ACM, 2016).
62. Shwartz-Ziv, R. & Armon, A. Tabular data: deep learning is not all you need. *Inf. Fusion* **81**, 84–90 (2022).
63. Shmueli, G. To explain or to predict? *Stat. Sci*. **25**, 289–310 (2010).
64. Herm, L.-V., Heinrich, K., Wanner, J. & Janiesch, C. Stop ordering machine learning algorithms by their explainability! A user-centered investigation of performance and explainability. *Int. J. Inf. Manage.* **69**, 102538 (2023).
65. Molinaro, A. M., Simon, R. & Pfeiffer, R. M. Prediction error estimation: a comparison of resampling methods. *Bioinformatics* **21**, 3301–3307 (2005).
66. López de Prado, M. Feature Importance. in *Advances in Financial Machine Learning* 113–128 (John Wiley & Sons, Inc., 2018).
67. Lundberg, S. M. & Lee, S. -I. A unified approach to interpreting model predictions. In Proceedings of the 31st International Conference on Neural Information Processing Systems (NIPS'17). Curran Associates Inc., Red Hook, NY, USA, 4768–4777 https://proceedings.neurips.cc/paper_files/paper/2017/file/8a20a8621978632d76c43dfd28b67767-Paper.pdf (2017).
68. Willmott, C. J. & Matsuura, K. Advantages of the mean absolute error (MAE) over the root mean square error (RMSE) in assessing average model performance. *Clim. Res.* **30**, 79–82 (2005).
69. Chicco, D. & Jurman, G. The advantages of the Matthews correlation coefficient (MCC) over F1 score and accuracy in binary classification evaluation. *BMC Genom.* **21**, 6 (2020).
70. Khaledialidusti, R., Khazaei, M., Khazaei, S. & Ohno, K. High-throughput computational discovery of ternary-layered MAX phases and prediction of their exfoliation for formation of 2D MXenes. *Nanoscale* **13**, 7294–7307 (2021).
71. Anasori, B. & Gogotsi, Y. *2D Metal Carbides and Nitrides (MXenes): Structure, Properties and Applications*. *2D Metal Carbides and Nitrides (MXenes): Structure, Properties and Applications* https://doi.org/10.1007/978-3-030-19026-2 (Springer International Publishing, 2019).
72. Murali, G. et al. A review on MXene synthesis, stability, and photocatalytic applications. *ACS Nano* **16**, 13370–13429 (2022).
73. Urbankowski, P. et al. Synthesis of two-dimensional titanium nitride Ti_4N_3 (MXene). *Nanoscale* **8**, 11385–11391 (2016).
74. Soundiraraju, B. & George, B. K. Two-dimensional titanium nitride (Ti_2N) MXene: synthesis, characterization, and potential application as surface-enhanced Raman scattering substrate. *ACS Nano* **11**, 8892–8900 (2017).
75. Peng, Q. et al. Unique lead adsorption behavior of activated hydroxyl group in two-dimensional titanium carbide. *J. Am. Chem. Soc.* **136**, 4113–4116 (2014).
76. Xie, Y. et al. Role of surface structure on Li-ion energy storage capacity of two-dimensional transition-metal carbides. *J. Am. Chem. Soc.* **136**, 6385–6394 (2014).
77. Zhang, N., Hong, Y., Yazdanparast, S. & Asle Zaeem, M. Superior structural, elastic and electronic properties of 2D titanium nitride MXenes over carbide MXenes: a comprehensive first principles study. *2D Mater.* **5**, 045004 (2018).
78. Aghaei, S. M., Torres, I., Baboukani, A. R., Khakpour, I. & Wang, C. Impact of surface oxidation on the structural, electronic transport, and optical properties of two-dimensional titanium nitride (Ti_3N_2) MXene. *Comput. Condens. Matter* **20**, e00382 (2019).
79. Björk, J. & Rosen, J. Functionalizing MXenes by tailoring surface terminations in different chemical environments. *Chem. Mater.* **33**, 9108–9118 (2021).
80. Gouveia, J. D. & Gomes, J. R. B. Effect of the surface termination on the adsorption of flue gas by the titanium carbide MXene. *Mater. Today Chem.* **29**, 101441 (2023).
81. Deeva, E. B. et al. In situ XANES/XRD study of the structural stability of two-dimensional molybdenum carbide Mo_2CT_x: implications for the catalytic activity in the water-gas shift reaction. *Chem. Mater.* **31**, 4505–4513 (2019).
82. Gouveia, J. D. & Gomes, J. R. B. The determining role of T_x species in the catalytic potential of MXenes: water adsorption and dissociation on Mo_2CT_x. *Catal. Today* **424**, 113848 (2023).

83. Hou, P. et al. Unraveling the oxidation behaviors of mxenes in aqueous systems by active-learning-potential molecular-dynamics simulation. *Angew. Chem. Int. Edit.* **135**, e202304205 (2023).
84. Dahlqvist, M. & Rosen, J. Chalcogen and halogen surface termination coverage in MXenes—structure, stability, and properties. *npj 2D Mater. Appl.* **8**, 65 (2024).
85. Sun, W. et al. A new 2D monolayer BiXene, M_2C (M = Mo, Tc, Os). *Nanoscale* **8**, 15753–15762 (2016).
86. Gouveia, J. D., Viñes, F., Illas, F. & Gomes, J. R. B. MXenes atomic layer stacking phase transitions and their chemical activity consequences. *Phys. Rev. Mater.* **4**, 054003 (2020).
87. Henkelman, G. & Jónsson, H. A dimer method for finding saddle points on high dimensional potential surfaces using only first derivatives. *J. Chem. Phys* **111**, 7010–7022 (1999).
88. Jurado, A., Morales-García, Á., Viñes, F. & Illas, F. Identifying the atomic layer stacking of Mo_2C MXene by probe molecule adsorption. *J. Phys. Chem. C* **125**, 26808–26813 (2021).
89. Downes, M. et al. M_5X_4: a family of MXenes. *ACS Nano* **17**, 17158–17168 (2023).
90. Nemani, S. K. et al. High-entropy 2D carbide MXenes: $TiVNbMoC_3$ and $TiVCrMoC_3$. *ACS Nano* **15**, 12815–12825 (2021).
91. Leong, Z. et al. Elucidating the chemical order and disorder in high-entropy MXenes: a high-throughput survey of the atomic configurations in $TiVNbMoC_3$ and $TiVCrMoC_3$. *Chem. Mater.* **34**, 9062–9071 (2022).
92. Ma, W. et al. A novel high-entropy MXene $Ti_{1.1}V_{1.2}Cr_{0.8}Nb_{1.0}Mo_{0.9}C_4T_x$ for high-performance supercapacitor. *Scr. Mater.* **235**, 115596 (2023).
93. Hantanasirisakul, K. et al. Evidence of a magnetic transition in atomically thin $Cr_2TiC_2T_x$ MXene. *Nanoscale Horiz.* **5**, 1557–1565 (2020).
94. Scheibe, B. et al. Study on the magnetic properties of differently functionalized multilayered $Ti_3C_2T_x$ MXenes and Ti-Al-C carbides. *Appl. Surf. Sci.* **479**, 216–224 (2019).
95. Yoon, Y. et al. Low temperature solution synthesis of reduced two dimensional Ti_3C_2 MXenes with paramagnetic behaviour. *Nanoscale* **10**, 22429–22438 (2018).
96. García-Romeral, N. et al. Theoretical analysis of magnetic coupling in the Ti_2C bare MXene. *J. Phys. Chem. C* **127**, 3706–3714 (2023).
97. Lv, P., Li, Y.-L. & Wang, J.-F. Monolayer Ti_2C MXene: manipulating magnetic properties and electronic structures by an electric field. *Phys. Chem. Chem. Phys.* **22**, 11266–11272 (2020).
98. Gouveia, J. D., Morales-García, Á., Viñes, F., Gomes, J. R. B. & Illas, F. MXenes à la Carte: tailoring the epitaxial growth alternating nitrogen and transition metal layers. *ACS Nano* **16**, 12541–12552 (2022).
99. Si, C., Zhou, J. & Sun, Z. Half-metallic ferromagnetism and surface functionalization-induced metal–insulator transition in graphene-like two-dimensional Cr_2C crystals. *ACS Appl. Mater. Interfaces* **7**, 17510–17515 (2015).
100. Khazaei, M. et al. Novel electronic and magnetic properties of two-dimensional transition metal carbides and nitrides. *Adv. Funct. Mater.* **23**, 2185–2192 (2013).
101. He, J., Lyu, P. & Nachtigall, P. New two-dimensional Mn-based MXenes with room-temperature ferromagnetism and half-metallicity. *J. Mater. Chem. C* **4**, 11143–11149 (2016).
102. García-Romeral, N., Morales-García, Á., Viñes, F., de P. R. Moreira, I. & Illas, F. How does thickness affect magnetic coupling in Ti-based MXenes. *Phys. Chem. Chem. Phys.* **25**, 17116–17127 (2023).
103. García-Romeral, N., Morales-García, Á., Viñes, F., de P. R. Moreira, I. & Illas, F. The nature of the electronic ground state of M_2C (M = Ti, V, Cr, Zr, Nb, Mo, Hf, Ta, and W) MXenes. *Phys. Chem. Chem. Phys.* **25**, 31153–31164 (2023).
104. Karlsson, L. H., Birch, J., Halim, J., Barsoum, M. W. & Persson, P. O. Å. Atomically resolved structural and chemical investigation of single MXene sheets. *Nano Lett* **15**, 4955–4960 (2015).
105. Sang, X. et al. Atomic defects in monolayer titanium carbide ($Ti_3C_2T_x$) MXene. *ACS Nano* **10**, 9193–9200 (2016).
106. Bandyopadhyay, A., Ghosh, D. & Pati, S. K. Effects of point defects on the magnetoelectronic structures of MXenes from first principles. *Phys. Chem. Chem. Phys.* **20**, 4012–4019 (2018).
107. Xiao-Hong, L., Xiang-Ying, S. & Rui-Zhou, Z. Effect of vacancies on the structural and electronic properties of Ti_2CO_2. *RSC Adv* **9**, 27646–27651 (2019).
108. Gouveia, J. D. & Gomes, J. R. B. Structural and energetic properties of vacancy defects in MXene surfaces. *Phys. Rev. Mater.* **6**, 024004 (2022).
109. Parey, V., Abraham, B. M., Mir, S. H. & Singh, J. K. High-throughput screening of atomic defects in MXenes for CO_2 capture, activation, and dissociation. *ACS Appl. Mater. Interfaces* **13**, 35585–35594 (2021).
110. Li, X.-H. et al. Influence of C-vacancy-line defect on electronic and optical properties and quantum capacitance of Ti_2CO_2 MXene: a first-principles study. *J. Phys. Chem. Solids* **176**, 111254 (2023).
111. Gouveia, J. D. & Coutinho, J. Can we rely on hybrid-DFT energies of solid-state problems with local-DFT geometries? *Electron. Struct.* **1**, 015008 (2019).
112. Tao, Q. et al. Two-dimensional $Mo_{1.33}C$ MXene with divacancy ordering prepared from parent 3D laminate with in-plane chemical ordering. *Nat. Commun.* **8**, 14949 (2017).
113. Afonso, R. V., Gouveia, J. D. & Gomes, J. R. B. Catalytic reactions for H_2 production on multimetallic surfaces: a review. *J. Phys. Energy* **3**, 032016 (2021).
114. Single-atom catalysts push the boundaries of heterogeneous catalysis. *Nat. Commun*. **12**, 5884 (2021).
115. Zhang, X. et al. A Ti-anchored Ti_2CO_2 monolayer (MXene) as a single-atom catalyst for CO oxidation. *J. Mater. Chem. A* **4**, 4871–4876 (2016).
116. Zhang, J. et al. Single platinum atoms immobilized on an MXene as an efficient catalyst for the hydrogen evolution reaction. *Nat. Catal.* **1**, 985–992 (2018).
117. Zhao, D. et al. MXene (Ti_3C_2) vacancy-confined single-atom catalyst for efficient functionalization of CO_2. *J. Am. Chem. Soc.* **141**, 4086–4093 (2019).
118. Oschinski, H., Morales-García, Á. & Illas, F. Interaction of first row transition metals with M_2C (M = Ti, Zr, Hf, V, Nb, Ta, Cr, Mo, and W) MXenes: a quest for single-atom catalysts. *J. Phys. Chem. C* **125**, 2477–2484 (2021).
119. Keyhanian, M., Farmanzadeh, D., Morales-García, Á. & Illas, F. Effect of oxygen termination on the interaction of first row transition metals with M_2C MXenes and the feasibility of single-atom catalysts. *J. Mater. Chem. A* **10**, 8846–8855 (2022).
120. Kraushofer, F. & Parkinson, G. S. Single-atom catalysis: insights from model systems. *Chem. Rev.* **122**, 14911–14939 (2022).
121. Rocha, H., Gouveia, J. D. & Gomes, J. R. B. Transition metal atom adsorption on the titanium carbide MXene: trends across the periodic table for the bare and O-terminated surfaces. *Phys. Rev. Mater.* **6**, 105801 (2022).
122. Yang, W. et al. Design and fabrication of an ultra-sensitive Ta_2C MXene/Au-coated tilted grating sensor. *Sens. Actuators B Chem.* **369**, 132391 (2022).
123. Akinola, O., Chakraborty, I., Celio, H., Akinwande, D. & Incorvia, J. A. C. Synthesis and characterization of Cr_2C MXenes. *J. Mater. Res.* **36**, 1980–1989 (2021).
124. Venkateshalu, S. et al. New method for the synthesis of 2D vanadium nitride (MXene) and its application as a supercapacitor electrode. *ACS Omega* **5**, 17983–17992 (2020).
125. Maldonado-Lopez, D. et al. Atomic-scale understanding of Li storage processes in the Ti_4C_3 and chemically ordered $Ti_2Ta_2C_3$ MXenes: a theoretical and experimental assessment. *ACS Appl. Energy Mater.* **5**, 1801–1809 (2022).

126. Gouveia, J. D., Morales-García, Á., Viñes, F., Gomes, J. R. B. & Illas, F. Facile heterogeneously catalyzed nitrogen fixation by MXenes. *ACS Catal* **10**, 5049–5056 (2020).
127. Zhou, J. et al. A two-dimensional zirconium carbide by selective etching of Al_3C_3 from nanolaminated $Zr_3Al_3C_5$. *Angew. Chem. Int. Ed.* **55**, 5008–5013 (2016).
128. Liu, M.-Z. et al. The influence of different functional groups on quantum capacitance, electronic and optical properties of Hf_2C MXene. *Appl. Surf. Sci.* **605**, 154830 (2022).
129. Jasani, J., Mishra, P. & Sonvane, Y. A First-principles investigation of the structural and electronic properties of Two-dimensional Hf_2CSe_2. *Mater. Today Proc*. https://doi.org/10.1016/j.matpr.2022.12.266 (2023).
130. Caffrey, N. M. Effect of mixed surface terminations on the structural and electrochemical properties of two-dimensional $Ti_3C_2T_2$ and V_2CT_2 MXenes multilayers. *Nanoscale* **10**, 13520–13530 (2018).
131. Liu, M.-Z., Li, X.-H., Yan, H.-T., Zhang, R.-Z. & Cui, H.-L. Influence of N-doped concentration on the electronic properties and quantum capacitance of Hf_2CO_2 MXene. *Vacuum* **210**, 111826 (2023).
132. Michałowski, P. P. et al. Oxycarbide MXenes and MAX phases identification using monoatomic layer-by-layer analysis with ultralow-energy secondary-ion mass spectrometry. *Nat. Nanotechnol.* **17**, 1192–1197 (2022).
133. Gouveia, J. D. & Gomes, J. R. B. Structural and electronic properties of the titanium carbide MXene with variable sublattice oxygen composition. *Surf. Interfaces* **46**, 103920 (2024).
134. Michałowski, P. P. Unraveling the composition of each atomic layer in the MXene/MAX phase structure—identification of oxycarbide, oxynitride, and oxycarbonitride subfamilies of MXenes. *Nanoscale Horizons* **9**, 1493–1497 (2024).
135. Gouveia, J. D. & Gomes, J. R. B. Effect of surface composition on the stability of Ti- and V-based oxycarbide and oxynitride MXenes. *Mater. Today Phys.* **46**, 101481 (2024).
136. He, Z. et al. Two-dimensional TiVC solid-solution MXene as surface-enhanced Raman scattering substrate. *ACS Nano* **16**, 4072–4083 (2022).
137. Zhang, Y. et al. Vibrational properties of TiVC-based Mxenes by first-principles calculation and experiments. *Mater. Today Commun.* **34**, 105396 (2023).
138. Dion, M., Rydberg, H., Schröder, E., Langreth, D. C. & Lundqvist, B. I. Van der Waals density functional for general geometries. *Phys. Rev. Lett.* **92**, 246401 (2004).
139. Hamada, I. van der Waals density functional made accurate. *Phys. Rev. B* **89**, 121103 (2014).
140. Niu, K., Chi, L., Rosen, J. & Björk, J. C–H activation of light alkanes on MXenes predicted by hydrogen affinity. *Phys. Chem. Chem. Phys.* **22**, 18622–18630 (2020).
141. Junkaew, A. & Arróyave, R. Enhancement of the selectivity of MXenes (M_2C, M = Ti, V, Nb, Mo) via oxygen-functionalization: promising materials for gas-sensing and -separation. *Phys. Chem. Chem. Phys.* **20**, 6073–6082 (2018).
142. Gouveia, J. D. et al. First-principles calculations on the adsorption behavior of amino acids on a titanium carbide MXene. *ACS Appl. Bio Mater.* **3**, 5913–5921 (2020).
143. Morales-Salvador, R. et al. Carbon capture and usage by MXenes. *ACS Catal.* **11**, 11248–11255 (2021).
144. Persson, I. et al. 2D transition metal carbides (MXenes) for carbon capture. *Adv. Mater.* **31**, 1805472 (2019).
145. Obodo, K. O., Ouma, C. N. M., Modisha, P. M. & Bessarabov, D. Density functional theory calculation of Ti_3C_2 MXene monolayer as catalytic support for platinum towards the dehydrogenation of methylcyclohexane. *Appl. Surf. Sci.* **529**, 147186 (2020).
146. Li, Z. et al. Two-dimensional transition metal carbides as supports for tuning the chemistry of catalytic nanoparticles. *Nat. Commun.* **9**, 5258 (2018).
147. SPENCER, N. Iron single crystals as ammonia synthesis catalysts: Effect of surface structure on catalyst activity. *J. Catal.* **74**, 129–135 (1982).
148. Honkala, K. et al. Ammonia synthesis from first-principles calculations. *Science* **307**, 555–558 (2005).
149. Evans, M. G. & Polanyi, M. Inertia and driving force of chemical reactions. *Trans. Faraday Soc.* **34**, 11 (1938).
150. Bronsted, J. N. Acid and basic catalysis. *Chem. Rev.* **5**, 231–338 (1928).
151. Gomes, J. R. B., Bofill, J. M. & Illas, F. Azomethane decomposition catalyzed by Pt(111): an example of anti-Brönsted−Evans−Polanyi behavior. *J. Phys. Chem. C* **112**, 1072–1080 (2008).
152. Mars, P. & van Krevelen, D. W. Oxidations carried out by means of vanadium oxide catalysts. *Chem. Eng. Sci.* **3**, 41–59 (1954).
153. Daisley, A. & Hargreaves, J. S. J. Metal nitrides, the Mars-van Krevelen mechanism and heterogeneously catalysed ammonia synthesis. *Catal. Today* **423**, 113874 (2023).
154. Shao, M. et al. Efficient nitrogen fixation to ammonia on MXenes. *Phys. Chem. Chem. Phys.* **20**, 14504–14512 (2018).
155. Fajín, J. L. C., Cordeiro, M. N. D. S., Illas, F. & Gomes, J. R. B. Influence of step sites in the molecular mechanism of the water gas shift reaction catalyzed by copper. *J. Catal.* **268**, 131–141 (2009).
156. Gokhale, A. A., Dumesic, J. A. & Mavrikakis, M. On the mechanism of low-temperature water gas shift reaction on copper. *J. Am. Chem. Soc.* **130**, 1402–1414 (2008).
157. Ghuman, K. K., Yadav, S. & Singh, C. V. Adsorption and dissociation of H_2O on monolayered MoS_2 edges: energetics and mechanism from ab initio simulations. *J. Phys. Chem. C* **119**, 6518–6529 (2015).
158. Tran, N. Q., Bui, V. Q., Le, H. M., Kawazoe, Y. & Lee, H. Anion-cation double substitution in transition metal dichalcogenide to accelerate water dissociation kinetic for electrocatalysis. *Adv. Energy Mater.* **8**, 1702139 (2018).
159. Gouveia, J. D., Morales-García, Á., Viñes, F., Illas, F. & Gomes, J. R. B. MXenes as promising catalysts for water dissociation. *Appl. Catal. B Environ.* **260**, 118191 (2020).
160. Fajín, J. L. C., Cordeiro, M. N. D. S., Illas, F. & Gomes, J. R. B. Descriptors controlling the catalytic activity of metallic surfaces toward water splitting. *J. Catal.* **276**, 92–100 (2010).
161. Fajín, J. L. C., Cordeiro, M. N. D. S. & Gomes, J. R. B. Water dissociation on bimetallic surfaces: general trends. *J. Phys. Chem. C* **116**, 10120–10128 (2012).
162. Fajín, J. L. C., Cordeiro, M. N. D. S. & Gomes, J. R. B. Water dissociation on multimetallic catalysts. *Appl. Catal. B Environ.* **218**, 199–207 (2017).
163. Zhu, C., Liang, J.-X., Wang, Y.-G. & Li, J. Non-noble metal single-atom catalyst with MXene support: Fe_1/Ti_2CO_2 for CO oxidation. *Chin. J. Catal.* **43**, 1830–1841 (2022).
164. Yu, X. et al. Monolayer Ti_2CO_2: a promising candidate for NH_3 sensor or capturer with high sensitivity and selectivity. *ACS Appl. Mater. Interfaces* **7**, 13707–13713 (2015).
165. Gouveia, J. D., Novell-Leruth, G., Viñes, F., Illas, F. & Gomes, J. R. B. The Ti_2CO_2 MXene as a nucleobase 2D sensor: a first-principles study. *Appl. Surf. Sci.* **544**, 148946 (2021).
166. Peng, Q., Zhang, X., Geng, Z., Yang, Z. & Yang, J. Single Zn atom catalyst on Ti_2CN_2 MXenes for efficient CO oxidation. *Phys. E Low-Dimens. Syst. Nanostruct.* **147**, 115595 (2023).
167. Kountoupi, E. et al. The impact of oxygen surface coverage and carbidic carbon on the activity and selectivity of two-dimensional molybdenum carbide (2D-Mo_2C) in Fischer–Tropsch synthesis. *ACS Catal.* **14**, 1834–1845 (2024).
168. van Santen, R. A., Markvoort, A. J., Filot, I. A. W., Ghouri, M. M. & Hensen, E. J. M. Mechanism and microkinetics of the Fischer–Tropsch reaction. *Phys. Chem. Chem. Phys.* **15**, 17038–17063 (2013).

169. Speight, J. G. Production of hydrocarbons from natural gas. in *Handbook of Industrial Hydrocarbon Processes* (ed. Speight, J. G.) 127–162 https://doi.org/10.1016/C2009-0-18464-7 (Elsevier, 2011).
170. Fajín, J., Cordeiro, M. & Gomes, J. Fischer-Tropsch synthesis on multicomponent catalysts: what can we learn from computer simulations? *Catalysts* **5**, 3–17 (2015).
171. Champagne, A. & Charlier, J.-C. Physical properties of 2D MXenes: from a theoretical perspective. *J. Phys. Mater.* **3**, 032006 (2021).
172. Zha, X.-H. et al. Role of the surface effect on the structural, electronic and mechanical properties of the carbide MXenes.*Europhys. Lett.* **111**, 26007 (2015).
173. Zhang, Y., Sa, B., Miao, N., Zhou, J. & Sun, Z. Computational mining of Janus Sc_2C-based MXenes for spintronic, photocatalytic, and solar cell applications. *J. Mater. Chem. A* **9**, 10882–10892 (2021).
174. Banoth, P., Kandula, C. & Kollu, P. *Introduction to Electrocatalysts. Noble Metal-Free Electrocatalysts: New Trends in Electrocatalysts for Energy Applications*. Vol. 2, 1–37, https://doi.org/10.1021/bk-2022-1432.ch001 (2022).
175. Nørskov, J. K. et al. Origin of the overpotential for oxygen reduction at a fuel-cell cathode. *J. Phys. Chem. B* **108**, 17886–17892 (2004).
176. Exner, K. S. Elementary reaction steps in electrocatalysis: theory meets experiment. in *Encyclopedia of Solid-Liquid Interfaces* 65–92 https://doi.org/10.1016/B978-0-323-85669-0.00025-8 (Elsevier, 2024).
177. Razzaq, S. & Exner, K. S. Materials screening by the descriptor $G_{max}(\eta)$: the free-energy span model in electrocatalysis. *ACS Catal.* **13**, 1740–1758 (2023).
178. Exner, K. S. A universal descriptor for the screening of electrode materials for multiple-electron processes: beyond the thermodynamic overpotential. *ACS Catal.* **10**, 12607–12617 (2020).
179. Kozuch, S. & Shaik, S. How to conceptualize catalytic cycles? The energetic span model. *Acc. Chem. Res.* **44**, 101–110 (2011).
180. Meng, L., Yan, L.-K., Viñes, F. & Illas, F. Effect of terminations on the hydrogen evolution reaction mechanism on Ti_3C_2 MXene. *J. Mater. Chem. A* **11**, 6886–6900 (2023).
181. López, M., Exner, K. S., Viñes, F. & Illas, F. Theoretical study of the mechanism of the hydrogen evolution reaction on the V_2C MXene: thermodynamic and kinetic aspects. *J. Catal.* **421**, 252–263 (2023).
182. Handoko, A. D. et al. Tuning the basal plane functionalization of two-dimensional metal carbides (MXenes) to control hydrogen evolution activity. *ACS Appl. Energy Mater.* **1**, 173–180 (2018).
183. Hinnemann, B. et al. Biomimetic hydrogen evolution: MoS_2 nanoparticles as catalyst for hydrogen evolution. *J. Am. Chem. Soc.* **127**, 5308–5309 (2005).
184. Jin, D. et al. Computational screening of 2D ordered double transition-metal carbides (MXenes) as electrocatalysts for hydrogen evolution reaction. *J. Phys. Chem. C* **124**, 10584–10592 (2020).
185. López, M., Exner, K. S., Viñes, F. & Illas, F. Computational Roubaix diagrams for MXenes: a key ingredient toward proper theoretical electrocatalytic studies. *Adv. Theory Simul.* **6**, 2200217 (2023).
186. Lim, K. R. G. et al. 2H-MoS_2 on Mo_2CT_x MXene nanohybrid for efficient and durable electrocatalytic hydrogen evolution. *ACS Nano* **14**, 16140–16155 (2020).
187. Azofra, L. M., Li, N., MacFarlane, D. R. & Sun, C. Promising prospects for 2D d2 –d4 M_3C_2 transition metal carbides (MXenes) in N_2 capture and conversion into ammonia. *Energy Environ. Sci.* **9**, 2545–2549 (2016).
188. Gao, Y. et al. Mo_2TiC_2 MXene: a promising catalyst for electrocatalytic ammonia synthesis. *Catal. Today* **339**, 120–126 (2020).
189. Li, Q., He, L., Sun, C. & Zhang, X. Computational study of MoN_2 monolayer as electrochemical catalysts for nitrogen reduction. *J. Phys. Chem. C* **121**, 27563–27568 (2017).
190. Johnson, L. R. et al. MXene materials for the electrochemical nitrogen reduction—functionalized or not? *ACS Catal.* **10**, 253–264 (2020).
191. Anasori, B. et al. Two-dimensional, ordered, double transition metals carbides (MXenes). *ACS Nano* **9**, 9507–9516 (2015).
192. Caffrey, N. M. Prediction of optimal synthesis conditions for the formation of ordered double-transition-metal MXenes (o-MXenes). *J. Phys. Chem. C* **124**, 18797–18804 (2020).
193. Zhao, R. et al. Two-dimensional ordered double-transition metal carbides for the electrochemical nitrogen reduction reaction. *ACS Appl. Mater. Interfaces* **15**, 6797–6806 (2023).
194. Zhao, Z. et al. Atomic catalyst supported on oxygen defective MXenes for synergetic electrocatalytic nitrate reduction to ammonia: a first principles study. *Appl. Surf. Sci.* **614**, 156077 (2023).
195. Gao, X. & Tse, E. C. M. Unraveling the performance descriptors for designing single-atom catalysts on defective MXenes for exclusive nitrate-to-ammonia electrocatalytic upcycling. *Small* **20**, 2306311 (2024).
196. Gao, G., O'Mullane, A. P. & Du, A. 2D MXenes: a new family of promising catalysts for the hydrogen evolution reaction. *ACS Catal.* **7**, 494–500 (2017).
197. Kan, D. et al. Rational design of bifunctional ORR/OER catalysts based on Pt/Pd-doped Nb_2CT_2 MXene by first-principles calculations. *J. Mater. Chem. A* **8**, 3097–3108 (2020).
198. Kuznetsov, D. A. et al. Single site cobalt substitution in 2D molybdenum carbide (MXene) enhances catalytic activity in the hydrogen evolution reaction. *J. Am. Chem. Soc.* **141**, 17809–17816 (2019).
199. Kuznetsov, D. A. et al. Single-atom-substituted Mo_2CT_x:Fe-layered carbide for selective oxygen reduction to hydrogen peroxide: tracking the evolution of the MXene phase. *J. Am. Chem. Soc.* **143**, 5771–5778 (2021).
200. Chen, X., Zhang, Y., Lin, S., Zhang, H. & Zhao, X. Screening of single transition metal substitution in two-dimensional Mo_2CT_x MXene electrocatalyst with ultrahigh activity for oxygen reduction reaction. *Surf. Interfaces* **36**, 102585 (2023).
201. Wang, Y., Tian, W., Zhang, H. & Wang, Y. Nb_2N monolayer as a promising anode material for Li/Na/K/Ca-ion batteries: a DFT calculation. *Phys. Chem. Chem. Phys.* **23**, 12288–12295 (2021).
202. Lu, S., Zhang, Y., Lou, F. & Yu, Z. Theoretical study of single transition metal atom catalysts supported on two-dimensional Nb2NO2 for efficient electrochemical CO2 reduction to CH4. *J. CO2 Util.* **62**, 102069 (2022).
203. Nørskov, J. K. et al. Trends in the exchange current for hydrogen evolution. *J. Electrochem. Soc.* **152**, J23 (2005).
204. Zheng, S., Zuo, C., Liang, X., Li, S. & Pan, F. Valence state of transition metal center as an activity descriptor for CO_2 reduction on single atom catalysts. *J. Energy Chem.* **56**, 444–448 (2021).
205. Li, F., Ai, H., Shi, C., Lo, K. H. & Pan, H. Single transition metal atom catalysts on Ti_2CN_2 for efficient CO_2 reduction reaction. *Int. J. Hydrogen Energy* **46**, 12886–12896 (2021).
206. Meng, L., Yan, L.-K., Viñes, F. & Illas, F. Surface termination dependent carbon dioxide reduction reaction on Ti_3C_2 MXene. *J. Mater. Chem. A* **12**, 7856–7874 (2024).
207. Zhou, S. et al. Vacancy-rich MXene-immobilized ni single atoms as a high-performance electrocatalyst for the hydrazine oxidation reaction. *Adv. Mater.* **34**, 2204388 (2022).
208. Qian, C., Sun, K. & Bao, W. Recent advance on machine learning of <scp>MXenes</scp> for energy storage and conversion. *Int. J. Energy Res.* **46**, 21511–21522 (2022).
209. Frey, N. C. et al. Prediction of synthesis of 2D metal carbides and nitrides (MXenes) and their precursors with positive and unlabeled machine learning. *ACS Nano* **13**, 3031–3041 (2019).

210. He, M. & Zhang, L. Machine learning and symbolic regression investigation on stability of MXene materials. *Comput. Mater. Sci.* **196**, 110578 (2021).
211. Saal, J. E., Kirklin, S., Aykol, M., Meredig, B. & Wolverton, C. Materials design and discovery with high-throughput density functional theory: the Open Quantum Materials Database (OQMD). *JOM* **65**, 1501–1509 (2013).
212. Mishra, A. et al. Accelerated data-driven accurate positioning of the band edges of MXenes. *J. Phys. Chem. Lett.* **10**, 780–785 (2019).
213. Roy, P., Rekhi, L., Koh, S. W., Li, H. & Choksi, T. S. Predicting the work function of 2D MXenes using machine-learning methods. *J. Phys. Energy* **5**, 034005 (2023).
214. Venturi, V., Parks, H. L., Ahmad, Z. & Viswanathan, V. Machine learning enabled discovery of application-dependent design principles for two-dimensional materials. *Mach. Learn. Sci. Technol.* **1**, 035015 (2020).
215. Lipatov, A. et al. Elastic properties of 2D Ti 3 C 2 T x MXene monolayers and bilayers. *Sci. Adv.* **4**, eaat0491 (2018).
216. Tian, S. et al. Investigation and understanding of the mechanical properties of MXene by high-throughput computations and interpretable machine learning. *Extrem. Mech. Lett.* **57**, 101921 (2022).
217. Gong, C. et al. Discovery of intrinsic ferromagnetism in two-dimensional van der Waals crystals. *Nature* **546**, 265–269 (2017).
218. Song, Y.-Y., Wu, X.-C., Li, S.-Z., Sun, Q. & Zhang, W.-B. A simple descriptor for magnetic classification of 2D MXene materials. *AIP Adv*. **12**, 075106 (2022).
219. Marchwiany, M. E., Birowska, M., Popielski, M., Majewski, J. A. & Jastrzębska, A. M. Surface-related features responsible for cytotoxic behavior of MXenes layered materials predicted with machine learning approach. *Materials* **13**, 3083 (2020).
220. Geim, A. K. & Grigorieva, I. V. Van der Waals heterostructures. *Nature* **499**, 419–425 (2013).
221. Zheng, J. et al. High-throughput screening of hydrogen evolution reaction catalysts in MXene materials. *J. Phys. Chem. C* **124**, 13695–13705 (2020).
222. Wang, X. et al. Accelerating 2D MXene catalyst discovery for the hydrogen evolution reaction by computer-driven workflow and an ensemble learning strategy. *J. Mater. Chem. A* **8**, 23488–23497 (2020).
223. Liang, H., Liu, P., Xu, M., Li, H. & Asselin, E. A study of two-dimensional single atom-supported MXenes as hydrogen evolution reaction catalysts using density functional theory and machine learning. *Int. J. Quantum Chem.* **123**, e27055 (2023).
224. Chen, Y. et al. M-N 4 -Gr/MXene heterojunction nanosheets as oxygen reduction and evolution reaction catalysts: machine learning and density functional theory insights. *ACS Appl. Nano Mater.* **6**, 7694–7703 (2023).
225. Ma, N. et al. Machine learning-assisted exploration of the intrinsic factors affecting the catalytic activity of ORR/OER bifunctional catalysts. *Appl. Surf. Sci.* **628**, 157225 (2023).
226. Li, S. & Barnard, A. S. Inverse design of MXenes for high-capacity energy storage materials using multi-target machine learning. *Chem. Mater.* **34**, 4964–4974 (2022).
227. Cheng, J., Li, T., Wang, Y., Ati, A. H. & Sun, Q. The relationship between activated H2 bond length and adsorption distance on MXenes identified with graph neural network and resonating valence bond theory. *J. Chem. Phys*. **159**, 191101 (2023).
228. Liu, S. et al. Hydrogen storage in incompletely etched multilayer Ti_2CT_x at room temperature. *Nat. Nanotechnol.* **16**, 331–336 (2021).
229. Abraham, B. M. et al. Machine learning-driven discovery of key descriptors for CO_2 activation over two-dimensional transition metal carbides and nitrides. *ACS Appl. Mater. Interfaces* **15**, 30117–30126 (2023).
230. Boonpalit, K., Kinchagawat, J., Prommin, C., Nutanong, S. & Namuangruk, S. Efficient exploration of transition-metal decorated MXene for carbon monoxide sensing using integrated active learning and density functional theory. *Phys. Chem. Chem. Phys.* **25**, 28657–28668 (2023).
231. Jiao, Y., Li, H., Jiao, Y. & Qiao, S.-Z. Activity and selectivity roadmap for C–N electro-coupling on MXenes. *J. Am. Chem. Soc.* **145**, 15572–15580 (2023).
232. Ding, Z. et al. Machine learning in prediction of MXenes-based metasurface absorber for maximizing solar spectral absorption. *Sol. Energy Mater. Sol. Cells* **262**, 112563 (2023).

Acknowledgements

This work was developed within the scope of the projects CICECO-Aveiro Institute of Materials, UIDB/50011/2020 (DOI 10.54499/UIDB/50011/2020), UIDP/50011/2020 (DOI 10.54499/UIDP/50011/2020) and LA/P/0006/2020 (DOI 10.54499/LA/P/0006/2020), and ForTheShift, with ref. 2022.02949.PTDC (DOI 10.54499/2022.02949.PTDC), financed by national funds through the FCT/MEC (PIDDAC). TLPG and JDG thank the Portuguese Foundation for Science and Technology (FCT) for the grants with Refs. 2022.08205.CEECIND and 2023.06511.CEECIND, respectively, in the scope of the Individual Call to Scientific Employment Stimulus—5th and 6th Editions.

Author contributions

J.D.G., T.L.P.G., K.I.N., and J.R.B.G. contributed to literature research and data collection. J.D.G., T.L.P.G., and J.R.B.G conceptualized the review and were responsible for funding. J.R.B.G. supervised the project. All authors approved the final manuscript.

Competing interests

The authors declare no competing interests.

Additional information

Correspondence and requests for materials should be addressed to José R. B. Gomes.